Co-evaporated Hybrid Metal-Halide Perovskite Thin-Films for Optoelectronic Applications



Juliane Borchert

Wadham College

University of Oxford

A thesis submitted for the degree of

Doctor of Philosophy

Trinity 2019

Acknowledgements

I would like to thank Prof Michael Johnston for his guidance, encouragement and enthusiasm for my scientific projects and my development as a scientist. I would also like to thank Prof Henry Snaith for his support and for being a never ending supply of new ideas for experiments. Furthermore, I would like to thank Prof Laura Herz who, while not officially my supervisor always generously offered ideas, feedback and perspective on my work.

Many thanks go to all of the members of the three research groups I have been connected to, the Photovoltaic and Optoelectronic Device Group, the Terahertz Photonics Group and the Semiconductors Group. I am grateful for fruitful scientific collaborations and conversations, many hours of inspiring chats over tea and home-baked cakes, pub visits, punt tours and conference adventures. I would like to especially thank the group members who I had the pleasure of collaborating with on studies included in this thesis, in particular Dr Jay Patel, Dr Rebecca Milot, Dr Mathias Uller Rothmann, Dr Christopher Davies, Dr Adam Wright, Dr Laura Martínez Maestro, Dr Maximilian Hoerantner and Dr Lavina Snoek.

I had the great opportunity to collaborate with a number of experts around the world who have deeply enriched my research. In particular Dr Renée Haver of the Chemistry Department of the University of Oxford, Dr Ievgen Levchuk and Prof Christoph Brabec of the Friedrich-Alexander-Universität Erlangen-Nürnberg, Dr Li (Lily) Li of the Australian National University and Dr Sudha Mokkapati of Monash University.

Furthermore, I want to thank Dr David Sharp and Dr Jason Brown for their expertly introduction to atomic force microscopy, scanning electron microscopy and photolithography, as well as Charlotte Abraham whose close reading of this thesis immensely improved it.

The EPSRC Center for Doctoral Training in New and Sustainable Photovoltaics not only provided me with funding but also training, which allowed me insights into the wider field of solar cells and other renewable energy technologies. I am also immensely grateful for the cohort of fellow students and network of researchers that I gained through it.

Wadham College and its MCR and Chapel community managed to not only always keep me fed, but also, supported, entertained and connected to the wider world. I am grateful for the friends from many disciplines I have found there and the inspirations I was able to drawn from this very diverse community.

Finally I want to thank my friends and family, especially my sisters who have supplied me with endless encouragement in the form of postcards, visits, scoldings, surprise presents, chocolate, and phone calls.

Abstract

Since the fabrication of the first organic-inorganic halide perovskites solar cell in 2009 this material class has shown a lot of promise for solar cell and other semiconductor device applications. The rapid increase in the realised power conversion efficiencies and the unusual properties of the perovskite materials have drawn many researchers to focus on this material group. The perovskite materials which are investigated for use in solar cells, combine many advantageous properties which are known from either organic or inorganic semiconductors. Their high carrier mobilities, long carrier diffusion lengths, and long radiative lifetimes are similar to those in inorganic semiconductors, while the processibility at low temperatures and from solution as well as the chemical tunability of the optical properties are comparable to properties found in organic semiconductors.

Co-evaporation is a versatile method to deposit organic-inorganic halide perovskite thin-films. It was pioneered in 2013 and offers several advantages over solution-based deposition techniques. Co-evaporated films are exceptionally smooth and uniform and due to the additive nature of the technique can be deposited onto solvent sensitive substrates which is crucial for the fabrication of flexible substrates or when building a multi-layer stack for tandem solar cells.

In this thesis the co-evaporation of organic-inorganic halide perovskite thin-films is developed further and the resulting films and devices are studied in detail. Initially, the first reported co-evaporation of formamidinium lead triiodide ($FAPbI_3$) solar cells is realised and high efficiencies are achieved. Subsequently, the impact of impurities on the co-vaporation of methylammonium lead triiodide ($MAPbI_3$) is studied and insights are gained to improve the process control and reproducibility of the co-evaporation of perovskite thin-films. Finally, the experience and knowledge gained from these two studies are combined to fabricated co-evaporated patterned ($FAPbI_3$) thin-films for applications in semi-transparent solar cells and micro-lasers.

The results from this thesis are important contributions towards the deeper understanding of organic-inorganic halide perovskites and their properties as well as towards the development of stable, efficient, large-scale perovskites solar cells.

Contents

List of Publications xi

1 Introduction 1

2 Metal-halide Perovskite Devices 5

2.1 Solar cells . . . 5

2.1.1 Physics of solar cells . . . 5

2.1.1.1 The solar spectrum . . . 5

2.1.1.2 Solar cell efficiency limitations . . . 6

2.2 Metal-halide perovskite solar cells . . . 8

2.2.1 Development of metal-halide perovskite semiconductors . . . 8

2.2.2 Development of metal-halide perovskite solar cells . . . 9

2.2.2.1 Device architectures . . . 11

2.2.2.2 Transporting layers . . . 11

2.2.2.3 Properties of metal-halide perovskite semiconductors . . . 13

3 Co-evaporation as a Deposition Method for Perovskite Solar Cells 17

3.1 Physical vapour deposition of thin-films . . . 17

3.2 Physical vapour deposition of metal Halide perovskite thin-films . . . 19

3.3 Co-evaporation of methylammonium lead iodide . . . 21

3.4 Moving beyond $MAPbI_3$ - new materials . . . 22

3.5 Co-evaporation enabling insights into fundamental material properties . . . 25

4 Methods 27

4.1 Fabrication techniques . . . 27

4.1.1 Co-evaporation of perovskite thin films . . . 27

4.1.2 Deposition of contact layers . . . 28

4.2 Solar cell characterisation . . . 31

4.2.1 J-V curves . . . 31

4.2.2 External quantum efficiency (EQE) . . . 34

5 Vapour Deposited Formamidinium Lead Triiodide **37**
5.1 Introduction and background . . . 37
5.2 Sample preparation . . . 38
5.2.1 Preparation of the $FAPbI_3$ layer . . . 38
5.2.2 Preparation of the full solar cell . . . 39
5.3 Solar cell performance . . . 39
5.3.1 Current-Voltage sweeps (J–V) . . . 40
5.3.2 Stabilised power output (SPO) . . . 40
5.3.3 Spread of solar cell efficiencies . . . 41
5.3.4 External quantum efficiency (EQE) . . . 42
5.4 Film quality . . . 43
5.4.1 Uniformity of deposition . . . 44
5.4.1.1 Uniformity on the microscale . . . 44
5.4.1.2 Uniformity on the macroscale . . . 47
5.4.2 Chemical composition of the thin film . . . 49
5.4.3 Crystallinity of the thin film . . . 50
5.5 Optoelectronic properties . . . 52
5.6 Summary and conclusion . . . 55

6 Influence of Impurities on the Co-evaporation of $MAPbI_3$ **57**
6.1 Introduction and motivation . . . 57
6.2 Methods . . . 60
6.2.1 Solar cell fabrication . . . 60
6.2.2 Stabilised power output measurement . . . 62
6.2.3 In-situ mass spectroscopy . . . 63
6.2.4 Synthesis of methylammonium iodide and the impurities . . . 65
6.2.4.1 Methylammonium synthesis . . . 65
6.2.4.2 Synthesis of neat impurities . . . 66
6.2.5 Nuclear magnetic resonance . . . 67
6.3 Results and discussion . . . 67
6.3.1 Characterisation of precursors . . . 68
6.3.1.1 Nuclear magnetic resonance measurements of different batches of MAI . . . 68
6.3.1.2 Mass spectroscopy Measurements of MAI and its impurities 72
6.3.1.3 Infra-red spectra of precursors and impurities . . . 74
6.3.2 Evaporation of MAI of different purities . . . 75
6.3.3 Rate-controlled evaporation run with high-purity MAI . . . 76
6.3.4 Co-evaporation of $MAPbI_3$ thin-films . . . 77
6.3.5 Deposits on the quartz micro balances . . . 82
6.4 Conclusion and outlook . . . 86

7 Patterned Perovskite Thin-films for Transparent Solar Cells and Lasing 89
7.1 Introduction and motivation 89
7.2 Methods 92
7.2.1 Photolithographic patterning 92
7.2.2 Ion-milling of perovskite thin-films 93
7.2.3 Photoluminescence microscopy 94
7.3 Results and discussion 96
7.3.1 Photolithographically patterned films 96
7.3.2 Ion-milled patterns 103
7.4 Conclusion and outlook 112

8 Conclusion and Outlook 115

References 119

x

List of Publications

Borchert, J., Milot, R. L.; Patel, J. B.; Davies, C. L.; Wright, A. D.; Martínez Maestro, L.; Snaith, H. J.; Herz, L. M.; Johnston, M. B. 'Large-Area, Highly Uniform Evaporated Formamidinium Lead Triiodide Thin Films for Solar Cells'. *ACS Energy Letters*, 2017 2(12), 2799–2804.

Borchert, J.; Levchuk, I.; Snoek, L. C.; Rothmann, M. U.; Haver, R.; Snaith, H. J.;Brabec, C. J.; Herz, L. M.; Johnston, M. B. 'Impurity Tracking Enables Enhanced Control and Reproducibility of Hybrid Perovskite Vapor Deposition'. *ACS Appl. Mater. Interfaces* 2019, 11, 32, 28851-28857

Davies, C. L., **Borchert, J.**, Xia, C. Q., Milot, R. L., Kraus, H., Johnston, M. B., Herz, L. M. 'Impact of the Organic Cation on the Optoelectronic Properties of Formamidinium Lead Triiodide'. *J. Phys. Chem. Lett*, 2018, 9, 28.

1 Introduction

Humanity is facing many global challenges, two crucial ones are climate change and the growing demand for energy, especially in previously under-served regions of the world. One technology that helps address both of these challenges are solar cells for electricity generation [1]. They are ideal for many applications, from small modules to charge phones, to medium-sized installations that power fridges to cool vaccines, to large arrays used to power entire cities, all while emitting no carbon dioxide, which makes solar cells a key technology to fight the climate crisis. Photovoltaic solar cells also offer additional benefits. They can be installed in a distributed fashion which enables electricity generation independently of grid connections or fossil fuel supplies. This has in particular been used to supply remote communities which are not connected to an electricity grid [2]. Furthermore, it enables independence from foreign fossil fuel supplies which may be subject to geopolitical instabilities. Due to these advantages, solar cells have been deployed to generate electricity around the globe and even beyond, for example on the international space station [3] and several Mars rovers [4, 5].

Solar cells can be fabricated from a wide range of semiconductor materials. Hybrid organic-inorganic metal-halide perovskite semiconductors are a new class of solar cell

materials. This emerging material class is advantageous for application in solar cells due to strong absorption in the visible part of the light spectrum [6], favourable electronic properties [7], and a large variety of possible materials and compositions which can be used to optimise the material for a wide range of different applications within the area of photovoltaics and beyond [8].

Aside from their high potential for applications from solar cells [9–12] to light emitting devices [13–15] and transistors [16, 17], hybrid organic-inorganic metal-halide perovskites are also fascinating from a scientific viewpoint. Unusually, these materials consist of both inorganic atoms and small organic molecules which crystallise together in the perovskite structure. This unique group of materials pose many questions, for example about the formation energies and dynamics governing the formation of such hybrid materials, the influence of the different components on the material's properties, and the tunability of the properties by changing the composition.

In this thesis, the emphasis is placed on the co-evaporation of hybrid organic-inorganic metal-halide perovskites for optoelectronic applications, in particular solar cells and lasers. Co-evaporation is a particularly promising deposition method as it offers many advantages over solution-processing techniques. It is solvent free, additive and produces very uniform, pinhole free thin-films. The example of organic light emitting devices (OLED) has shown that thermal evaporation is an excellent technique for the scaling of new semiconductors to commercial scales [18]. While much of the initial research in the field of OLEDs had been done in solution, the evaporation technique proved more robust and scalable and is now the dominant technique for the commercial fabrication of OLED displays [19].

For this thesis, the fabrication, properties and application of co-evaporated hybrid organic-inorganic metal-halide perovskite films were studied. First, in Chapter 5 the deposition of formamidinium lead triiodide ($FAPbI_3$) is presented. For the first time, it was shown

that it is possible to deposit this material with co-evaporation and very smooth films and solar cells with high efficiencies were achieved. This result is an important step towards the co-evaporation of more complex, mixed perovskites and has additionally enabled further research into the properties of $FAPbI_3$ including spectroscopic and transmission electron microscopy studies. Subsequently in Chapter 5.6, the process control during the co-evaporation of methyl-ammonium lead iodide ($MAPbI_3$) and the influence of impurities on the deposition are studied in detail. This study illuminated why many researchers had reported problems with the process control during thermal evaporation and resolved this long-standing issue in the field. Furthermore, an understanding of the mechanism through which impurities influence the co-evaporation was gained. These new insights are crucial for the optimisation and scaling to industrial scales of the co-evaporation of hybrid metal-halide perovskites. A better understanding of the processes during evaporation also offers important guidance that will help speed up the optimisation of co-evaporation for new, more complex perovskites. Finally, the experience and insights gained in the previous chapters are applied to a new area in Chapter 6.4, in which the fabrication and characterisation of patterned co-evaporated $FAPbI_3$ are reported. The versatility of the metal-halide perovskite semiconductor and the additive nature of the co-evaporation process are utilised to fabricate micrometre-sized patterns which are suitable for applications in micro-lasing and semi-transparent solar cells. Both photolithography and ion-milling are employed to achieve the desired patterns. These methods offer a high degree of control over the shape of the fabricated features which is crucial especially for applications in micro-disk lasing. The optical properties of these patterned films are studied and it is shown that they still exhibit photoluminescence even after the photolithographic processing and ion-milling. This confirms their high promise for the use in lasing applications.

The work presented in this thesis contributes to the understanding and control of

co-evaporation processes for the fabrication of hybrid organic-inorganic metal-halide perovskites. $FAPbI_3$ was co-evaporated for the first time, the influence of impurities was studied and the technique was applied towards the field of micro-disk lasers in which it had not been previously employed.

2

Metal-halide Perovskite Devices

2.1 Solar cells

2.1.1 Physics of solar cells

2.1.1.1 The solar spectrum

Solar cells are built to convert light into electrical energy. To optimise their performance, it is important to take into account the spectrum of light they actually receive. Most solar cells are deployed on Earth and outside of buildings. In these conditions, the relevant spectrum is the solar spectrum filtered by the atmosphere of the earth. The spectrum of the light emitted by the sun should resemble that of a black body at 5778 K. As the sunlight passes through the atmosphere of the Earth, some wavelengths are absorbed and scattered by atmospheric molecules. In Figure 2.1, the black body spectrum is compared with the solar spectrum outside of the Earth's atmosphere and the filtered solar spectrum at sea level. In the infrared part of the spectrum, water (H_2O) and carbon dioxide (CO_2) have the largest influence while in the ultraviolet part of the spectrum, ozone (O_3) is responsible for most of the absorption [20].

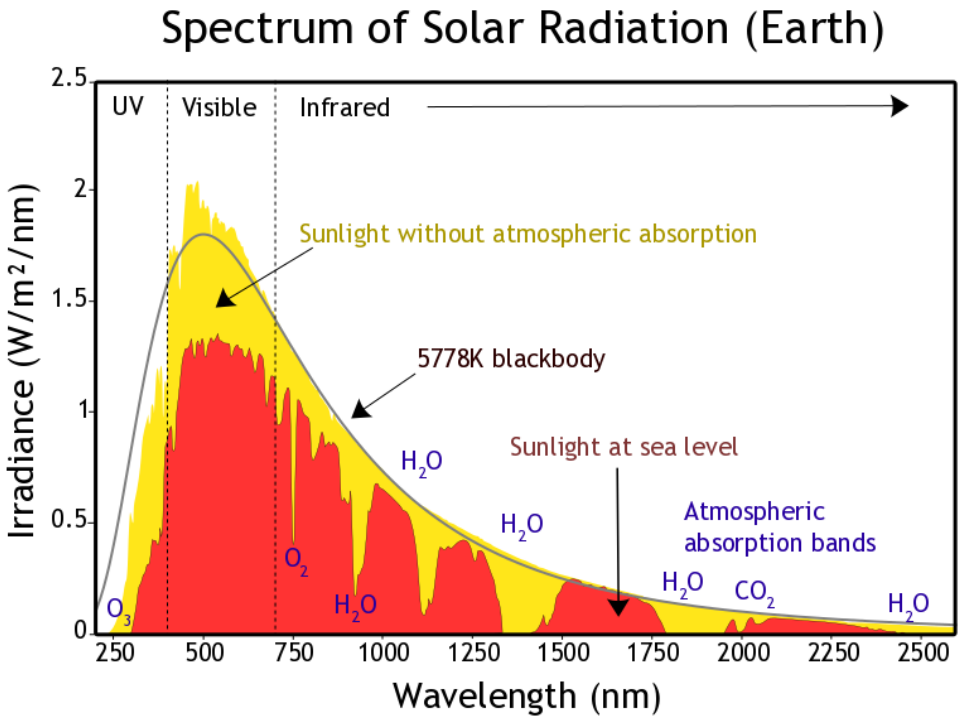


Figure 2.1: Comparison of an ideal black body spectrum, the solar spectrum outside of the Earth's atmosphere and the solar spectrum at sea level. Used with permission under CC BY-SA 3.0 licence [21].

Given the strong influence of the Earth's atmosphere on the spectrum of sun-light, it is important to take the location in which it is meant to be used into account when optimising a solar cell. A solar cell deployed to power a satellite orbiting the Earth receives the unfiltered solar spectrum and should be optimised for it, while solar cells deployed on the surface of the Earth operate under the filtered sunlight and need to be optimised for that spectrum. Taking the spectrum into account is even more relevant when considering solar cells for indoor applications which operate under artificial lights whose spectra can be very different from that of the Sun.

2.1.1.2 Solar cell efficiency limitations

To gain a first idea of how efficient an ideal solar cell could be, one can consider thermodynamics and treat a solar cell as an ideal black body absorber connected to an ideal Carnot heat engine. In this model, the solar radiation is concentrated onto

an ideal black body absorber which runs a Carnot heat engine in contact with the temperature of the Earth. To determine what the efficiency of such a Carnot Engine would be, three temperatures have to be taken into consideration: the temperature of the Sun (T_S), the temperature of the absorber during operation (T_A), and the temperature of the Earth (T_0). The overall efficiency η_{bC} of a black body absorber combined with a Carnot engine is given in Equation 2.1 [22].

$$\eta_{bC} = \left(1 - \frac{T_A^4}{T_S^4}\right)\left(1 - \frac{T_0}{T_A}\right) \tag{2.1}$$

Assuming the temperature of the Sun T_S is 5800 K and the temperature of Earth is 300 K, the overall efficiency reaches a maximum value of 85 % for $T_A = 2478$ K [22].

A more realistic way to consider the maximum efficiency a solar cell can reach is to take into account that solar cells are not black body absorbers but actually semiconductors with a bandgap. Then the question arises which bandgap would give the highest efficiency. A very low band gap would enable the absorption of a large part of the solar spectrum and therefore of many photons, but their energy can only be extracted up to the energy of the bandgap, thus for photons with an energy larger than the bandgap much of their energy would be lost. In the reverse case, if a very large bandgap were chosen, the full energy of such high energy photons could be extracted, but all photons with energies smaller than the bandgap would not be absorbed at all. Therefore, the ideal bandgap must be at an intermediate energy [20]. Shockley and Queiser investigated this for an ideal case in which radiative recombination is the only recombination mechanism and the solar spectrum is approximated as the spectrum of a black body at 6000 K. Their calculation yield a maximum efficiency of 30 % for a single junction solar cell with a bandgap of 1.1 eV [23]. This limit has become known as the Shockley-Queiser limit. To overcome this limit, several concepts have been proposed, either introducing

more than one bandgap, for example in a tandem or intermediate bandgap solar cell, or altering the spectrum using up- or down-conversion to convert more photons into the energy range the solar cell can absorb. Efficient tandem solar cells and even cells with up to six junctions have been reported, while the other proposals to exceed the Shockley-Queisser limit have remained largely theoretical [24].

2.2 Metal-halide perovskite solar cells

2.2.1 Development of metal-halide perovskite semiconductors

Hybrid organic-inorganic metal-halide perovskites are a group of materials which are promising as semiconductors in a variety of applications from solar cells to light emitting devices (LEDs) to transistors and micro lasers. They are only a small subgroup of the much larger perovskite material class. Perovskites are characterised by the fact that they possess the same crystal structure as calcium titanate ($CaTiO_3$). More generally, this means that all perovskites have an (ABX_3) composition. In the case of metal-halide perovskites, A is usually an organic molecule, B a metal, and X a halide. The very first perovskite material was discovered and described by Gustav Rose in 1840 [25]. He described the mineral $CaTiO_3$ which crystallises in the perovskite structure. Through the years, many other materials which crystallise in this structure were found in nature and synthesised in laboratories. Today, we know hundreds of materials in the perovskite structure. Their properties and applications vary widely with insulating, conducting, semiconducting and superconducting perovskites as well as antiferromagnetic, piezoelectric, and thermoelectric perovskite materials [26].

The first hybrid organic-inorganic metal-halide perovskites were synthesised in the early 1990s. Mitzi et al. studied different properties of $CH_3NH_3PbI_3$ including its magnetic, optical and transport properties [27]. Furthermore, both transistors and light emitting devices (LED) were fabricated from this material [28, 29]. But the photovoltaic properties

of these new semiconductors were not studied at the time, partly due to concerns over lead toxicity and a belief that the less harmful tin based alternatives were not robust enough [30]. It took until 2006 for metal-halide perovskites to be utilised in solar cells.

2.2.2 Development of metal-halide perovskite solar cells

Miyasaka and co-workers used $CH_3NH_3PbBr_3$ as a sensitiser in a dye sensitised solar cell and achieved a power conversion efficiency (PCE) of 2.2 % [9]. In 2009, they were able to increase the efficiency to 3.8 % by using iodide instead of bromide [31]. These early perovskite solar cells utilised liquid electrolytes which dissolved the perovskite and led to a rapid degradation of the solar cells. This problem was overcome, when Lee et al. used the solid hole transport material spiro-OMeTAD (2,2',7,7'-Tetrakis-(N,N-di-4-methoxyphenylamino)-9,9'-spirobifluorene) which led to more stable cells and boosted the efficiency to 10.9 % [32]. Improvements to the film-deposition and optimisation of the used contact materials led to rapid improvement in the solar cell efficiency. This attracted additional interest to the field and now thousands of researchers are working on the improvement and understanding of metal-halide perovskite solar cells. This has led to a number of different research trajectories. Some important themes are the development of perovskite with mixed compositions [33], lead free perovskites [34–36], tandem solar cells [37–40], two dimensional perovskites [41–44] and applications beyond solar cells [45, 46].

In an effort to achieve solar cells with higher efficiencies and better stability and to tailor the perovskite's properties for different applications, a wide range of metal-halide perovskites with mixed compositions have been studied. Early examples include the use of mixed halides for example in $CH_3NH_3Pb(I_{1-x}Br_x)_3$ with the aim of tuning the bandgap to make it suitable for tandem solar cells [47]. Using multiple materials

for the same site in the ABX_3 structure has been pushed to an extreme with the development of materials such as the triple A - cation double - halide perovskite $Cs_x(CH(NH_2)_2)_{0.17}(CH_3NH_{0.83})_{1-x}Pb(Br,I)_3$ [33]. Such mixed materials have enabled high solar cell efficiencies of over 20 % and exhibit a longer operational stability than neat $MAPbI_3$ [33]. Mixed perovskites are essential for the fabrication of tandem solar cells as they allow for a tuning of the bandgap.

Two kinds of approaches to making tandem cells are being explored using perovskites. One approach aims to add perovskite as a second layer to an existing solar cell technology to form a tandem solar cell and increase the over all efficiency. This was successfully demonstrated for a number of different bottom cells, for example CIGS [39, 48] and silicon [40, 49–52]. The current efficiency record for a CIGS / perovskite tandem solar cell is 23.26 % [39] while silicon / perovskite tandems have even reached efficiencies of 28 % [40]. In the other approach, perovskite layers are used for both cells of the tandem. This is only possible as mixed perovskite materials can be used to obtain the necessary bandgap. Using a four-terminal architecture efficiencies up to 23 % have been reached [53] and 21 % with the more practical two-terminal approach [54].

Another important theme in recent research into perovskites for solar cells has been focused on finding lead-free materials to reduce the potential environmental impact of large scale fabrication and deployment of perovskite solar cells. One promising avenue is the replacement of lead with tin, yet so far, efficiencies are lagging behind those of lead containing perovskites and tin-based materials struggle with stability issues [55]. Aside from tin, the replacement of lead with a mixed system is also being explored. A typical example for this approach is the double perovskite $Cs_2BiAgBr_6$ [56]. Research into these lead-free double perovskites is in its infancy and so far only relatively low solar cell efficiencies have been reported.

Over the last few years, a wide range of perovskite materials have been synthesised

for application in photovoltaic solar cells. Many of these semiconducting materials are also promising candidates for other optoelectronic and electronic applications from light emitting devices (LEDs) and lasers to transistors, photodetectors and thermoelectric devices [57].

2.2.2.1 Device architectures

A variety of device architectures has been used for perovskite solar cells. Three main types can be distinguished: the dye-sensitised solar cell (DSSC), meso-superstructured solar cell (MSSC) and the planar p-i-n type solar cell. The first solar cells using perovskites were dye-sensitised solar cells, consisting of a nano-crystalline, porous, conductive TiO_2 layer coated by a thin perovskite layer which acts as a dye [31]. The TiO_2 acts as an electron-transport material, while the holes are transported by a liquid electrolyte or solid hole-transport material (HTM).

Another layout was developed from these first DSSCs: the meso-superstructured solar cell. Instead of the TiO_2 layer, it uses a non-conductive porous Al_2O_3 scaffold. This showed that the electron-transport could actually take place in the perovskite layer itself [32]. As a result of this discovery, a new, planar type of perovskite solar cells emerged in which the porous layer is left out altogether and instead planar layers of perovskite are sandwiched between a hole-transport and electron-transport layer [32].

2.2.2.2 Transporting layers

Currently, high-efficiency perovskite solar cells utilise both hole-transport and electron-transport layers. These play an important role in the solar cell, as they enable charge separation and transport. They have to fulfil a number of demands: (1) a fitting band alignment that allows for the flow of one species of carriers and blocks the other; (2) a carrier mobility which at least matches that of the perovskite; (3) formation of a homogeneous and close contact with the absorber layer; (4) no chemical reactions with

the perovskite; (5) one of the transport layers needs to be transparent to let in light [57]. Electron-transport materials, which have typically been used are either organic fullerene derivatives e.g. $6,6-\text{phenyl}\,C_{61}\,\text{butric acid methyl ester}$ (PCBM) or metal oxides such as TiO_2, ZnO, Al_2O_3 and ZrO_2. Many of these materials have already been used for a considerable amount of time not only for organic solar cells, but also for most inorganic commercial thin-film solar cells. Metal sulphides such as CdS, ZnS, Bi_2S_3, MoS_2 and Sb_2S_3 are also considered as electron-transport layers because they possess electron mobilities that are two to three orders of magnitude higher than those of the currently used oxides [57]. Additionally, it has been demonstrated that the use of Sb_2S_3 can improve the stability of the solar cell in comparison to cells using TiO_2 [58]. The drawback of these sulphides is their low transparency. Very thin layers have to be used to allow enough light to pass into the solar cell [57].

On the other side of the absorber, organic semiconductors are used as hole-transport layers. Commonly used polymers are $\text{spiro}-\text{OMeTAD}$ [32], $\text{poly}(3-\text{hexylthiophene})$ (P3HT) [59], $\text{poly}(3,4-\text{ethylenedioxythiophene})-\text{polystyrenesulfonic acid}$ (PEDOT:PSS) [60] and various other polymers. Unfortunately, these polymers have much lower hole mobilities than the perovskite. Only PEDOT:PSS has a higher mobility but is unable to block electrons, is acidic and hygroscopic. Therefore, it is not ideal for use with a perovskite absorber as it would contribute to the fast degradation of the cell [57]. There is a range of inorganic materials that are considered for the hole-transport layer. So far, NiO [61], CuSCN [62] and MoO_x [63] have been used in perovskite cells and others such as MoS_2, MoS_xSe_{1-x}, V_2O_3 and WO_3 could be suitable as they have been used with organic absorber materials before [57]. It is also possible to fabricate a working perosvkite solar cell in which the perovskite itself acts as a hole-transport material and no additional hole-transport layer is added. For this approach, efficiencies of up to 12.8 % have been reported [64].

2.2.2.3 Properties of metal-halide perovskite semiconductors

The advantageous optoelectronic properties of metal-halide perovskites, such as the tunability of key properties and the flexibility in their fabrication, underpin the immense interest in them as semiconductor materials for solar cells, light emitting devices and other applications. In particular, high absorption coefficients [57], high charge-carrier mobilities [65] and long charge-carrier lifetimes [66–68] make perovskites attractive materials for solar cells.

The chemical tunability of their bandgap is another attractive property of metal-halide perovskites. By changing the composition of a metal-halide perovskite, it is possible to tune the bandgap to fit the needs of a given application. For example, high bandgaps can be achieved to exactly fit with another solar cell material to fabricate tandem solar cells. Changing the metal or the halide has the biggest influence on the bandgap. The inorganic components form octahedra which the valance and conduction band depend on most strongly. While the organic component only influences the bandgap slightly, it can significantly change its temperature behaviour [69, 70]. In $MAPbI_3$ the bandgap changes appruptly upon cooling as the MA dipole rotation is abruptly frozen out, whereas in $FAPbI_3$ a graduale change occurs [70].

When the composition is varied to tune the bandgap, non-linear behaviour such as the so-called bandgap bowing need to be taken into account. When iodide and bromine are mixed in $CH_3NH_3Pb(I_{1-x}Br_x)_3$, the bandgap can be tuned linearly between 1.51 eV and 2.21 eV by changing the x value [47]. In contrast, when tin and lead are mixed in $CH_3NH_3Pb_{1-y}Sn_yI_3$ the bandgap does not change linearly when the composition is changed. Instead, mixed phases with y values between 0.25 and 0.5 have lower bandgaps then either of the two unmixed perovskites $CH_3NH_3PbI_3$ and $CH_3NH_3SnI_3$ [71]. This bandgap bowing makes the prediction of the bandgap of a mixed phase more challenging. It has been demonstrated that metal-halide perovskite thin-films can be deposited with

a remarkably wide range of deposition techniques, including solution-based and vapour based techniques. One of the most popular methods for the fabrication of research perovskite solar cells it the one-step spincoating of films from solution. For such a one-step deposition, both precursors, (eg. CH_3NH_3 and PbI_2) are put into the same solution and spin-coated onto a substrate [72]. The composition of the solution, the solvent used, and the spin-coating parameters are varied to optimise the film. A common problem which occurs with spin-coated films are discontinuous films and the formation of pin holes [57]. To optimise this one-step approach for different perovskite compositions, various adaptations such as different solvent systems [73, 74], a quenching of the crystallisation process with anti-solvents [75] or a sudden gas flow [76] and drying and annealing steps have been used.

Another approach is using two-step processes. In a solution-based two-step process, the PbI_2 is first deposited onto the substrate and then dipped into a solution containing CH_3NH_3I or CH_3NH_3Cl, which leads to a rapid transformation into a perovskite film. Using this method, continuous films and efficiencies above 15 % have been reached [77]. It is also possible to use a vapour assisted solution process. A PbI_2 layer is deposited either from solution or from the vapour phase and is subsequently heated and exposed to CH_3NH_3I vapour for an extended period of time. During this annealing, the precursors react and form a perovskite film [78].

A very different group of approaches are vacuum deposition methods. A number of different vacuum-based techniques are used, including co-evaporation, various two-step methods and flash evaporation. Vacuum-based methods offer good control over the composition and thickness of the film. Furthermore, the substrate can be kept at a low temperature which enables the use of flexible substrates [79]. Additionally, vacuum-based methods are additive, allowing for the fabrication of multi-layered devices [80].

The most commonly used evaporation-based deposition method for perovskite thin-films

is co-evaporation [81]. For this method, a vacuum chamber is used in which the substrate is placed above thermal evaporation sources. These are used to heat the precursor material. This is the main method used throughout this thesis and is discussed in detail in Chapter 3. Moreover, perovskite layers have been grown using a number of sequential deposition methods in vacuum. Chen et al. [82] performed a sequential deposition, fully under vacuum using $PbCl_2$ and $rmCH_3NH_3I$. The substrate with the sublimed $PbCl_2$ had to be heated during the evaporation of the MAI to achieve a full conversion to the perovskite. This led to homogeneous perovskite layers and ultimately solar cells with an efficiency of around 15 % [82].

It is also possible to grow a perovskite layer in vacuum by depositing alternating thin layers of the precursors [83]. The deposition and conversion of such multilayers appears to offer a good reproducibility and good homogeneity of the layers, while also being compatible with large-scale production processes. A further method to deposit perovskites under vacuum is flash evaporation, also called single-source thermal ablation. The perovskite is initially synthesised in solution. The perovskite powder is then placed on a metal sheet through which a large current is passed, causing the perovskite to rapidly evaporate and condense on the substrate. Already in 1999, Mitzi et al. reported the deposition of a wide range of layered organic-inorganic perovskites, using this technique [84]. More recently, it has been demonstrated that efficient planar solar cells can be fabricated using perovskite layers grown by flash evaporation [85].

In summary, solar cells need to meet a number of demands. They need to have high efficiencies, be durable and easy to manufacture. Furthermore, they need to be optimised for different environments and applications. Metal-halide perovskite solar cells are a promising new type of solar cell. Since the 1 st perovskite solar cell was reported in 2006 [9] this material group has seen a lot of research activity and a rapid

development. Power conversion efficiencies have quickly risen and many studies to understand the material in depth are being conducted.

3

Co-evaporation as a Deposition Method for Perovskite Solar Cells

3.1 Physical vapour deposition of thin-films

Physical vapour deposition (PVD) is a vacuum based technique for the deposition of thin-films. It is particularly suitable for the deposition of very thin, uniform films onto a wide variety of substrates, including flexible substrates. It is used for a wide range of materials and applications. For example, it is used to deposit thin-films of metals or silicon oxide onto foils to improve their barrier properties for packaging food such as potato crisps [86]. Physical vapour deposition is not limited to inorganic materials, but can also be used to deposit organic materials which is applied to deposit organic semiconductors for organic light emitting devices (OLED). Not only was the first OLED fabricated using vapour deposition in 1987 [87], but also today the majority of commercially produced OLEDs manufacturers employ vapour deposition at a large scale to produce OLEDs for display which are used in mobile telephones, displays and many other applications [19]. Thin films of organic materials for large display applications have very similar requirements as solar cells. Therefore, it is plausible that the successful use of PVD to deposit organic LEDs on a large scale for displays could be translated to the use of PVD

for the deposition of perovskite solar cells on a large scale.

Film formation during vapour deposition takes place in a series of steps. The evaporated atom or molecule impinges on the surface and usually possesses a higher temperature than the surface. It therefore needs to quickly equilibrate with the temperature of the surface to be able to stick to the substrate. Once this thermal accommodation has taken place successfully, the particle can bind to the surface either via physisorption or chemisorption. It can now diffuse on the surface to combine with other atoms to nucleate crystall growth. These initial growth nuclei grow into islands which continue to grow until they start to touch each other and coalesce together. As the film continues to grow, a network of islands forms with channels of uncovered substrate inbetween. As these channels close, secondary nucleation can occur in the remaining holes. Finally, these secondary islands are incorporated into the film and a continuous film forms. During coalescence, the crystallographic orientation of the islands can change leading to recrystallisation. This can result in larger domain sizes than would be expected from the distance between the initial randomly oriented nuclei [88].

As the film continues to grow, three main growth regimes occur: firstly, Frank-van der Merwe growth [89], a two-dimensional growth mode in which one complete layer grows after another; secondly, Volmer-Weber growth [90] which describes a growth in which three-dimensional islands form and finally Stranski-Krastanov growth [91], a mixed growth regime in which initially a complete covering layer grows on which three-dimensional islands grow [92]. Many factors influence which growth mode dominates in a particular evaporation. The substrate and the deposited material themselves play an important role but also external factors such as the evaporation rate, substrate temperature, film thickness and chamber atmosphere can play a crucial role [88].

Many approaches are used to monitor and control physical vapour deposition processes. One method which has become especially routine and it is often not even mentioned in publications is the quartz micro balance (QMB). It is typically used at the thermal sources to monitor the rate of evaporation of the different precursors or close to the substrate to monitor the rate of deposition. It consists of a thin disk of crystalline quartz. The resonance frequency of this disk is excited electrically and can measured very precisely. As material is deposited onto the disk and its mass changes, the resonance frequency changes. This frequency change can be used to very precisely measure the amount of material that has been deposited on the QMB [93]. The first quartz micro balance was used in this way by Günther Sauerbrey in 1959 [94]. It has since become ubiquitous as a tool in vacuum deposition processes but also beyond gravimetry to study anything that would change its surface-acoustic-wave behaviour. Examples are the study of polymer brushes, adsorbed proteins, cell cultures, contact mechanisms, adsorption on surfaces and properties of molecular assemblies [93].

3.2 Physical vapour deposition of metal Halide perovskite thin-films

The first time physical vapour deposition was used to deposit hybrid organic-inorganic metal halide perovskites for solar cells was in 2013 when Liu et al. co-evaporated methylammonium iodide (MAI) and lead chloride ($PbCl_2$) [10]. They were able to deposit smooth, planar, pin-hole free perovskite films. They then used these films in solar cells and achieved efficiencies of up to 15.4 %. They thereby not only demonstrated that it was possible to fabricate efficient vapour deposited perovskite solar cells, but they also demonstrated a simplified, planar solar cell architecture which does not require the use of mesoporous titanium dioxide. Since then a whole field of scientists studying co-evaporated perovskite thin-films and their application in solar cells has emerged.

Furthermore other solvent-free, vacuum-based deposition methods for perovskite films have emerged, including flash evaporation [85], 2-step evaporation [95] and chemical vapour deposition (CVD) [96].

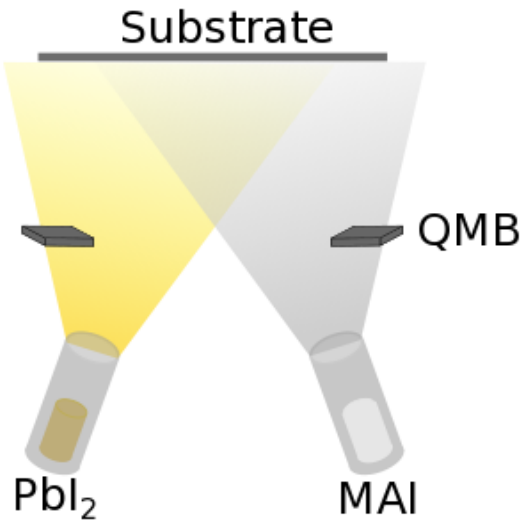


Figure 3.1: Schematic of a co-evaporation system. Two crucibles are controlled with quartz micro-balances (QMB) and mounted below a rotating substrate holder [97].

During co-evaporation, organic and inorganic precursors such as MAI and PbI_2 are heated simultaneously in separate furnaces in a vacuum chamber. The precursors condense on a substrate which is mounted above the sources. This results in the formation of polycrystalline perovskite films. Co-evaporated films are typically very uniform and pin-hole-free, [10, 97] over a large area which makes them ideal for the up-scaling of perovskite solar cells. The film thickness can also be controlled very accurately [98, 99]. Additionally, the substrate remains at low temperatures during the deposition which makes it possible to use heat sensitive substrates such as flexible foils [79]. Furthermore, vapour deposited films are extremely smooth, enabling fundamental studies which require

well-define interfaces and low light scattering [70, 100, 101]. In contrast to the more widely used solution-based deposition methods such as spin-coating [64, 72], doctor-blading [102, 103], two-step deposition [77] and solvent annealing [78], co-evaporation does not require any solvents. This makes it a particularly promising method for perovskite-perovskite tandem and multi-junction solar cells as it avoids the need for solvent orthogonality required during solution processing [104]. It also eliminates the need for the handling and disposal of large amounts of solvents in large-scale production.

Despite these advantages, co-evaporation has not been utilised by researchers as much as the solution-based spin-coating method. One reason is the need for a dedicated vacuum chamber and therefore higher investment needed to begin to use co-evaporation. Another crucial challenge has been the difficultly in reliably controlling the co-deposition process, in particular the rate control of the organic precursors such as MAI [105–107]. Researchers have struggled to overcome this challenge. While some workable solutions have been reported the underlying reasons why methylammonium iodide is so hard to evaporate controllably, have not previously been investigated in detail [108]. This problem, a better understanding of it and solutions are discussed in detail in chapter 5.6.

3.3 Co-evaporation of methylammonium lead iodide

Following first reported co-evaporated perovskite solar cells [10], the initial research focus was on the optimisation of co-evaporated $MAPbI_3$. A number of different solar cell layouts and contact materials were utilised. Especially noteworthy examples are by Polander et al. who not only studied the influence of several different evaporated hole transport materials on the solar cell efficiency but they also demonstrated a fully vacuum deposited $MAPbI_3$ solar cell [106]. Momblona et al. employed doped contact layers and were able to push the efficiency of a co-evaporated $MAPbI_3$ solar cell to 20.3 % [109].

Further studies focused on better understanding factors such as the substrate or the

precursor rates, which influence the perovskite deposition and film formation. Patel et al. simultaneously co-evaporated $MAPbI_3$ onto several different substrates to study their influence on the film formation, solar cell efficiency and J-V hysteresis [100]. To understand the influence of different precursor rates on the film formation, Borchert et al. employed a unique evaporation chamber with an in-situ X-ray diffraction system to monitor the formation of different crystallographic phases during the co-evaporation [110].

3.4 Moving beyond $MAPbI_3$ - new materials

After much of the work on evaporated perovskite thin-films for solar cells had focused on $MAPbI_3$, in the last few years other materials have successfully been evaporated and it has been shown that a wide range of hybrid perovskite materials can be co-evaporated.

First steps away from $MAPbI_3$ were made by investigating halides other than iodide. The so-called chloride route had been used to make $MAPbI_3$. In this approach, MAI and $PbCl_2$ are used as precursors to fabricated $MAPbI_3$ thin-films which, depending on the used rates, contain various amounts of chloride [107, 110]. Small amounts of chloride incorporation into $MAPbI_3$ thin-films seem to support film growth [10]. But $MAPbCl_3$ itself is unsuitable for solar cells as this material has a large bandgap and is transparent [107]. By varying the composition from $MAPbI_3$ to $MAPbCl_3$ one ought to be able to tune the bandgap, but this turns out to not be possible because of a miscibility gap which makes it impossible to reach useful intermediate iodide-chloride compositions [107].
In contrast with iodide-bromide such a miscibility gap has not been absorbed and the bandgap can be tuned by adjusting the ratio of iodide to bromide [116]. This was utilised by Longo et.al. to fabricate fully vacuum-deposited mixed-halide perovskite solar cells. These had a wide bandgap, suitable to use in tandem solar cells and reached power conversion efficiencies of up to 15.9 % [98]. In solution-processed solar cells, it had been shown that using not only a mixed composition for the X site in the perovskite

perovskite material	**cell architecture**	**perovskite thickness (nm)**	**active area (cm^2)**	J_{SC} (mA/cm^2)	V_{OC} (V)	**FF (%)**	**PCE (%)**	
$MAPbI_3$	ITO/C_{60}:PhIm/$C_{60}/CH_3NH_3PbI_3/$ $TaTm/TaTm{:}F_6-TCNNQ/Ag$	500	0.01	22.08	1.14	80	20.3	[109]
$MAPbI_3$	$FTO/TiO_2/CH_3NH_3PbI_3/$ Spiro/Ag	350	0.1	21.76	1.08	66.8	15.7	[111]
$MAPbI_3$	$FTO/TiO_2/PCBM/CH_3NH_3PbI_3/$ Spiro/Au	380	0.16	21.3	1.007	75	17.1	[112]
$MAPb(Br,I)_3$	ITO/C_{60} : PhIm/$C_{60}/CH_3NH_3Pb(Br,I)_3/$ $TaTm/TaTm:F_6-TCNNQ/Ag$	•	0.0653	17.3	1.11	82	15.9	[98]
$CsFAPb(Br,I)_3$	$ITO/C_{60}:PhIm/C_{60}/Cs_{0.5}(HC(NH_2)_2)_{0.5}Pb(Br,I)_3/$ $TaTm/TaTm:F_6-TCNNQ/Ag$	310	•	18.7	0.922	56	9.7	[113]
$CsFAMA(Br,I)_3$	ITO/C_{60} : PhIm/$C_{60}/$ $Cs_{0.5}(HC(NH_2)_2)_{0.4}(CH_3NH_3)_{0.1}Pb(Br,I)_3/$ $TaTm/TaTm:F_6-TCNNQ/Ag$	340	•	17.0	1.146	82	16.0	[113]
$FAPbI_3$	$FTO/C_{60}/HC(NH_2)_2PbI_3/$ Spiro/Ag	300	0.0919	22.1	1.01	•	15.8	[97]
$CsPbI_2Br$	$FTO/TiO_2/CsPbI_2Br/$ Spiro/Au	400	0.09	10.9	1.1	49	5.7	[114]
$CsPbI_3$	$ITO/PTAA/CsPbI_3/C_{60}/BCP/Cu$	450	0.16	18.1	0.96	73	12.5	[115]

Table 3.1: Overview of metal-halide perovskite solar cells fabricated using co-evaporation published since 2016. Abbreviations: ITO = Indium doped tin oxide, FTO: flouride doped tin oxide, PhIm = N1,N4-bis(tri-p-tolylphosphoranylidene) benzene-1,4- diamine, TaTm = $N4,N4,N4'',N''-$tetra([1,1′−biphenyl]−4−yl)−[1,1′ : 4′,″ −terphenyl]−4,″ −diamine, F6-TCNNQ = 2,2'-(perfluoronaphthalene-2,6-diylidene) dimalononitrile, spiro-OMeTAD = 2,2',7,7'- tetrakis(N,N-di-4-methoxyphenylamino)-9,9'-spirobifluorene, PTAA = poly(triaryl amine), BCP = bathocuproine.

but also in the A site cation leads to more stable and even more tuneable materials. A popular example is the triple-cation mixed halide perovskite $(CsFAMA)Pb(Br, I)_3$. An important step towards the co-evaporation of this material was to investigate if FAI can be evaporated controllably and to realise the co-evaporation of $FAPbI_3$. This crucial first step was achieved as part of this thesis and is reported in detail in Chapter 5. Subsequently, Gil-Escrig et al. were able to demonstrate the co-evaporation of $Cs_{0.5}FA_{0.4}MA_{0.1}Pb(I_{0.83}Br_{0.17})_3$ [113] and fabricated the first co-evaporated triple-cation halide perovskite solar cell.

Another strand of research into new perovskite materials for solar cells focuses on all inorganic perovskites. In these materials, the organic molecule on the A site is replaced with an inorganic element, most commonly caesium. Burwig et al. demonstrated that both $CsPbI_3$ and $CsPbBr_3$ can be deposited using co-evaporation. They also confirmed that these materials are thermally more stable than their organic counterparts and have complex phase behaviour including non-perovskite phases which are undesirable for solar cells [117]. Soon after, the first inorganic co-evaporated perovskite solar cell based on $CsPbI_2Br$ was fabricated [114]. At the time it only reached an efficiency of 5.7 %. Becker et al. used CsI and PbI_2 as precursors and deliberatly did not rotate the substrate. With this approach, they deposited thin-films with a graded composition from a CsI rich area to a PbI_2 rich area they studied how properties such as photoluminescence intensity and absorption coefficient changed with the composition and were able to identify ideal growth conditions to directly grow the desired γ- $CsPbI_3$ phase and fabricate solar cells with efficiencies of up to 12 % [115].

Particularly since 2016 it has been demonstrated that metal-halide perovskite materials other than $MAPbI_3$ can be evaporated successfully. An overview of all co-evaporated solar cell efficiencies reported in that time frame is shown in Table 3.1.

3.5 Co-evaporation enabling insights into fundamental material properties

Perovskite thin-films deposited via co-evaporation are remarkably planar and uniform. Furthermore, their thickness can be controlled very finely. These advantageous properties have enabled a range of studies which shed light on fundamental material properties of metal-halide perovskites. One of the earliest studies utilising evaporated thin-films to study the material properties of $MAPbI_3$ was conducted by Wehrenfennig et al. [66]. They studied the charge carrier mobility and lifetimes in these materials. Both are key parameters to predict the suitability of a material for solar cell and other optoelectronic devices. They found that both the charge carrier mobility and the lifetime were higher than for spin-coated $MAPbI_3$.

Patel et al. utilised the additive nature of deposition via evaporation to gain insights into the formation dynamics of $MAPbI_3$. He deposited a bilayer of PbI_2 and MAI onto a cooled substrate to prevent their inter-diffusion during the deposition. The samples were then placed at room temperature to observe the real-time formation dynamics of $MAPbI_3$ using visible light transmission, photoluminescence lifetime measurements and X-ray diffraction [101].

Olthof et al. [118] studied the substrate-dependence of the electronic structure and film formation of $MAPbI_3$ thin-films using co-evaporation. Thanks to the exceptional thickness control of this method, they were able to deposit films incrementally only adding a few nanometre at a time. Between each evaporation step, they performed UV photoelectron spectroscopy (UPS) and X-ray photoelectron spectroscopy (XPS) measurements. With this approach, they were able to observe the appearance of interface dipoles as well as band bending. They found a dependence of the bandedges of the perovskite on the substrate especially for thin films. Furthermore the substrate influences the film formation and how the perovskite forms in the initial deposited layers [118].

Looking beyond $MAPbI_3$, the work described in Chapter 5 enabled a further study by Davies et al. [70] who used evaporated $FAPbI_3$ thin-films to study the optoelectronic properties of $FAPbI_3$ in comparison to $MAPbI_3$. They found that the organic cation has more of an influence on the optoelectronic properties than anticipated. Especially the temperature dependence of the bandgap deviates strongly from what has been observed in $MAPbI_3$ [70].

All of these studies profited from the unique advantages of co-evaporation for the fabrication of metal-halide perovskite films. While some relied on the very planar films with little scattering, others utilised the additive nature of the deposition and the superior thickness control this method provides. As these examples show, vapour deposition has not only yielded efficient, scalable perovskite solar cells but has also made deeper insights into the underlying physics possible.

In summary, physical vapour deposition has long been a widely employed method to deposit thin-films of a large variety of materials. It has since 2013 been applied to deposit metal-halide perovskite thin-films for solar cells [10]. Initially, the focus of research into the co-evaporation of perovskite materials was on $MAPbI_3$ which yielded highly efficient solar cells and enabled studies into the material properties of $MAPbI_3$. Recently, other metal-halide perovskite materials have been deposited with co-evaporation, including mixed perovskites. Co-evaporation offers many advantages; especially its additive, scalable and solvent free nature. In the future, this deposition technique will play an important role for the fabrication of perovskite solar cells on an industrial scale.

4 Methods

4.1 Fabrication techniques

4.1.1 Co-evaporation of perovskite thin films

The primary deposition technique used throughout this thesis is vacuum deposition. Its development, advantages and applications are discussed in detail in Chapter 3. For the evaporations described in this thesis, a Kurt J. Lesker Mini Spectros evaporator was used. It is equipped with two independently controlled thermal sources and a temperature controlled substrate holder mounted above them. Each source and the substrate holder have their own shutter and quartz micro balance (QMB) to control the timing and rates of the deposition. A backing pump and a turbo pump are combined to evacuate the chamber, and pressures in the 10^{-6} mbar range are regularly reached. The chamber has several custom modifications, made in collaboration with the mechanical workshop of the Oxford Physics department, including additional heat shielding to reduce the influence of the thermal sources on each other and a steel door which is less susceptible to corrosion than the pre-installed aluminium door. In the thermal sources, alumina crucibles are used into which the precursors are placed. These crucibles can easily be removed from the thermal sources. For each precursor, a dedicated crucible is used to

avoid cross contamination of different precursors. An important recent addition to the chamber is a Hiden Analytical quadrupole mass-spectrometer.

4.1.2 Deposition of contact layers

To fabricate a functioning solar cell, it is necessary to have a mechanism that separates the generated charges. One way to achieve charge separation is the use of selective contact layers that transport one of the charged species and block the other. This approach is commonly employed in organic solar cells and perovskite solar cells which are based on a p-i-n junction layout. These selective layers have to fulfil a number of requirements, including, but not limited to, suitable band alignment with the absorber, good charge transport, homogeneous and close contact with the absorber, as well as chemical stability [57].



Figure 4.1: Example layer stack as used for planar perovskite solar cells. The bottom layer is fluoride doped tin oxide (FTO) which is a transparent conductor on a glass substrate (not shown). This is followed by C_{60} as a electron transport layer. The middle layer is the perovskite absorber which is followed by a doped Spiro-OMeTAD layer and finally a silver or gold electrode.

For all solar cells fabricated for this thesis, a standard solar cell layout was used which is shown in Figure 4.1. An overview over the steps needed to fabricate a solar cell is shown in Figure 4.3. First, the FTO substrate is thoroughly cleaned using aceton and

isopropanol, then the electron transport material is deposited. The electron transport layer is C_{60} which is deposited in the same vacuum chamber as the perovskite thin-film. Zhao et al. have previously reported the successful fabrication of perovskite solar cells using vapour deposited C_{60} as the electron-transport material [119]. This same procedure was adopted for this evaporation system and successfully implemented to fabricate solar cells with high performance, low hysteresis and good reproducibility. Initially a deposition rate for C_{60} had to be established and a series of evaporations with varying length was performed. In this way, C_{60} films with a variety of thicknesses were obtained. These were then used in standard $MAPbI_3$ perovskite solar cells and changes in the cell performance observed, as shown in Figure 4.2. In this optimisation series the highest power conversion efficiency was seen with a deposition time of 1400 s which results in a around 50 nm thick film. The champion cell had a stabilised efficiency of 15.4 %.

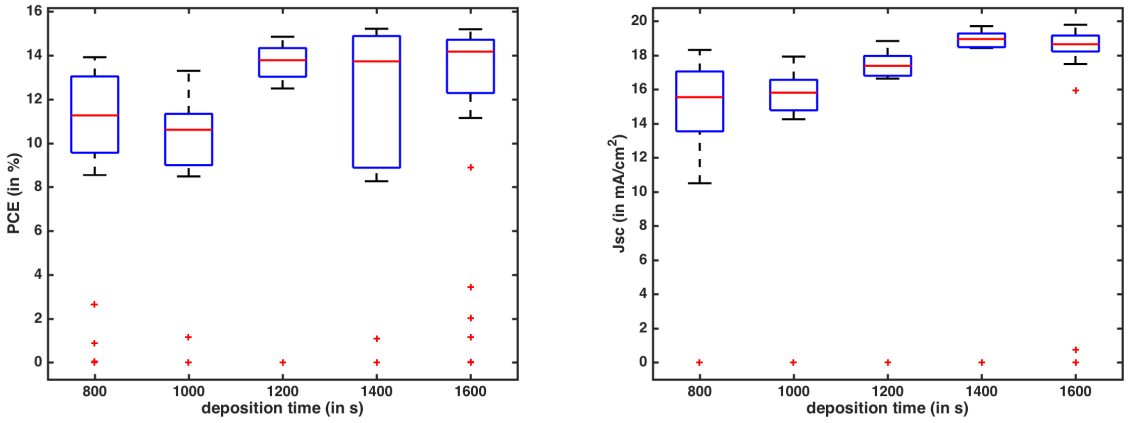


Figure 4.2: The power conversion efficiency (left) and short circuit current (right) of the solar cells changes with the C_{60} deposition time.

The C_{60} was directly deposited onto the fluoride doped tin oxide (FTO) without the commonly used TiO_2 layer. Eliminating this layer is advantageous since TiO_2 requires a high temperature sintering step which is incompatible with substrates such as plastic or fabric. Furthermore, high temperature steps are a major challenge for up-scaling.
Using vapour deposited C_{60} makes it possible to avoid the use of TiO_2 and the problems

associated with spin-coating the transport layer such as uneven films, pinholes and undissolved particulates depositing on the film.

On the other side of the perovskite thin-film, 2,2',7,7'-Tetrakis-(N,N-di-4-methoxyphenylamino)-9,9'-spirobifluorene (Spiro-OMeTAD) is used as the hole transport layer. For all solar cells in this thesis, Spiro-OMeTAD from Lumtec was used. It was doped with lithium bis(trifluoromethanesulfonyl)imide (LiTFSI) and 4-tert-Butylpyridine (tBP) and spin coated at 2000 rpm for 45 s. Finally, 100 nm of silver were evaporated in a second evaporation chamber to form the contacts and complete the solar cells. The size of the evaporated metal contacts defined the area of the solar cells as 0.0919 cm^2.

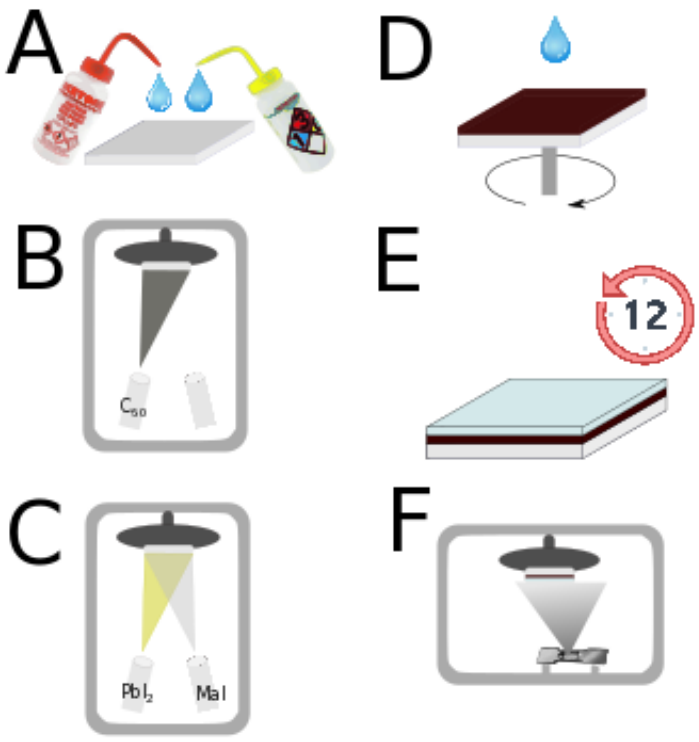


Figure 4.3: Overview over the steps used to fabricate solar cells. A) The FTO substrate is thoroughly cleaned. B) A C_{60} layer is deposited. C) The perovskite layer is co-evaporated. D) Doped Spiro-OMeTAD is spincoated onto the perovskite. E) The sample is left in dry air for 12 h to oxidise and dope the Spiro. F) The top metal electrode is evaporated to complete the cell.

4.2 Solar cell characterisation

4.2.1 J-V curves

To test the performance of solar cells, their current density against voltage is measured. This can be done both when the cell is unilluminated (dark current) and while illuminating it with simulated solar radiation. Without illumination, the solar cell shows rectifying behaviour, like a diode. Under forward bias (V>0), a large current can pass, while in reverse bias (V<0) only a small current can flow [20]. Under illumination, an additional photocurrent (J_{ph}) is generated which leads to a shift of the JV curve as shown in figure 4.4.

$$J(V) = J_{\mathrm{SC}} - J_{\mathrm{dark}}(V) \tag{4.1}$$

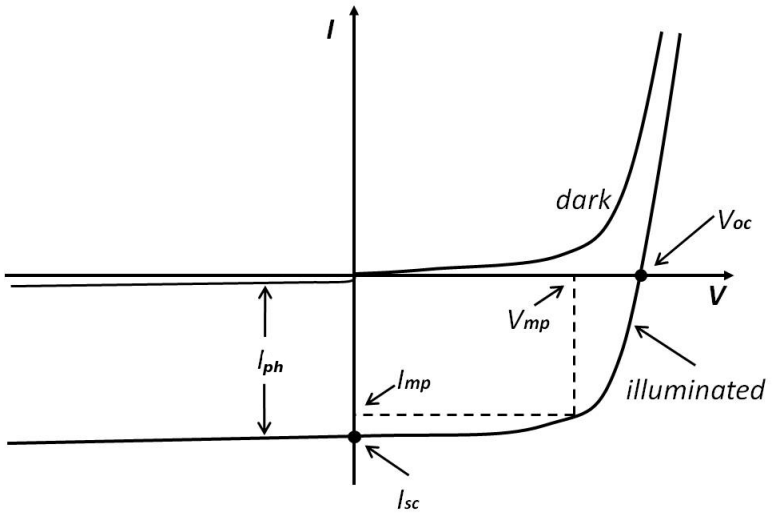


Figure 4.4: Current-Voltage curves of a solar cell in the dark and under illumination.

For J-V measurements, the solar cell is illuminated with light simulating the intensity and spectrum of sun light. The Sun's spectrum is that of a black-body emitter, filtered by the Sun's outer layers and the earth's atmosphere (compare Section 2.1.1.1). With a solar simulator, the aim is to simulate this spectrum as closely as possible. The solar cell is exposed to this simulated solar light and the load is varied to scan the whole J-V curve. There are four key parameters that can be extracted from a JV curve to characterise the

solar cell. These are J_{SC}, V_{OC}, FF and η. When no load is applied to the cell, the short circuit current J_{SC} flows. This is the maximum value the current can reach. Likewise, if the contacts are isolated, no current flows and the highest possible potential difference builds up. This is called the open circuit voltage V_{OC}. Another parameter that can be extracted from a JV curve is the power density P. A solar cell delivers power in a range of biases from 0 to its V_{OC}. In this range, the power is given by equation 4.2.

$$P = JV \tag{4.2}$$

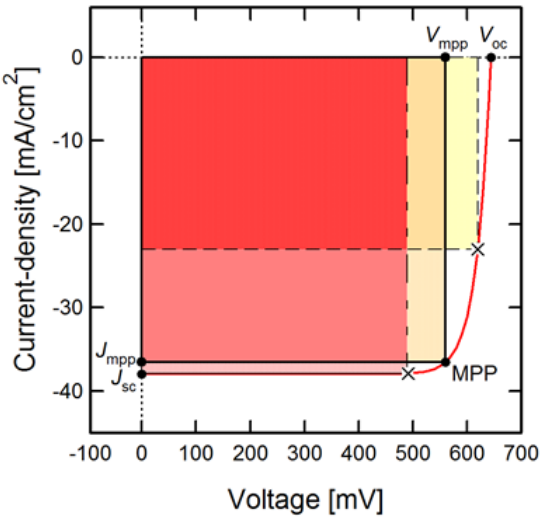


Figure 4.5: A typical J-V curve under illumination [120]

P reaches a maximum at the so-called maximum power point (MPP) (see 4.5). The voltage V_{MPP} and current density J_{MPP} at the maximum power point can be used to calculate the fill factor, using formula 4.3. The fill factor is the ratio of the maximum operational power over the theoretically possible maximum output. It describes how "square" the JV curve is [20].

$$FF = \frac{J_{\mathrm{m}} V_{\mathrm{m}}}{J_{\mathrm{SC}} V_{\mathrm{OC}}} \tag{4.3}$$

Another parameter which can be extracted from a JV curve is the power conversion efficiency (PCE) also often called efficiency η. It gives the fraction of the incident light power density (P_s) which is converted to electrical power by the solar cell. It is calculated according to formula 4.4.

$$\eta = \frac{J_{SC} V_{OC} FF}{P_s} \tag{4.4}$$

When measuring the J-V curves of perovskite solar cells, often-times, a dependence on the scan direction and scan speed has been observed. How pronounced this hysteretic behaviour is, appears to depend both on the properties of the absorber and on the transport and contact materials used. For example, it has been reported that in solvent annealed perovskite layers with very large crystal grains, no hysteresis could be observed [121].

Several possible explanations for this hysteresis have been proposed, including ferroelectricity [122], charge accumulation on the interfaces [123], the filling of traps in the surface or on interfaces [124], or ion migration [125].

Associated with the hysteresis is a slow transient of 10 s to up to 100 s before a steady state is reached in current or voltage measurements. To be able to compare results from different laboratories, it is important to report preconditioning, such as light or voltage biasing, scan rates and scan directions used for J-V measurements. All of these factors can greatly influence the shape of the J-V curve and the solar cell efficiency calculated from it [125]. Care has to be taken to measure perovskite cells properly to avoid an overestimation of the power conversion efficiency. It has been shown that this is a common problem with a high number of publications reporting a higher J_{sc} from their JV measurements than could be calculated from the EQEs of their cells [126].

One approach to circumvent the measurement problems described above is the use of stabilised power conversion efficiencies for comparisons. It was proposed to report the

stabilised power output close to the maximum power point, alongside the JV-curves. To measure a stabilised PCE, the solar cell is held at a constant voltage, close to the maximum power point, until the current stabilises [124]. This typically takes several tens of seconds. The stabilized power conversion efficiency is typically, but not always, lower than the power conversion efficiency calculated from a relatively fast JV scan.

4.2.2 External quantum efficiency (EQE)

The external quantum efficiency (EQE) is defined as the probability that a photon with energy E incident on the cell, will result in an electron being delivered to the external circuit. The EQE is usually measured and plotted as a function of the wavelength or the energy of the incoming photon. The relation between the short circuit current and the external quantum efficiency is given by equation 4.5, where q is the electronic charge and $b_s(E)$ the density of the incident spectral photon flux [20]. The EQE depends on several properties of the solar cell: the absorption coefficient of the absorber material, the efficiencies of the charge separation and the charge collection. Therefore, a lot of information about a solar cell can be obtained from the shape of its EQE. For example the bandgap of the absorber material can be determined from the EQE or problems with the window layer can be diagnosed.

$$J_{SC} = q \int b_s(E)\, QE(E)\, dE \tag{4.5}$$

In standard EQE measurements the solar cell is illuminated with monochromatic light with a varying wavelength and the response recorded. The intensity of this light is usually small, so that the resulting signal is hard to detect. To overcome this, a chopper and lock-in-amplifier are used in order to detect the signal. The wavelength is varied, using a broadband light source and a monochromator. Since the intensity of the incoming light is not the same for each wavelength, it is necessary to know the intensity distribution of

the light source. This is measured using a calibrated reference solar cell. The use of a monochromator to generate the different wavelengths for the measurement, successively, takes a considerable amount of time, resulting in relativity slow measurements. This can present a problem if the sample changes over the course of the measurement or many samples need to be measured. To speed the EQE measurements up, a Fourier transform photo current spectroscopy (FTPS) approach can be used instead. FPTS utilises instruments commonly used for Fourier transform infrared spectroscopy (FTIR) measurements and modifies them to measure the spectral response of a solar cell. It is a fast and sensitive method which has been successfully used to study a variety of solar cells, including micro-crystalline silicon solar cells [127], organic and hybrid solar cells [128]. It allows for fast and very sensitive measurements of the external quantum efficiency [129]. The output beam of an FTIR spectrometer is used to illuminate a photovoltaic device, which replaces the regular detector. The spectrum of the incoming light is measured beforehand with a calibrated photodetector and used as a reference. Comparing the reference and the signal from the photovoltaic device, the photocurrent's dependence on the wavelength can be determined [127].

In summary, many methods to fabricate as well as characterise perovskite thin-films and solar cells have been employed in this thesis. A particular focus was the co-evaporation of metal-halide perovskite thin-films and the matching contact layers. Solar cell characterisation with JV curves and external quantum efficiency measurements was of special importance as it provides direct feedback on the quality and usability of the fabricated films. Other techniques that were used are photo-lithography, scanning electron microscopy, atomic force microscopy and optical microscopy, as well as spectroscopy in the infra-red and visible range of the spectrum. Furthermore, THz-spectroscopy,

transmission electron microscopy, nuclear magnetic resonance and ion-milling were utilized in collaboration with other researchers.

5 Vapour Deposited Formamidinium Lead Triiodide

5.1 Introduction and background

Methylammonium lead triiodide ($CH_3NH_3PbI_3$ = $MAPbI_3$) has been the most commonly used and investigated perovskite solar cell material. However, more recently formamidinium lead triiodide ($CH(NH_2)_2PbI_3$ = $FAPbI_3$) and other perovskites containing formamidinium have attracted interest as they offer a number of advantages over $MAPbI_3$. Specifically, $FAPbI_3$ has a narrower bandgap of 1.47 eV which results in an extension of the absorption into the near infrared [130], and $FAPbI_3$ also exhibits better thermal stability than $MAPbI_3$ [131]. Mixed-cation perovskites combining formamidinium and other cations such as methylammonium or caesium have been shown to be even more thermally stable [132, 133]. Furthermore, using both mixed cations and mixed halides enables stable perovskites such as $Cs_aFA_bMA_{1-a-b}Pb(I_xBr_{1-x})_3$ with a widely tuneable bandgap [134]. $FAPbI_3$ thin-films have been fabricated using a variety of methods, spin-coating from solution being the most common [131, 135]. Another successful route is based on predeposited PbI_2 films which are converted into $FAPbI_3$ by dipping in solutions containing FAI [130]. Finally, it has also been demonstrated that $FAPbI_3$ thin-films can be grown in

a chemical vapour deposition (CVD) furnace [96]. As discussed in Chapter 3, vacuum based deposition processes such as co-evaporation are advantageous because they result in highly uniform, pin-hole free, smooth thin films [10]. Pin-hole free films are particularly important for large-area solar cells in order to avoid short circuits between electron and hole transport layers that limit PCEs and fill factors. Good thickness uniformity and low roughness are important for reliable solar cell production and these also facilitate advanced optoelectronic characterisation of the material [10]. Additionally, vacuum based deposition does not require solvents, thus it is an ideal method for depositing perovskite thin films in multi-layer stacks and on sensitive substrates. This is particularly useful for the fabrication of tandem solar cells [133, 136] and solar cells on flexible substrates.

In this chapter, the fabrication of $FAPbI_3$ thin-films using co-evaporation is presented. It is shown that it is possible to use co-evaporation to fabricate efficient $FAPbI_3$ solar cells and large-area thin-films. This is a crucial step towards the realisation of co-evaporated mixed cation perovskite solar cells.

5.2 Sample preparation

5.2.1 Preparation of the $FAPbI_3$ layer

The $FAPbI_3$ layer was fabricated in a modified Kurt J. Lesker dual source evaporation system described in Section 4.1.1. PbI_2 and FAI were heated in separate crucibles until each of them evaporated. During evaporation, the pressure in the chamber was 10^{-6} mbar. The evaporation temperature for FAI was 150 °C, and PbI_2 evaporated at 300 °C. The vapours condensed on a rotating substrate that was mounted above the sources. The rotation helps ensure uniform coating. To obtain thin-films for PL spectroscopy [69], THz spectroscopy [137], ultraviolet-visible spectroscopy and infrared spectroscopy [138], this deposition was carried out on z-cut quartz or KBr crystals as substrates. All $FAPbI_3$ layers were annealed at 170 °C for 1 min.

After this annealing step the film was in the desired, dark, perovskite phase. Unfortunately, exposure to humid air can trigger a phase transition to the yellow non-perovskite phase. This meant that the perovskite film had to be kept in the glovebox as much as possible and steps had to be taken to minimise the time the films spent outside of the glovebox.

5.2.2 Preparation of the full solar cell

The solar cells were fabricated on a fluoride-doped tin oxide (FTO) coated glass substrate. The FTO was cleaned using a multi-step cleaning protocol that involved being scrubbed with Hellmanex solution, sonication in acetone and isopropanol and cleaning with oxygen plasma. C_{60} was evaporated onto these clean FTO substrates in the same evaporation system which was used for the perovskite deposition. C_{60} with a purity of 99.9 % was bought from Acros Organics and evaporated at 350 °C [119]. The perovskite layer was deposited onto this as described above. Next, 2,2',7,7'-Tetrakis-(N,N-di-4-methoxyphenylamino)-9,9'-spirobifluorene (Spiro-OMeTAD) from Lumtec was spin-coated as the hole extraction layer. Spiro-OMeTAD was doped with Lithium bis(trifluoromethanesulfonyl)imide (LiTFSI) and 4-tert-Butylpyridine (tBP) and spin coated at 2000 rpm for 45 s. Finally, 100 nm of silver was evaporated in a second evaporation chamber to complete the solar cells. The size of the evaporated metal contacts defined the area of the solar cells as 0.0919 cm^2.

5.3 Solar cell performance

To characterise the performance of the solar cells, both current density-voltage sweeps (JV-curves) and external quantum efficiency measurements were performed.

5.3.1 Current-Voltage sweeps (J–V)

A solar simulator was used to illuminate the solar cells and measure their current-voltage (JV) characteristics. A typical JV-scan for a champion cell is shown in 5.1. The measurement was performed both in forward and in reverse directions. A large difference between these measurements is observed. This phenomenon is seen in many kinds of perovskite solar cells and is known as hysteresis [124, 125]. From the JV scan, the power conversion efficiency (PCE) of the device can be calculated. The PCE of the champion device was 15.8 % during the reverse scan. The hysteresis makes it hard to choose a consistent way to determine the PCE from JV scans of different devices. To avoid this problem, stabilised power conversion efficiencies were measured as well.

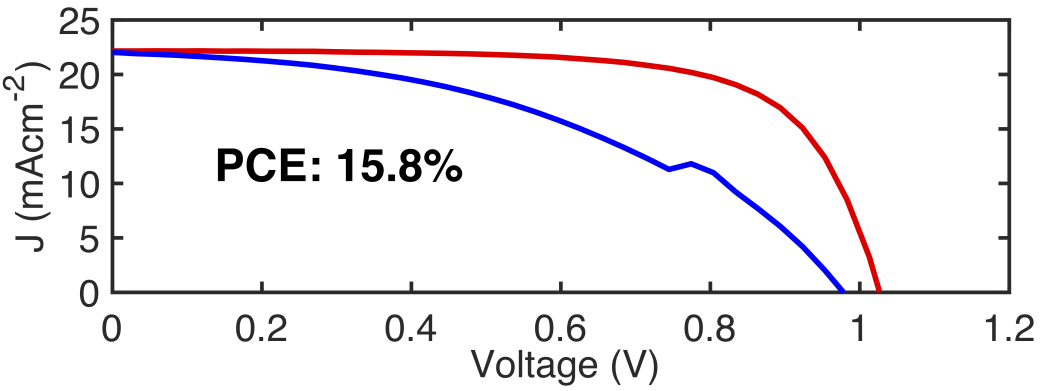


Figure 5.1: Current–voltage (J–V) measurement of the champion $FAPbI_3$ solar cell. The short-circuit current density (J_{SC}) was 22.1 $mAcm^{-2}$, the open–circuit voltage (V_{OC}) 1.01 V, and the power conversion efficiency (PCE) 15.8 %. Hysteresis is observed between the forward (blue) and reverse (red) scans. (Used with permission from [97])

5.3.2 Stabilised power output (SPO)

To measure the efficiency of the solar cells, stabilised power output (SPO), measurements in addition to the standard JV-sweeps were used. The solar cell was held close to the maximum power point for 50 s, while the current and efficiency are recorded. The SPO measurement for the champion cell is shown in 5.2. After an initial rise, the stabilised efficiency stayed at around 14 % and reached a value of 14.2 % and the current

stabilised at 17 mAcm^{-2}. Cells that have a large hysteresis commonly also have a relatively long rise time in the SPO measurement, before a stable current and efficiency are reached. This is also the case in the devices presented here. During the SPO measurement shown in Figure 5.2, it takes about 5 s before the current and power conversion efficiency rise to a stable level.

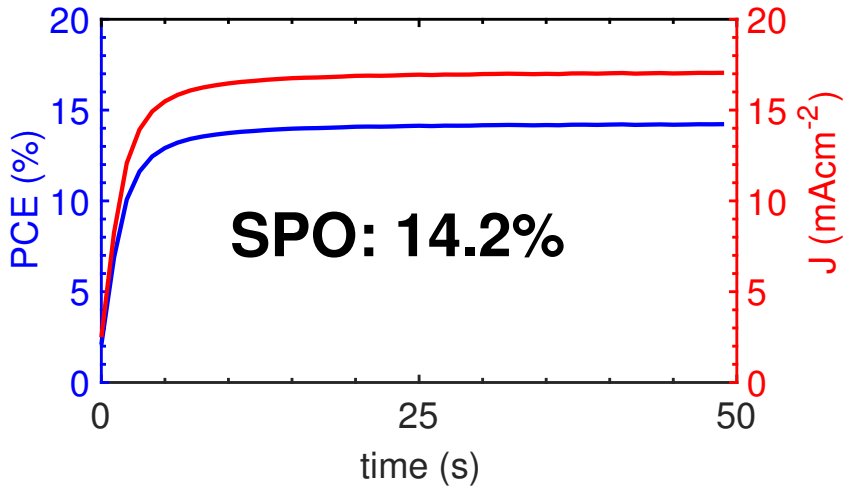


Figure 5.2: For the stabilised power output measurement (SPO), the voltage was held constant for 50 s and the current was measured. A stabilised efficiency of 14.2 % (blue) and a stabilised current of 17 mAcm^{-2} (red) was measured. (Used with permission from [97])

5.3.3 Spread of solar cell efficiencies

The performances of the solar cells in one batch are often not exactly equal, but a spread does occur. This can be seen in Figure 5.3. The PCEs of all the cells of the best batch are plotted in a histogram. Some cells have very low efficiencies, possibly due to shorts. Shorts occur whenever the layer structure of the solar cell is disrupted and the top and bottom electrode come into direct contact. This can happen for many reasons, for example if dust particles settle on one of the layers during fabrication or the spincoating of the hole transport layer is not uniform enough. Fortunately, many cells do reach high efficiencies, around 14 % and 15 %. The efficiencies from the reverse scans are generally higher than those of the forward scans.

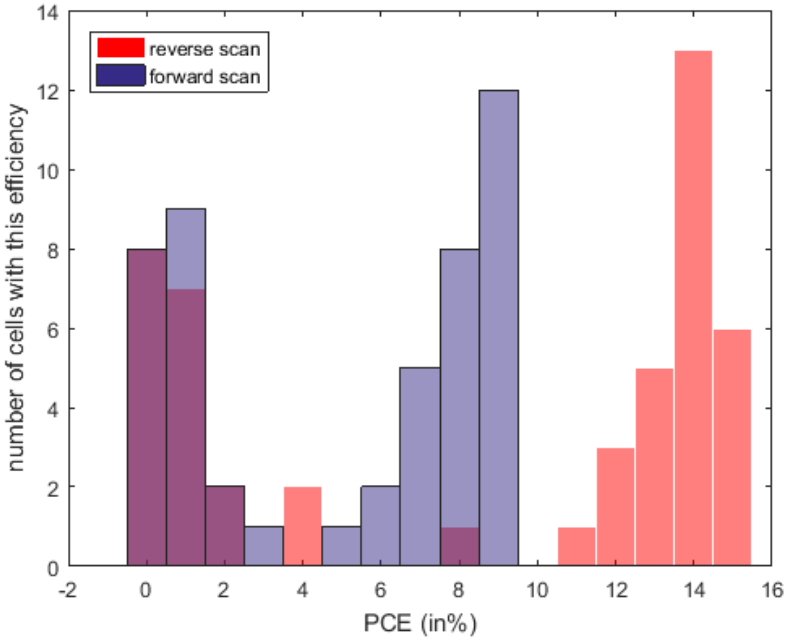


Figure 5.3: An overview of the efficiencies of all cells produced in the same batch as the champion solar cell is shown. Some devices perform very poorly which is likely due to shorts in these cells. Many cells do reach high efficiencies of 14 % and 15 % in the reverse scan. (Used with permission from [97])

5.3.4 External quantum efficiency (EQE)

The external quantum efficiency (EQE) spectrum of the champion device was measured in short circuit conditions under 1 Sun (1 kW/cm^2 AM 1.5) illumination (see Figure 5.4). The Fourier transform photo current spectroscopy (FTPS) approach [127] is used making it possible to measure the full EQE spectrum in a very short measurement. For this, a Bruker Vertex 80v interferometer was combined with a Newport Oriel Sol3A class AAA solar simulator as the light source and the solar cell acted as the detector. A Newport calibrated silicon reference solar cell was used as the reference.

The EQE peaks at 80 % and shows high values over the wavelength range 400 nm - 600 nm. However, a drop in EQE to values around $\sim$60 % is observed for wavelengths between 600 nm and the $FAPbI_3$ band-edge. In this area of the spectrum, a thicker $FAPbI_3$

layer could further improve the PCE of the devices as long as efficient charge collection can be maintained in the thicker films. The integrated current over the spectrum is 19 $mAcm^{-2}$ which is close to the J_{SC} recorded in the J–V measurements: 22 $mAcm^{-2}$ for both the forward and reverse scan, and 17 $mAcm^{-2}$ stabilised (see section 5.3.1) [97].

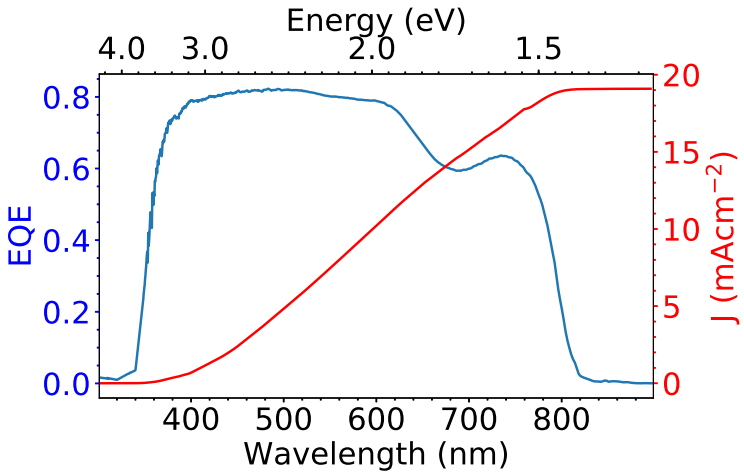


Figure 5.4: The external quantum efficiency (EQE) spectrum (blue) of the champion device and the integrated current over the EQE spectrum (red) were measured using the Fourier transform photo current spectroscopy approach. The integrated current over the full spectrum was 19 $mAcm^{-2}$. (Used with permission from [97])

Overall, fabrication of solar cells with a high PCE was achieved. These cells stabilised at similarly high efficiencies. This result shows that vapour depositing $FAPbI_3$ yields efficient solar cells in a relatively simple, planar cell architecture.

5.4 Film quality

The quality of the deposited films is crucial for the fabrication of solar cells and for the reliability of the material properties determined from measurements on these samples. Therefore, it is important to obtain high quality thin films. Measures used to assess the film quality are the uniformity of the film across the sample, the chemical composition of the film and its crystallinity.

5.4.1 Uniformity of deposition

5.4.1.1 Uniformity on the microscale

One major advantage of co-evaporation over solution-based deposition techniques for hybrid organic-inorganic perovskite thin films is the tremendous uniformity and smoothness of the co-evaporated films on the micro-scale. It is particularly important to avoid the formation of pin-holes; it is even more so when fabricating large-area solar cells to avoid short circuits between electron and hole transport layers that limit PCEs and fill factors. It has been shown before that low roughness can be achieved for $MAPbI_3$ and is important for reliable solar cell production and also enables advanced optoelectronic characterisation of the material [10]. To see if similar smoothness was achieved for $FAPbI_3$, atomic force microscopy (AFM) measurements were performed to assess the uniformity of the films in the micro-scale. The $FAPbI_3$ was deposited onto a glass microscope slide. For comparison, both the microscope slide and the perovskite film were measured. Both AFM micrographs are shown in Figure 5.5. The roughness of the film is only $R_{RMS} = 6.2\,nm$, which is much lower than the surface roughness of $FAPbI_3$ thin films produced by other methods with reported roughness values ranging from 18 nm [139] to above 100 nm [140]. The film was also very homogeneous without any pinholes.

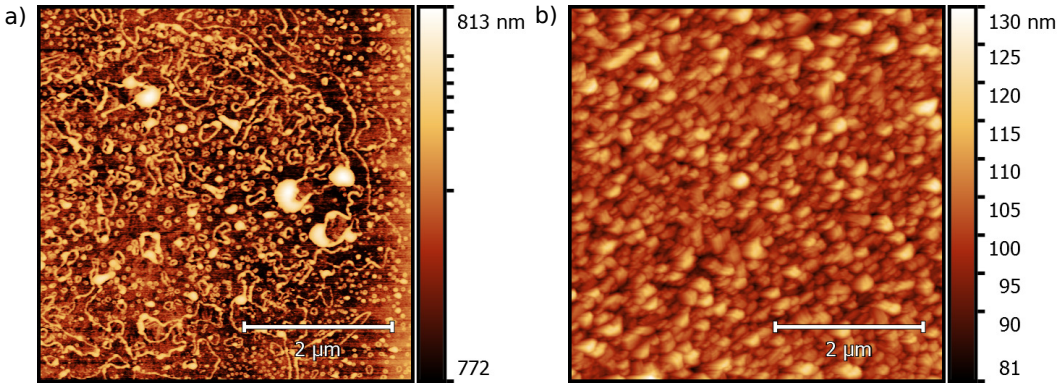


Figure 5.5: a) Atomic force micrograph of a $5\,\mu m \times 5\,\mu m$ region of a plain glass microscope slide. The root-mean-square roughness R_{RMS} of the plain glass is 2.7 nm b) Atomic force micrograph of a $5\,\mu m \times 5\,\mu m$ region of a $FAPbI_3$ thin film deposited onto a glass slide. The surface was found to be very smooth with a root-mean-square roughness $R_{RMS} = 6.2\,nm$. (Used with permission from [97])

To learn more about the micro-structure of the absorber layer and the stacking of all the layers of the solar cell, cross-sectional scanning electron microscopy measurements (SEM) (Figure 5.6) were used and in collaboration with Dr Laura Martínez-Maestro transmission electron (TEM) measurements (Figure 5.7) were performed. In both of them it is evident that the different materials are stacked on top of each other in planar layers. No evidence of pinholes or gaps in the films is found. The $FAPbI_3$ film is uniform in thickness and very smooth.

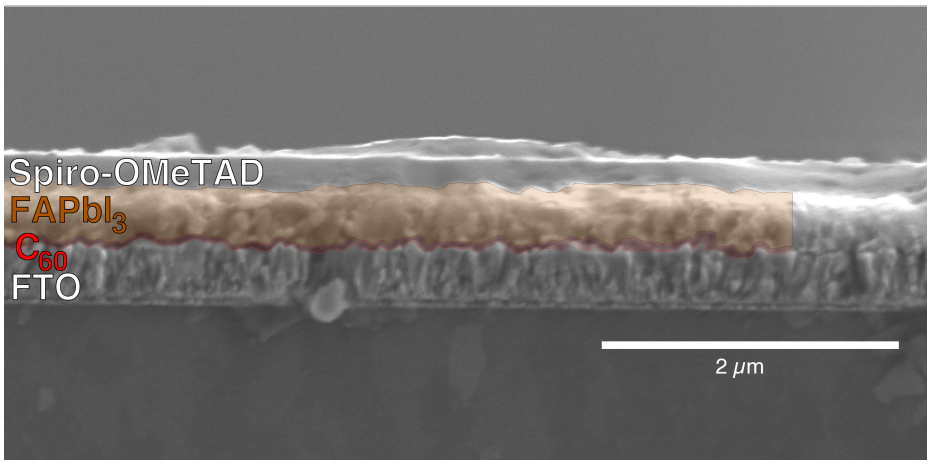


Figure 5.6: A scanning electron microscopy image (SEM) of a complete $FAPbI_3$ solar cell. From the bottom, the layers are a glass substrate, fluorine doped tin oxide (FTO) layer, thin C_{60} layer, $FAPbI_3$ layer, a spiro-OMeTAD layer, and the silver electrode. (Used with permission from [97])

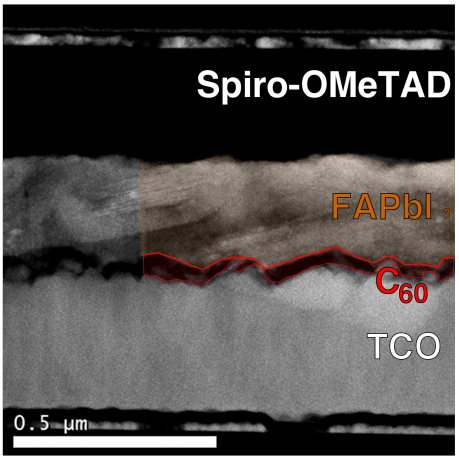


Figure 5.7: A transmission electron microscopy (TEM) image of a complete $FAPbI_3$ solar cell (taken by Dr Laura Martínez Maestro). From the bottom, the layers are a glass substrate, fluoride doped tin oxide (FTO) layer, thin C_{60} layer, $FAPbI_3$ layer, a spiro-OMeTAD layer, and finally, the silver electrode. (Used with permission from [97])

In addition to microscopy, optical methods were used to assess the smoothness and composition of the deposited perovskite films. A Fourier transform infrared spectrometer (Bruker Vertex 80v) was used to measure the reflectance (R) and transmittance (T) spectra of the evaporated $FAPbI_3$ thin film. The following combination of sources and detectors were used for the measurements: a tungsten halogen lamp with a silicon detector for the visible region ($> 1.25\,eV$); a tungsten halogen lamp and a liquid nitrogen-cooled HgCdTe (MCT) detector for the near-infrared (NIR) region ($1.25 > E > 0.46\,eV$); and a globar source and MCT detector for the mid-infrared (MIR) region ($< 0.46\,eV$). This data is shown in Figures 5.8 and 5.11 and was used to determine the absorption coefficient (α) from the visible to the infrared. To calculate the absorption coefficient the formula $\alpha = (1/d)\ln(T/(1-R))$ was used. Very little scatter below the onset of absorption is observed in the absorption, transmission and reflection spectra (Figure 5.8).

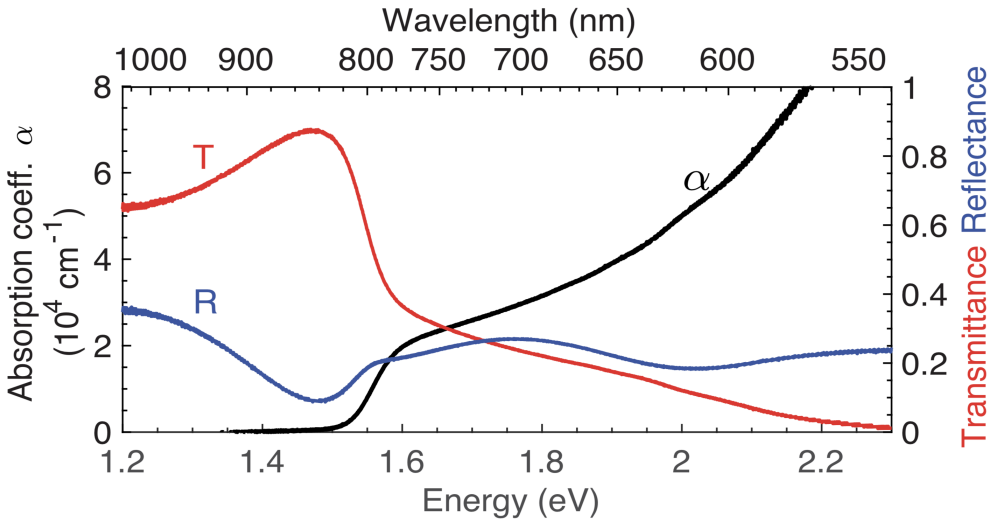


Figure 5.8: Absorption (black line) of the coevaporated $FAPbI_3$ thin films in the visible is calculated from the transmission (red line) and reflection (blue line) spectra. The transmission and reflection were measured by Dr Christopher Davies. As expected, an absorption onset around 1.5 eV is observed. (Used with permission from [97])

In conclusion, the three microscopy techniques, AFM, SEM and TEM as well as the reflection, transmission and absorption spectra demonstrate that the films are smooth and pinhole free on a micro-scale.

5.4.1.2 Uniformity on the macroscale

Planar thin film solar cells, like the ones studied in this thesis, all rely on the uniformity and continuity of the different layers of their stack. Gaps in the films, variation in thickness and pinholes would negatively influence the performance and reproducibility of thin film solar cells. The uniformity over large scales is not crucial in small lab scale solar cells, but it proves vital for larger, up-scaled devices. It is especially important to be able to deposit a uniform absorber layer over a large area when a larger active area is needed for the fabrication of a full module.

To assess the uniformity that can be achieved with this deposition method, a $FAPbI_3$ thin film was deposited onto a large substrate. The area of this film was 8 cm by 8 cm. The substrate holder was rotated during the co-evaporation to ensure a uniform deposition. A Dektak profilometer was then used to assess the uniformity of the thickness of the deposited perovskite film. The thickness was measured in three areas, the centre of the sample and two corners (see Figure 5.9). In each area, several measurements were taken to improve the accuracy of the measurement. All of the measured thicknesses are shown in Figure 5.10. In the centre, the film was 370 ± 20 nm thick. The thickness decreased towards the corners of the substrate to 330 ± 20 nm. This slight variation in thickness is expected given the relatively small working distance of only 20 cm between the thermal evaporation sources and the substrates. It could be reduced by using an evaporator with a larger working distance.

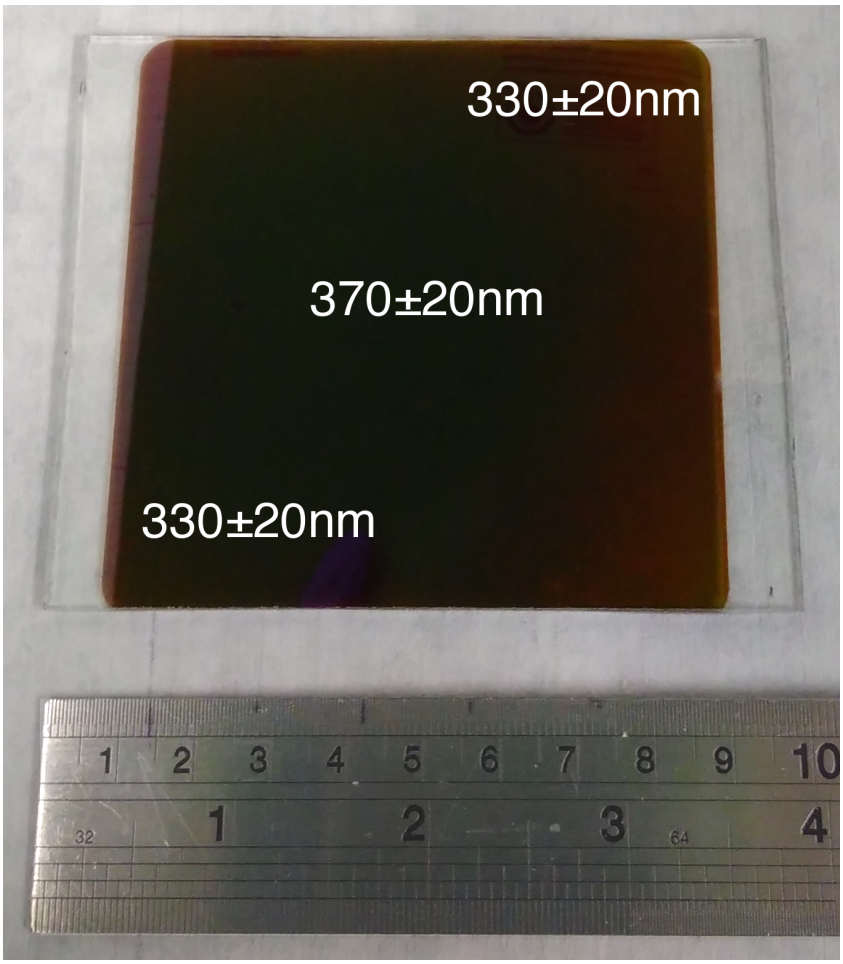


Figure 5.9: Photograph of a 64 cm^2 thin film of $FAPbI_3$ which was deposited on a glass sheet. The sample was annealed on a hotplate for 1 minute at 170 °C. The average measured thicknesses from 3 areas are superimposed on the image. A centimetre scale is pictured for size comparison. (Used with permission from [97])

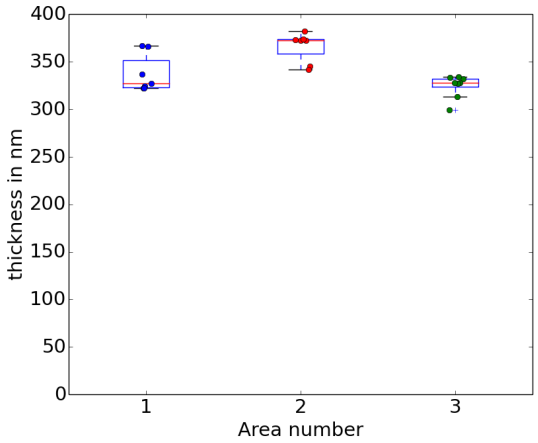


Figure 5.10: Profilometer measurements were taken in three areas on the film. The bottom left corner (1), the middle (2) and the top right corner (3). Several measurements were taken in each area and the median of them was used as the thickness of the film in that area. (Used with permission from [97])

Overall, the thickness of the large film was highly uniform. This is promising for the up-scaling of this deposition technique. Especially since an increased working distance between substrate and sources could reduce the thickness variation even more and would be easy to implement on an industrial scale set-up.

5.4.2 Chemical composition of the thin film

To assess if the chemical composition of the thin films was as expected, infrared spectroscopy was performed on $FAPbI_3$ co-evaporated onto KBr substrates (Figure 5.11). Of particular interest was the possible presence of contaminations from previous evaporations. The vacuum chamber in which the evaporation was performed had previously been used to evaporate various other materials including methylammonium iodide (MAI), lead chloride ($PbCl_2$) and fullerenes. In the MIR absoprtion spectrum the characteristic features of $FAPbI_3$ were present: the peak at $1713\,cm^{-1}$ matches the C=N stretch in the FA^+ cation and the peaks at $3269\,cm^{-1}$ and $3406\,cm^{-1}$ correspond to the N-H stretching vibrations [141, 142]. None of the characteristic peaks for $MAPbI_3$

were observed. This confirms, that $FAPbI_3$ was successfully deposited and no significant contamination from materials previously deposited in the same vacuum chamber occurred.

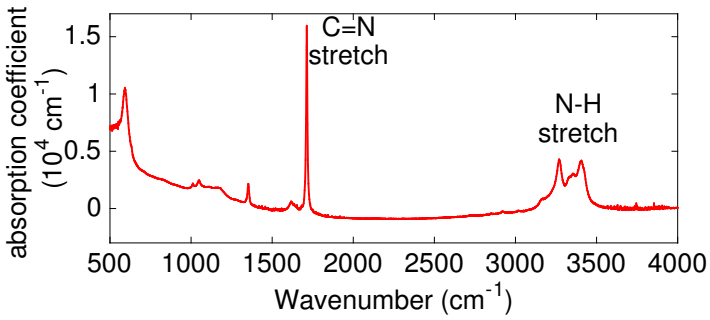


Figure 5.11: The infrared absorption spectrum of the film showing the characteristic absorption peaks for $FAPbI_3$. (Used with permission from [97])

5.4.3 Crystallinity of the thin film

To determine the phase and crystal quality of the deposited films, X-ray diffraction (XRD) patterns were measured using a Panalytical X'pert powder diffractometer with a copper X-ray source. Figure 5.12 shows the XRD patterns of as-deposited and annealed $FAPbI_3$ thin films.

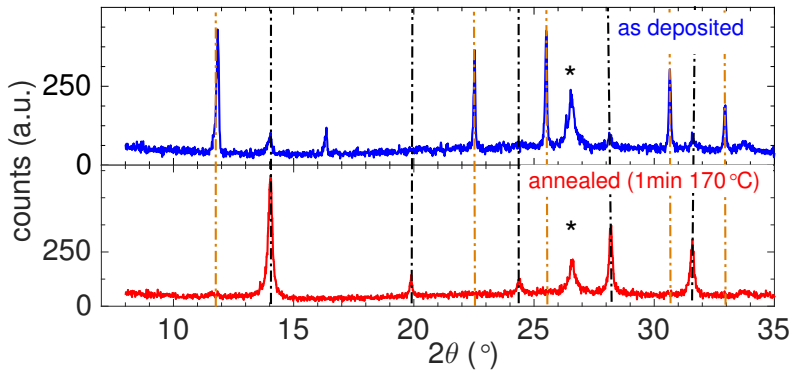


Figure 5.12: The X-ray diffraction pattern for an as-deposited and for an annealed film. The copper Cu Kα X-ray line was used. The orange lines mark the expected position corresponding to the yellow non-perovskite $\delta - FAPbI_3$ phase, whereas the black dashed lines mark the peaks matching the perovskite $\alpha - FAPbI_3$ phase [6]. The FTO substrate peak is marked with a star. (Used with permission from [97])

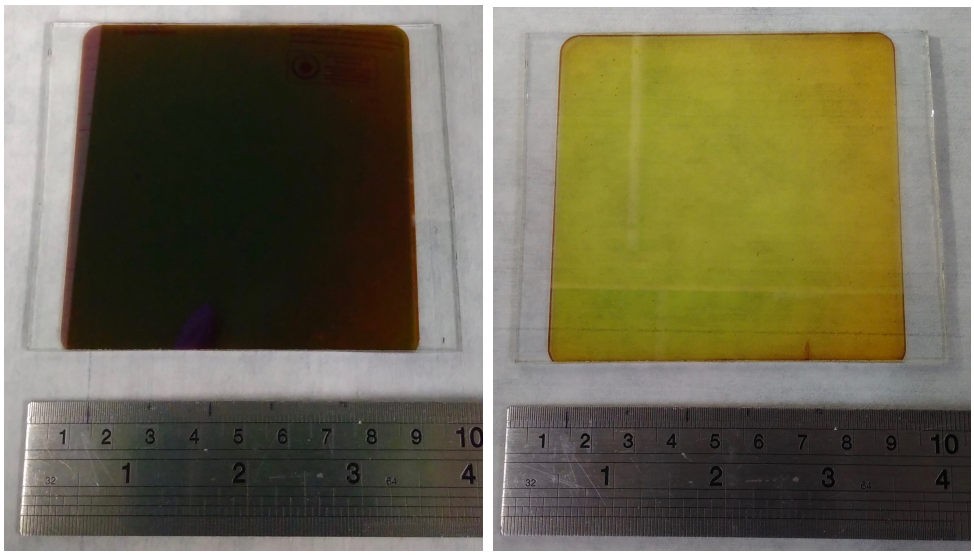


Figure 5.13: Photographs of the same thin film of $FAPbI_3$ before (left) and after (right) exposure to humid air. The phase transition from the brown perovskite phase to the yellow non-perovskite phase has taken place. (Used with permission from [97])

From the literature, it is known that at room temperature, $FAPbI_3$ can be either in a black, trigonal, perovskite phase or in a yellow, hexagonal, non-perovskite phase [6, 143]. Only thin films in the black phase are suitable for use as absorbers in solar cells, hence it is necessary to ensure that the film is in the right phase. The diffraction patterns are shown in Figure 5.12 and confirm that after 1 minute of annealing at $170\,^{\circ}C$ the material was in the black perovskite $\alpha - FAPbI_3$ phase. In the annealed sample, all X-ray reflections are consistent with this α structure, however in the as-deposited (unannealed) sample, the intensity of the perovskite peaks is strongly reduced, and the most intense peaks are consistent with the yellow, non-perovskite δ phase of $FAPbI_3$ [6]. This confirms that in the as-deposited film, the yellow $\delta - FAPbI_3$ is dominant and upon annealing it is converted to the black $\alpha - FAPbI_3$ phase. In evaporated $MAPbI_3$ thin films, annealing is not necessary to obtain high solar cell efficiencies [100] because there are no competing non-perovskite $MAPbI_3$ phases. In contrast, in the case of $FAPbI_3$ annealing is essential in order to obtain the perovskite phase. Overall, the same phase behaviour as has been reported for solution processed $FAPbI_3$ [143] and single crystals

[6], was also found for co-evaporated films. Interestingly for evaporated $FAPbI_3$ thin films, only a very short annealing is necessary to obtain the desired α-phase. The phase transition can be strikingly observed with the naked eye. In Figure 5.13, a large, annealed $FAPbI_3$ film is shown. It initially has a dark colour which after exposure to humid air turns yellow as the film transitions to the $\delta - FAPbI_3$ phase.

5.5 Optoelectronic properties

For the efficient operation of solar cells and other optoelectronic devices it is important to understand the optoelectronic properties of the used materials. Especially the charge carrier mobility and recombination dynamics are of importance. To measure these properties, photoconductivity measurements in the terahertz (THz) range and photoluminescence measurements were conducted. The THz measurements were conducted in collaboration with Dr Rebecca Milot. The film was excited with 35 fs laser pulses with different fluences. For the excitation, an amplified laser system (Spectra Physics, Millennia – Tsunami – Empower – Spitfire) with a centre wavelength of 800 nm, repetition rate of 1 kHz, average pulse energy of 1 mJ, and pulse duration of 40 fs was used. Approximately 50 % of the initial laser power was used to generate and detect THz, and the remaining 50 % was used for the photoexcitation of the sample. THz radiation was generated using optical rectification in a 450 μm thick GaP (110) crystal and detected via free-space electro-optic sampling in a ZnTe chip with 200 μm ZnTe (110) on 3 mm ZnTe (100). The sample was photoexcited at 400 nm following frequency doubling in a β-barium borate (BBO) crystal. All of the measurements were performed with the sample and the entire THz beam path in vacuum.

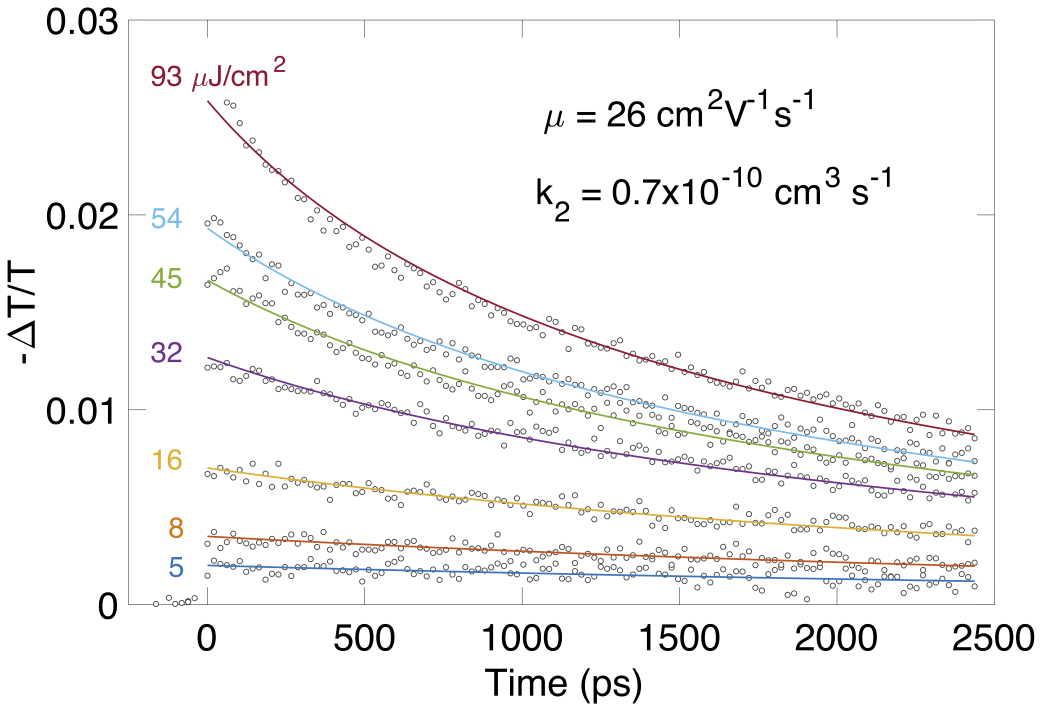


Figure 5.14: Measurements of the charge-carrier recombination dynamics in evaporated $FAPbI_3$ thin film on z-cut quartz. Optical pump / THz probe measurements were performed by Dr Rebecca Milot. The sample was photoexcited with a wavelength of 400 nm and various fluences ranging from 5 - 93 $\mu J/cm^2$ as labelled on the graph. The open circles represent experimental data points, while the solid lines are fits to the data using Equation 5.1. (Used with permission from [97])

The measured change of photoconductivity of a $FAPbI_3$ thin film after photoexcitation is shown in Figure **??**. The data were fitted using Equation 5.1, where n is the charge-carrier density, k_3 is the Auger recombination rate constant, k_2 is the bimolecular (electron-hole) recombination rate constant and k_1 is the monomolecular recombination rate. The constant k_3 was set to zero for the fitting because the excitation fluences were not high enough to measure it. Additionally, k_1 was set according to the rate determined from the PL measurements.

$$\frac{dn}{dt} = -k_3 n^3 - k_2^{\text{apparent}} n^2 - k_1 n \tag{5.1}$$

Using these fits, the charge-carrier mobility was determined to be to be 26 $cm^2V^{-1}s^{-1}$ and an apparent [144] bimolecular recombination rate constant of $k_2^{\text{apparent}} = 0.7 \times 10^{-10}\,cm^3s^{-1}$

was extracted. Comparing these results to those determined for solution-processed $FAPbI_3$ films [7, 67], they are nearly identical. Using the measured carrier lifetime and mobility, a charge carrier diffusion length [67] of 360 nm is calculated for a charge-carrier density typical for this material under solar illumination ($10^{15}cm^{-3}$) [7]. This is longer than the thickness of our $FAPbI_3$ layer and therefore long enough to allow the charges to migrate to the interfaces with the charge transport layers. These THz measurements show that the evaporated $FAPbI_3$ possesses good charge conduction properties, comparable with the perovskite materials used in high efficiency solar cells.

The photoluminescence (PL) measurements on these films were performed by fellow DPhil student Adam Wright. The PL spectrum of a co-evaporated and annealed $FAPbI_3$ film is shown in the inset of Figure 5.15. The PL peak is at a wavelength of approximately 805 nm (1.54 eV) in agreement with previous reports for solution-processed $FAPbI_3$ [6, 131, 145]. The full width at half-maximum (FWHM) of the PL spectrum for the co-evaporated sample was 79 meV, which is slightly narrower than the 88 meV previously reported for a solution-processed sample [145]. Figure 5.15 shows the measured time-resolved PL transient fitted with a stretched exponential function in order to account for a superposition of exponential decays [100, 146]. The average monomolecular lifetime τ of these decays is 2 ns, which is significantly lower than that typically reported for solution processed $FAPbI_3$ films [67, 131, 147]. Our measured lifetimes are similar to previously reported lifetimes for vapour deposited $MAPbI_3$ films [100]. Optimisation of deposition parameters to increase the PL lifetime offers another opportunity to improve the efficiency of solar cells based on these films, which despite the very short PL lifetimes, show remarkably high power conversion efficiencies.

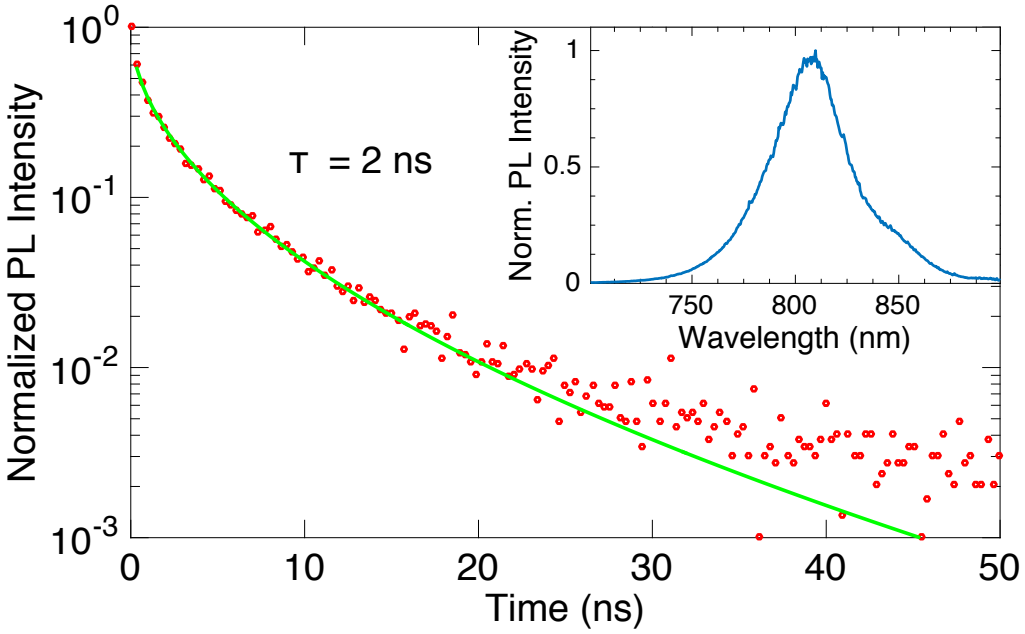


Figure 5.15: Photoluminescence (PL) from an evaporated $FAPbI_3$ thin film was measured by Adam Wright. The PL decay is fit using a stretched exponential function to extract an average monomolecular charge-carrier lifetime of 2 ns. The PL spectrum shown in the inset has a peak at 805 nm (1.54eV). (Used with permission from [97])

5.6 Summary and conclusion

The first co-evaporated $FAPbI_3$ thin films and solar cells are presented in this chapter. It is demonstrated that uniform films can be deposited with a roughness of only $R_{RMS} = 6.2$ nm. These smooth films are utilised to fabricate efficient $FAPbI_3$ solar cells with power conversion efficiencies of around 15 %. This is an important step on the way towards evaporated mixed perovskite solar cells. These were subsequently demonstrated by Gil-Escrig et al. [113] who realised an evaporated $Cs_{0.5}FA_{0.4}MA_{0.1}Pb(I_{0.83}Br_{0.17})_3$ solar cell. In this chapter, a wide range of characterisation methods were used to study the optoelectronic properties of $FAPbI_3$, the film quality, and the solar cell performance. These measurements reveal that the charge carrier lifetimes are comparable to those of other evaporated metal halide perovskites and the apparent bimolecular recombination rate is nearly identical to that reported for solution processed $FAPbI_3$. A combination of

microscopy techniques (AFM, SEM and TEM) as well as absorption spectroscopy in the infra-red and visible spectrum demonstrate that the deposited films possess the desired composition and are smooth and uniform in thickness. The planarity of these high quality $FAPbI_3$ thin films was subsequently utilised by my collaborators Christopher Davies and Adam Wright who used these thin films in studies which further illuminate the properties of $FAPbI_3$. Christopher Davies studied the impact which the formamidinium cation has on the optoelectronic properties of $FAPbI_3$ [70] and Adam Wright used these films to study quantum oscillations in bulk halide perovskites [148].

6

Influence of Impurities on the Co-evaporation of $MAPbI_3$

6.1 Introduction and motivation

As discussed in Chapter 4, the majority of research on metal halide perovskite solar cells has concentrated on methods that are solution-based such as spin-coating [64, 72], doctor-blading [102, 103], two-step deposition [77] and solvent annealing [78]. In contrast, vapour co-deposition is currently underutilised. This is in large part due to the difficulty in reliably controlling the co-deposition process, in particular the rate control of the organic precursors such as MAI has been a challenge [105–107].

The research presented in this chapter will show that the reliable production of $MAPbI_3$ thin films via co-evaporation of MAI and PbI_2 is critically dependent on impurities within the organic (MAI) precursor. The focus is on two impurities MAH_2PO_3 and MAH_2PO_2, as they are both commonly found in MAI powders as by-products of MAI synthesis [149]. These impurities are found to have a dramatic effect on the control and regulation of the deposition rate of MAI with quartz micro balances (QMBs) (for more on QMBs, see Chapter 3). While the impurities affect the control of the deposition process, little impact

on device performance was found. These results help explain the difficulties researchers have faced in controlling metal halide perovskite co-deposition and lead to proposals for more reliable deposition methodologies to overcome these problems. In addition, these results indicate that high-purity precursors are not required to vapour deposit solar cells with reasonable power conversion efficiency.

Several different strategies have been reported previously to control and monitor the evaporation rate of MAI during co-evaporation. Quartz micro balances (QMB) are commonly used to monitor the growth rate of evaporated thin films [94]. For the deposition of $MAPbI_3$ QMBs facing the MAI crucible have been employed [10, 100], as well as QMBs which are deliberately turned away from the crucible to measure the pressure in the chamber instead of the direct deposition rate [81, 150]. A third approach utilises a standard pressure gauge to measure the chamber pressure to control the MAI deposition [106, 110, 119]. The two latter approaches are often adopted after the standard QMB rate measurement could not be successfully employed to monitor and control the MAI deposition.

Many authors report difficulties determining the rate of MAI vapour-deposition with standard QMBs. For example, Malinkiewicz et al. [105] commented that they were unable to calibrate the QMB sensor by measuring the thickness of the deposited MAI film. Borchert et al.[110] noted that the MAI rate can often not be properly recorded using a QMB and Zhao et al.[119] similarly reported that they experienced difficulty calibrating and monitoring the MAI rate with a QMB, and therefore decided to monitor the pressure instead. Unfortunately, the chamber pressure can depend on many factors, for example small leaks in the chamber, residual water and other chemicals outgassing from the chamber walls and volatile impurities in the precursors. Therefore, it is not possible to draw a straight-forward connection between the chamber pressure and the rate of MAI

evaporation. A wide range of chamber pressures during evaporation has been reported, from around 3×10^{-3} mbar [81] to as low as 3×10^{-6} mbar [100] with many groups reporting values in the $10^{-4} - 10^{-5}$ mbar range [99, 106, 107, 110, 119, 151]. Neither process monitoring with QMBs nor via the chamber pressure led to fully satisfactory control and reproducibility. Another challenge for co-evaporation is the relatively small crystallite size in the deposited polycrystalline perovskite films in comparison to some solution processing approaches. Despite the typically small crystallite size in evaporated films, high performing solar cells have been fabricated from them. Nevertheless, it has been speculated that an increase in crystallite size may further the performance of evaporated perovskite solar cells.

Levchuk et al. [149] have reported that impurities can improve the crystallite size in solution processed perovskite thin-films. This inspired the here reported investigation into the influence of impurities on evaporated films. Two MAI (methylammonium iodide) batches of different purity were used to deposit $MAPbI_3$ thin films: one high-purity MAI batch and one low-purity MAI batch which contained impurities MAH_2PO_3 and MAH_2PO_2. Both of these impurities have a lower melting point than MAI. MAH_2PO_2 is a viscous liquid at room temperature and MAH_2PO_3 melts around 60 °C [149]. In the vacuum chamber, MAH_2PO_3 evaporates around 55 °C, which is well below the evaporation temperature of MAI. Both MAI batches were characterised in detail using nuclear magnetic resonance (NMR) measurements and infra-red absorption spectroscopy. To understand the influence of the impurities on co-evaporation of methylammonium lead triiodide ($MAPbI_3$) precursor fluxes were monitored using an in situ residual gas analysis system (RGA) and QMBs. The deposited films were also characterised using X-ray diffraction (XRD) and scanning electron microscopy (SEM). Finally, solar cells were fabricated and their performance studied. Together these data explain the origin of

the problems faced in previous studies in controlling MAI flux and hence $MAPbI_3$ layer quality and reproducibility. This understanding opens a pathway for more reliable and reproducible methods for co-deposition of metal halide perovskite semiconductors.

6.2 Methods

A large variety of methods was used to study the influence of impurities on the co-evaporation of $MAPbI_3$. Nuclear magnetic resonance (NMR), infra-red spectroscopy and mass-spectroscopy were used to characterise the precursors. X-ray diffraction, scanning electron microscopy (SEM) and infra-red spectroscopy were used to characterise the deposited films and J-V measurements and cross-sectional SEM were used to study the completed solar cells. The typical deposition techniques for the perovskite films and the contact layers have been discussed in previous chapters (see Chapter 3.5, and Section 2.2.2.3); methods unique to this study are discussed below.

6.2.1 Solar cell fabrication

$MAPbI_3$-based solar cells were fabricated to assess the impact of the impurities on the solar cell performance. To fabricate the solar cells, a standard layout was used. The substrate was float glass coated with fluoride-doped tin oxide (FTO). A thin layer of C_{60} was evaporated on top. The C_{60} deposition was carried out in the same evaporation chamber as the later perovskite deposition. The $MAPbI_3$ layers were co-evaporated on top. As Figure 6.16 shows, the thickness of the perovskite layer in the champion devices was between 810 nm and 850 nm. A layer of Spiro-OMeTAD was spin-coated on top from a solution of 73 mg/ml Spiro-OMeTAD in chlorobenzene with a spin speed of 2000 rpm for 45 s. To dope the Spiro-OMeTAD, 38 μl of 170 mg/ml lithium bis(trifluoromethanesulfonyl)imide (LiTFSi) in 1-butanol was added, as well as 21 μl of 4-tert-butylpyridine. This layer stack was then left in a dry atmosphere overnight before 100 nm of silver were evaporated

with a Lesker Nano36 evaporator to finish the solar cell. To optimise the efficiency of the solar cells the deposition time and therefore the thickness of the $MAPbI_3$ absorber layer were varied. In Figure 6.1, the champion efficiency from each evaporation run is shown. The optimal deposition time when using the high-purity MAI was higher than when the low-purity MAI was used. But as shown in Figure 6.16, despite this difference, the thickness for the two best solar cells was the same.

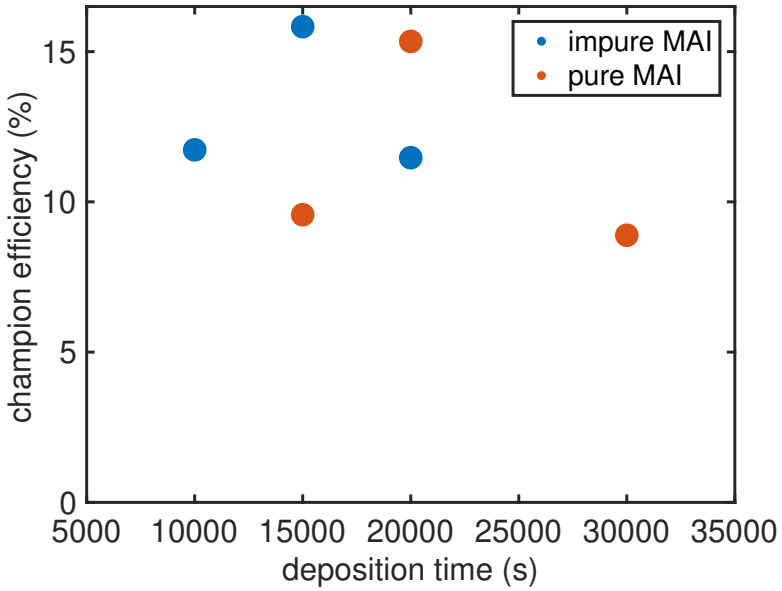


Figure 6.1: Deposition time optimisation for co-evaporations using two different MAI batches. Low-purity MAI in blue and high-purity MAI in red. Nearly the same champion efficiency is reached but after different deposition times (used with permission from [152]).

As a result of the thickness optimisations, nearly equal champion efficiencies were achieved with both high-purity and low-purity MAI. To show the cell performance beyond the champion device, the scanned efficiencies of all the cells of the batches that included the champion cell are plotted in histograms shown in Figures 6.2 and 6.3. The only noteworthy difference is the slightly higher number of solar cells that completely failed in the batch made with low-purity MAI.

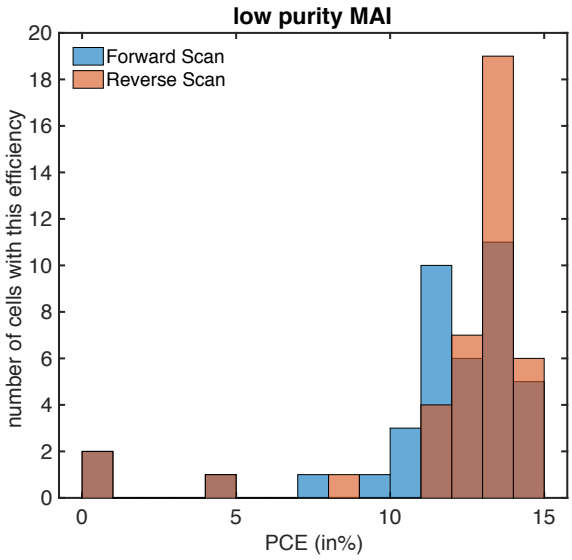


Figure 6.2: Power conversion efficiencies of all solar cells produced in the same batch as the champion device for low-purity MAI. A large number of cells reach high efficiencies of up to 15% (used with permission from [152]).

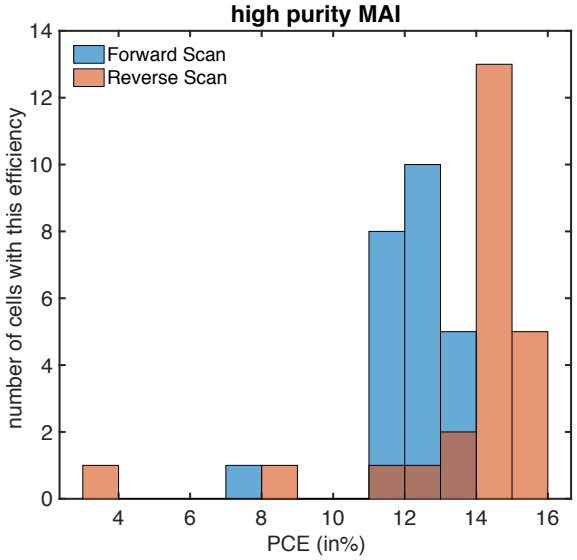


Figure 6.3: Power conversion efficiencies of all solar cells produced in the same batch as the champion device for high-purity MAI. A large number of cells reach high efficiencies of around 15% (used with permission from [152]).

6.2.2 Stabilised power output measurement

For the J-V sweeps and the stabilised power output measurements (SPO), an ABET class AAB Sun 2000 simulator was used. Black masks were used to achieve a well-defined active area and to prevent influences from light scattering. Hysteresis in the J-V

curves of perovskite solar cells is a commonly observed phenomenon. To obtain reliable efficiency measurements independently of possible hysteresis, stabilized power output (SPO) measurements are used. For these measurements, the solar cell is held close to the maximum power point (MPP) for 50 s while the current and efficiency is measured. The SPO curves for both the champion device fabricated with low-purity MAI and with high-purity MAI are shown below. The SPOs are very similar for both MAI batches.

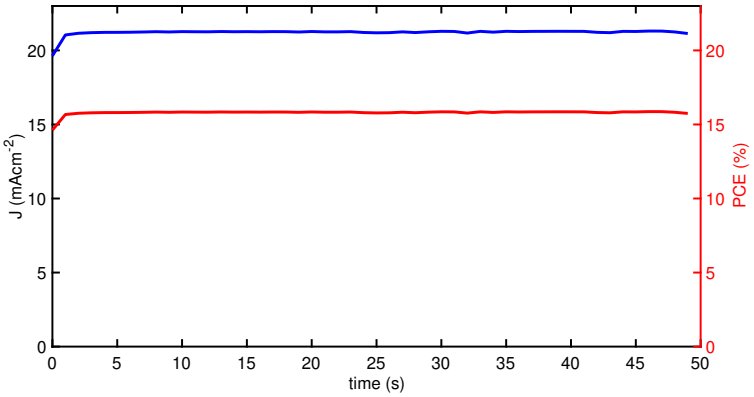


Figure 6.4: Stabilised power output of the champion solar cell from the best deposition run with low-purity MAI (used with permission from [152]).

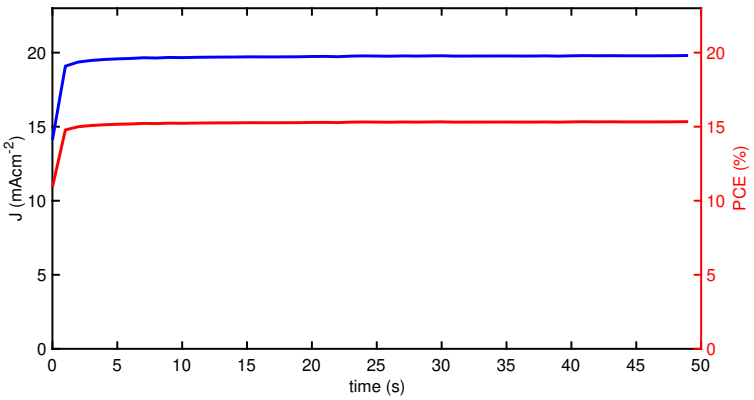


Figure 6.5: Stabilised power output of the champion solar cell from the best deposition run with high-purity MAI (used with permission from [152]).

6.2.3 In-situ mass spectroscopy

Only a few mass spectroscopy studies relating to MAI or $MAPbI_3$ have been reported in the literature. Most of these studies have focused on the decomposition of $MAPbI_3$

[153, 154], while Baekbo et al. performed combined QMB and mass spectrometry measurements, finding that MAI has a low sticking coefficient and appears to decompose into CH_3NH_2 and HI on the way from the crucible to the substrate [155].

To monitor the composition of the gas remaining in the chamber during evaporation, we used a residual gas analysis system with a Hiden Analytical quadrupole mass spectrometer. The mass spectrometer is connected to the back of the chamber where it samples the residual gas in the chamber. It contains a filament which ionises the molecules and two detectors. For the measurements shown in this chapter, the Faraday detector was used for the lower masses and the secondary electron multiplier (SEM) detector for the higher masses. This splitting of the measurement range made it possible to optimally use the different capabilities of the detectors. The Faraday detector is more robust and can cope with relatively high pressures but it is not sensitive enough for masses that are only present in very small quantities. In contrast, the SEM detector is more sensitive and can pick up masses that are only present in low concentrations; the SEM cannot be used if the partial pressure of the measured mass is too high and it also looses sensitivity over time which makes the application of increasing voltages to the SEM detector necessary to compensate for this. The lower mass range had several strong peaks, for example the nitrogen peak at 28 AMU/e. To avoid damage to the SEM detector this lower range was measured with the Faraday detector and the higher masses, where more sensitivity was needed, were measured with the SEM detector. The ranges for each of the detectors were chosen so that there was a small overlap of masses that were measured by both detectors. These masses were later used to correct for differences in the partial pressures measured by the two different detectors.

To be able to correctly assign the peaks in the mass spectrum to their parent molecules reference spectra are necessary. Some relevant spectra were available from databases but some had to be measured specifically for this study. The details of these measurements

are given in section 6.3.1.2. A significant hurdle to a conclusive analysis and interpretation of the mass spectroscopy data was the lack of reference files for most of the relevant materials. The mass spectroscopy library of the US National Institute of Standards and Technology did not contain entries for MAI or any of the relevant impurities. The only useful entries were those for methylamine (MA) and iodine (I). Similarly, no fitting reference spectra were found in the literature. This made it very hard to identify which peak originated from which material. Furthermore, it was unclear at what point the molecules had broken apart. It could not be determined if the molecules dissociated during the thermal evaporation, or stayed intact and where only subsequently split apart as they were being ionised for measurement in the mass spectrometer.

6.2.4 Synthesis of methylammonium iodide and the impurities

The high-purity MAI, low-purity MAI and the impurities MAH_2PO_2 and MAH_2PO_3 were synthesized by Ievgen Levchuk from Christoph Brabec's group at the University of Erlangen-Nürnberg.

6.2.4.1 Methylammonium synthesis

The high-purity methylammonium iodide was synthesised by mixing HI and methylamine (CH_3NH_2) in ethanol at room temperature. Compared to the commonly used standard diethyl ether/ethanol purification process [31, 32, 156, 157] this material was recrystallised three times from hot solutions of ethanol. Finally, fine, but large flakes of highly crystalline MAI were obtained and used as the standard high-purity material. In a 500 mL flask, 27.86 mL CH_3NH_2, 40 % in methanol, was mixed with 100 mL of ethanol. Then, at room temperature, 30 mL 57 % HI (contains < 1.5 % H_3PO_2 as stabiliser) in H_2O was added dropwise under continuous stirring. The obtained solution was placed in a rotary evaporator at 60 °C to remove all solvents. Then, after washing with diethyl ether several times, MAI was dissolved in ethanol and precipitated twice with diethyl ether. To obtain

single crystals, MAI was dissolved in 80 mL of hot ethanol and placed in a refrigerator at −3 °C for crystallisation. Large flakes (up to 7 mm) were obtained. The synthesis of standard methylammonium iodide with diethyl ether purification only, contains a higher level of impurities (low-purity MAI) and is described elsewhere [31, 32, 156, 157].

6.2.4.2 Synthesis of neat impurities

For the synthesis of methylammonium hypophosphite (MAH_2PO_2), 8.7 mL of 50 % H_3PO_2 in H_2O was mixed with 100 mL of ethanol. Then 29 mL CH_3NH_2 (40 % in methanol) was slowly added under continuous stirring. After 10 min, solvents were extracted by a rotary evaporator at 60 °C. The then obtained highly viscous liquid was diluted with ethanol and separated from ethanol by acetone. Small drops of $CH_3NH_3H_2PO_2$ were precipitated on the bottom of the flask forming an immiscible biphasic mixture. The washing process by ethanol/acetone mixture was repeated twice. The bottom phase was separated and dried in vacuum at 60 °C for 1 h. At room temperature, $CH_3NH_3H_2PO_2$ is a highly viscous liquid. Methylammonium hypophosphite is highly soluble in polar protic solvents such as methanol, formamide, n-propanol, etc., and easily mixable with polar aprotic solvents such as DMF and DMSO.

Methylammonium phosphite (MAH_2PO_3) was synthesised in a 500 mL flask, 6.3 g of H_3PO_3 were dissolved in 20 mL of water and further mixed with 100 mL of ethanol. Then, 29 mL CH_3NH_2 (40 % in methanol) were slowly added under continuous stirring. After 10 min, solvents were extracted by a rotary evaporator at 60 °C. The highly viscous liquid was diluted with methanol and small white crystals were precipitated by acetone. Purification was repeated twice and the highly crystalline white powder was dried in a vacuum oven at 30 °C for 5 h. Higher temperature or a longer drying time led to partial decomposition of the salt; it changed to a light brown colour due to H_3PO_4 formation.

The dried powder is highly soluble in polar protic solvents such as methanol, formamide, n-propanol, etc., but dissolves very poorly in polar aprotic solvents (N,N-dimethylformamide, dimethyl sulfoxide, acetone, acetonitrile, etc.) with only concentrations of up to 1 mg/mL achieved. However, in the presence of $CH_3NH_3H_2PO_2$, $CH_3NH_3H_2PO_3$ is well soluble in DMF or DMSO.

CH_3NH_2 (40 % in methanol) was purchased from ABCR GmbH & Co KG. H_3PO_2 solution (50 wt % in water), H_3PO_3 (99 %), DMF (anhydrous, 99.8 %), DMSO (99.9 %), ethanol (absolute, 99.8 %), and hydroiodic acid (57 % in water, contains < 1.5 % hypophosphorous acid as stabiliser) were purchased from Sigma-Aldrich. Dimethyl sulfoxide-d6 (DMSO, 99.9 at % D) was purchased from Deutero GmbH.

6.2.5 Nuclear magnetic resonance

Nuclear magnetic resonance (NMR) measurements were performed to characterise the different MAIs and their purity. The different batches of MAI were dissolved in DMSO-d6 for the measurement. A Bruker NEO 400 NMR machine was used for the NMR measurements at 400 MHz. I prepared the solutions and analysed the data while the NMR measurement itself was performed by my collaborator Renée Haver from the Department of Chemistry of the University of Oxford. Levchuk et al. [149] have previously shown that the NH_3 proton NMR peak shifts towards higher values when more MAH_2PO_2 impurity is present, whereas the peak broadens with increasing MAH_2PO_3 impurity concentration. To be able to perform the same analysis, the NMR data was fitted and the FWHM and peak positions extracted. The results are shown in Section 6.3.1.1.

6.3 Results and discussion

To study the influence of impurities on the co-evaporation of methylammonium lead iodide, a high-purity MAI batch was compared with a low-purity MAI batch (for details

of the synthesis see Section 6.2.4). Levchuk et al. [149] previously identified two main impurities in MAI: MAH_2PO_3 and MAH_2PO_2, both are formed during the synthesis of MAI and derive from H_3PO_2. The source of the H_3PO_2 impurity is likely the HI solution used in the synthesis of MAI, since commercial HI is typically stabilised with H_3PO_2. Depending on how the MAI is washed and purified after the synthesis, different concentrations of MAH_2PO_3 and MAH_2PO_2 remain.

6.3.1 Characterisation of precursors

To understand the impact of impurities on the co-evaporation of $MAPbI_3$, it is crucial to know the composition of the precursors and how variable the impurity concentration is for different MAIs. To gain a deeper understanding of the properties of the used precursors, the high-purity and the low-purity MAI as well as commercial MAI batches were characterised.

6.3.1.1 Nuclear magnetic resonance measurements of different batches of MAI

MAI was obtained from several commercial suppliers and characterised using nuclear magnetic resonance (NMR) measurements (see methods section 6.2.5. The same characterisation was performed on the lab-synthesised high-purity and the low-purity MAI supplied by our collaborator Ievgen Levchuk.

All commercial MAI materials were bought in August 2016. Ossilla then sold two different purity grades of which we used that which stated 99.9% purity (order number: M271, no batch number given). Sigma Aldrich gave the purity of their MAI as 98% (order number: 793493-5G, Lot number: MKBW1004V). Solaronix did not state a purity value for the MAI they supplied (order number: 24153, batch number: 17/260916FM). Finally, Dyesol (now Greatcell Solar Materials) also did not state a purity value (order number: 101000,

batch number: 243602) at the time of purchase.

Nuclear magnetic resonance (NMR) measurements were performed to characterise the different MAIs and their purity. The different batches of MAI were dissolved in DMSO-d6 for the measurement. A Bruker NEO 400 NMR machine was used for the NMR measurements at 400 MHz. As Levchuk et al. have described in detail, NMR spectra are a great tool to characterise the presence of impurities in different MAI batches [149]. The data from these measurements are shown in Figures 6.6 and 6.7.

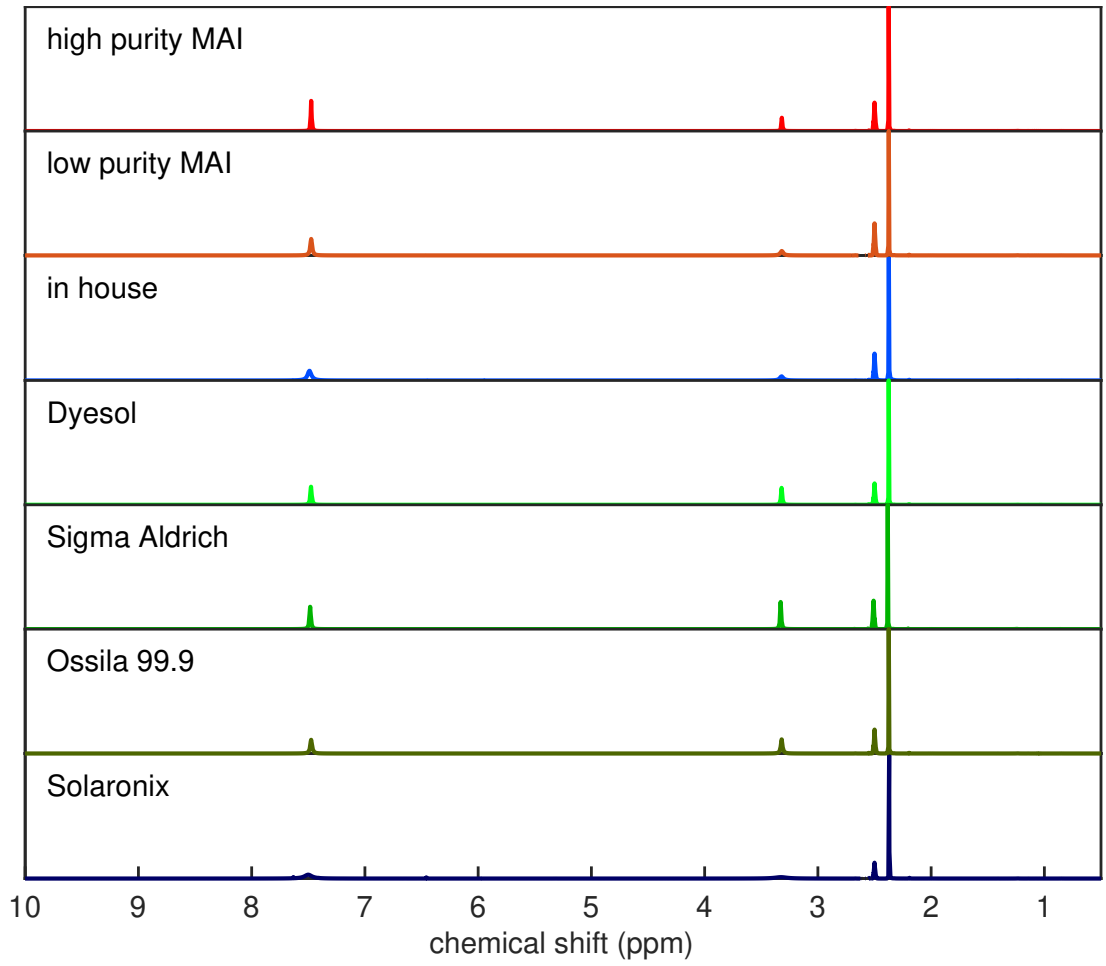


Figure 6.6: Overview of the 1H NMR spectra taken of different batches of MAI. Each MAI sample was dissolved in DMSO-d6 and measured in a Bruker NEO 400 NMR by Renée Haver of the Oxford Department of Chemistry (used with permission from [152]).

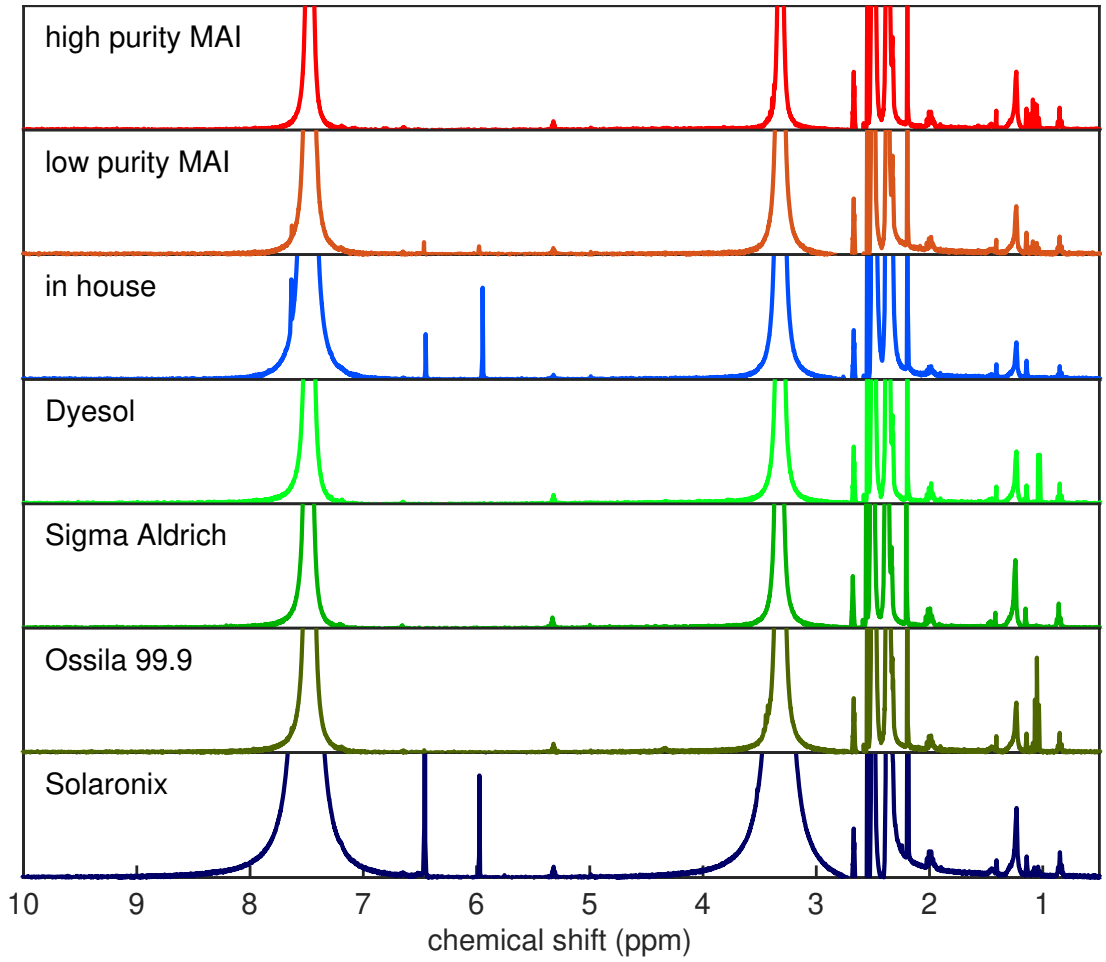


Figure 6.7: A zoom into the 1H NMR spectra of different MAI batches. When zooming into the lower counts, additional small peaks which are associated with impurities are found. NMR spectra were measured by Renee Haver (used with permission from [152]).

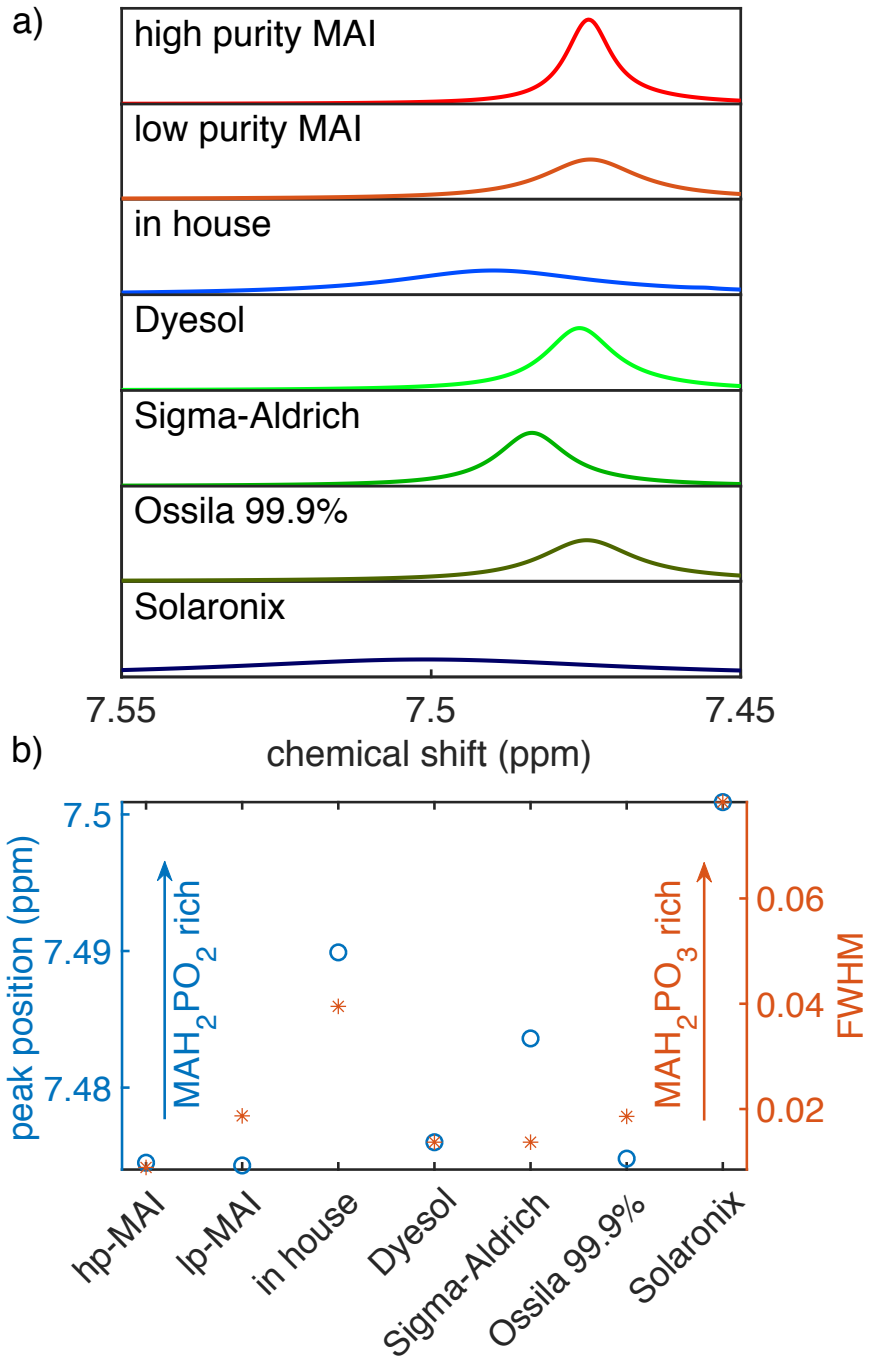


Figure 6.8: 1H NMR characterisation of different MAI batches, measurements were carried out by Renée Haver. a) NMR spectra of different MAI batches shown from 7.55 ppm to 7.45 ppm to focus on the NH_3 proton MA peak. A clear shift of the peak maximum for different batches is observed. b) Summary of the peak position and full width half maximum (FWHM) of the peak around 7.5 ppm for several MAI batches. A higher FWHM indicates that the batch is rich in MAH_2PO_3. A higher peak position indicates that it is rich in MAH_2PO_2 [149] (used with permission from [152]).

Figure 6.8a shows the proton nuclear magnetic resonance (1H NMR) spectra for

samples from each of these batches and a summary of their NH_3 proton peak positions. Their corresponding full width at half maximum (FWHM) is displayed in Figure 6.8b. As shown by Levchuk et al. [149], the NH_3 proton NMR peak shifts towards higher values when more MAH_2PO_2 is present, and the peak broadens with increasing MAH_2PO_3 concentration. We find that our high-purity MAI has the smallest FWHM and peak position of all samples in agreement with Levchuk's observation. Figure 6.8b shows the significant variations in the concentrations of MAH_2PO_2 and MAH_2PO_3 impurities in commercially available MAI. The dependence of the apparent deposition rate on a QMB on the impurity concentration therefore explains the challenges with the control and measurement of the MAI rate during evaporation which have been reported in the literature.

As shown in Figure 6.8, 1H NMR measurements reveal that different commercial batches of MAI contain vastly different amounts of the two studied impurities. While the MAI batch obtained from Dyesol (now Greatcell Solar Materials) contains a small amount of MAH_2PO_3 and of MAH_2PO_2, it is the purest of the commercial samples. The batch from Sigma-Aldrich contains a small amount of MAH_2PO_3 and a significant amount of MAH_2PO_2. In contrast, the MAI batch from Ossila ($> 99.9\%$ purity) is very low in MAH_2PO_2 and contains some MAH_2PO_3. Finally, the batch obtained from Solaronix contains the highest concentration of both of these impurities. In comparison with these commercial samples, our lab-synthesised low-purity MAI sample is still relatively pure.

6.3.1.2 Mass spectroscopy Measurements of MAI and its impurities

To be able to analyse the mass spectra measured during the evaporation, reference data both from the NIST database and from measurements performed using the mass-spectroscopy set-up attached to the evaporation chamber were used. The measured

mass spectrum for the high-purity MAI batch was compared with the mass spectroscopy spectrum for methylamine (MA) from the NIST database (NIST#: 228024) (see Figure 6.9). For masses below 50 AMU/e, the two spectra are very similar. All the main peaks from the methylamine spectrum are reproduced in the methylammonium iodide spectrum that we measured.

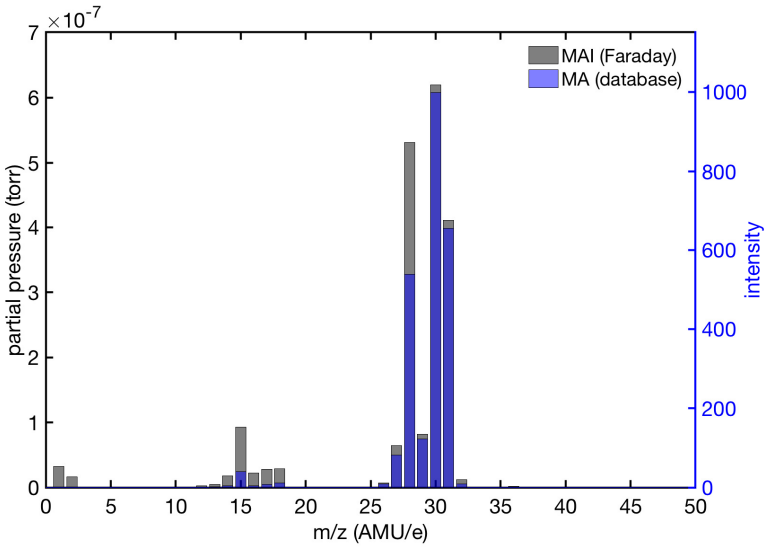


Figure 6.9: Comparison of the mass spectrum of high-purity methylammonium iodide (MAI) (grey) measured with the Faraday detector with the mass spectrum for methylamine (MA) (blue) obtained from the NIST database.The peak positions match well with small deviations in the peak intensities, which are attributed to other constituents in the chamber, such as nitrogen (used with permission from [152]).

Furthermore, isolated impurities were evaporated in the evaporator and the mass spectrum measured. A comparison of the low-purity MAI with the mass spectrum of the isolated impurities is shown in Figure 6.10. Unfortunately, isolated MAH_2PO_2 is liquid at room temperature, and therefore could not be evaporated in our chamber, making it difficult to obtain a reference mass spectrum for this material. When comparing MAH_2PO_3 and MAI, the peaks at 36 and 38 AMU/e are particularly noteworthy since they only show up in the mass spectrum of MAH_2PO_3. In contrast the peaks at 127 and 128 AMU/e are only present in the MAI mass spectrum and are characteristic for iodide (I) and hydrogen iodide (HI).

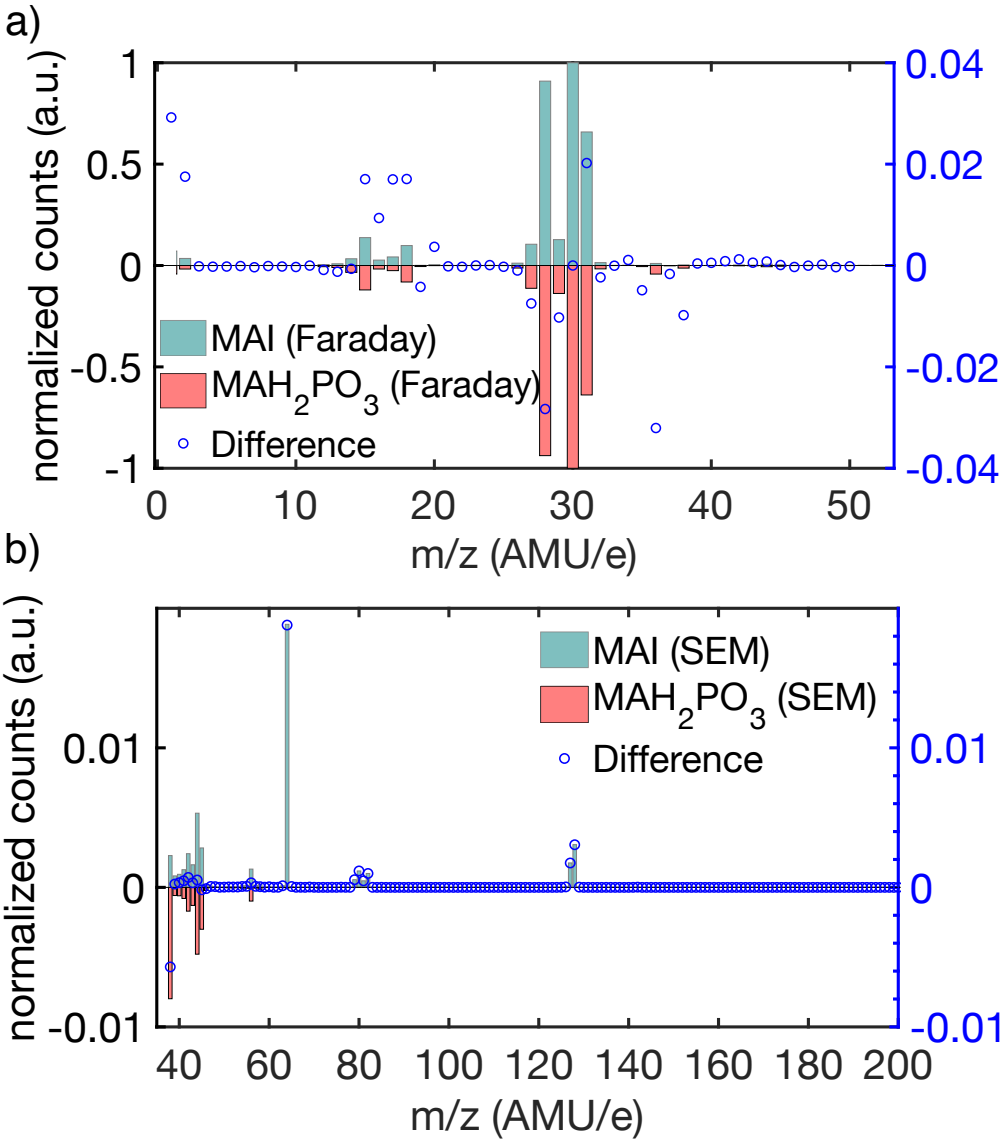


Figure 6.10: a) Comparison of the mass spectrum of MAI and MAH_2PO_3, both recorded with the Faraday detector of the residual gas analysis (RGA) system. b) Comparison of the higher m/z range of the mass spectrum of MAI and MAH_2PO_3, both recorded with the secondary electron multiplier (SEM) detector of the residual gas analysis (RGA) system. The difference between the mass spectra of the two measured substances was calculated by subtracting the normalised MAH_2PO_3 value from the normalised MAI value for each m/z value and is displayed with blue circles (used with permission from [152]).

6.3.1.3 Infra-red spectra of precursors and impurities

To measure the absorption spectrum in the infra-red of the MAI and the isolated impurities MAH_2PO_3 and MAH_2PO_2, as well as H_2PO_3 and H_2PO_2, a Fourier-transform infra-red spectroscopy (FTIR) set-up with an attenuated total reflectance (ATR) extension was

used. The machine used was a Bruker Vertex 80v interferometer with a Bruker Platinum ATR accessory. The attenuated total reflectance technique makes it possible to easily measure the infra-red absorption spectrum of a solid or liquid sample by placing it directly onto the ATR's diamond crystal.

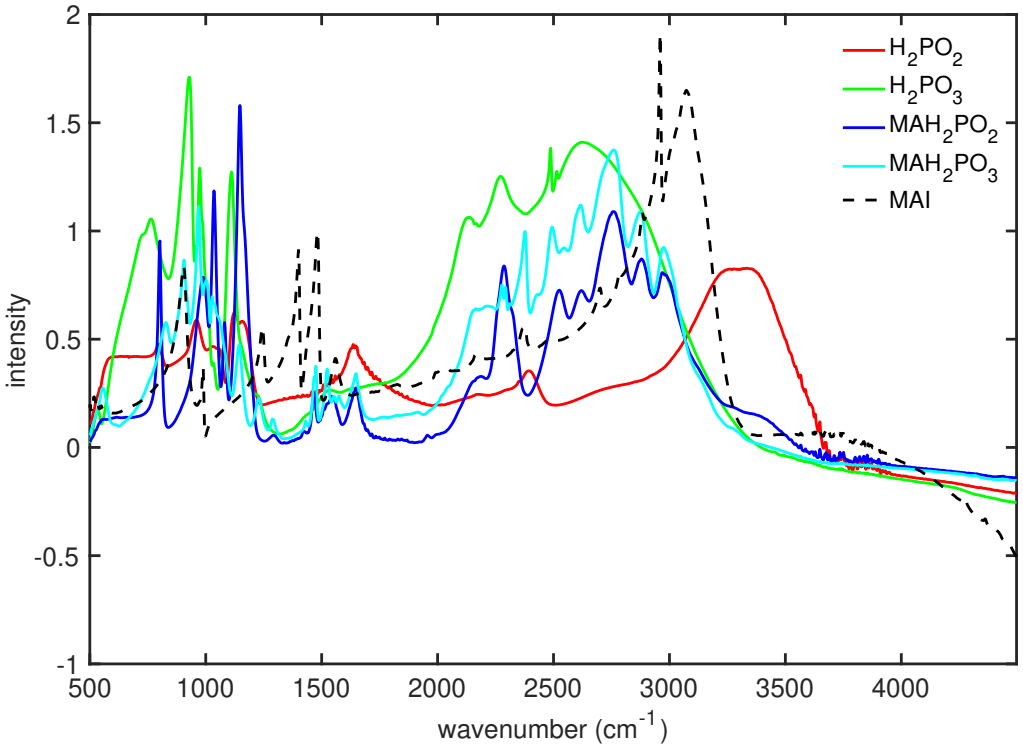


Figure 6.11: ATR-FTIR infra-red absorption spectra of H_2PO_2, H_2PO_3, MAH_2PO_2 and MAH_2PO_3 as well as methylammonium iodide (MAI). Spectra were taken with a Bruker Vertex 80v interferometer combined with a Bruker Platinum ATR accessory (used with permission from [152]).

6.3.2 Evaporation of MAI of different purities

The temperature of the thermal sources and therefore the evaporation and subsequent deposition of the precursors is controlled with proportional–integral–derivative (PID) controllers. These can be set to either maintain a constant rate or to a constant temperature. In this study the PID controlling the MAI was typically set to a constant temperature and the one controlling the PbI_2 source was set to maintain a constant rate on the QMB mounted near that source. The PID values for the PbI_2 source were

carefully tuned to achieve a smooth and constant evaporation of the PbI_2. This process was successful as can be seen in the PbI_2 source temperature curve in Figure 6.12, which is very smooth. In contrast, the PID values for MAI were slightly detuned which led to a small oscillation of the MAI source temperature. This approach was utilized to identify the contributions from MAI in other measurements such as the RGA and QMB measurements.

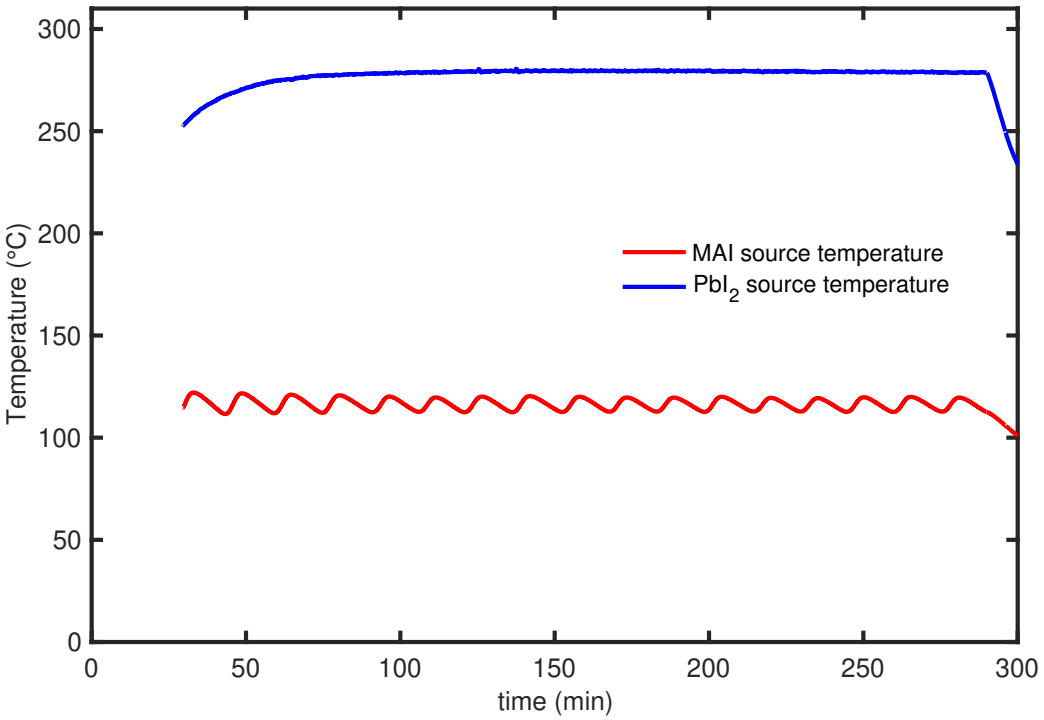


Figure 6.12: Source temperatures of the MAI source (red) and PbI_2 source (blue) over the course of an exemplary co-evaporation run (used with permission from [152]).

6.3.3 Rate-controlled evaporation run with high-purity MAI

It was found that the quartz micro balance (QMB) could not be used to control the deposition run with the high-purity MAI. To demonstrate clearly the problem, a standard evaporation run controlled with the QMB was set-up. The MAI rate was set to a typical value and the PID controller was left to try to regulate the evaporation using the apparent rate the QMB measured. To maintain this apparent rate, the controller continued to increase the temperature until it became well above the normal evaporation

temperature (around 120 °C). It appears that the QMB was not registering enough MAI and therefore the PID controller kept increasing the temperature. The temperature kept rising until eventually the MAI in the crucible ran out. This is apparent in Figure 6.13 after about 55 min when the temperature continues to rise, yet the apparent rate on the QMB drops off completely.

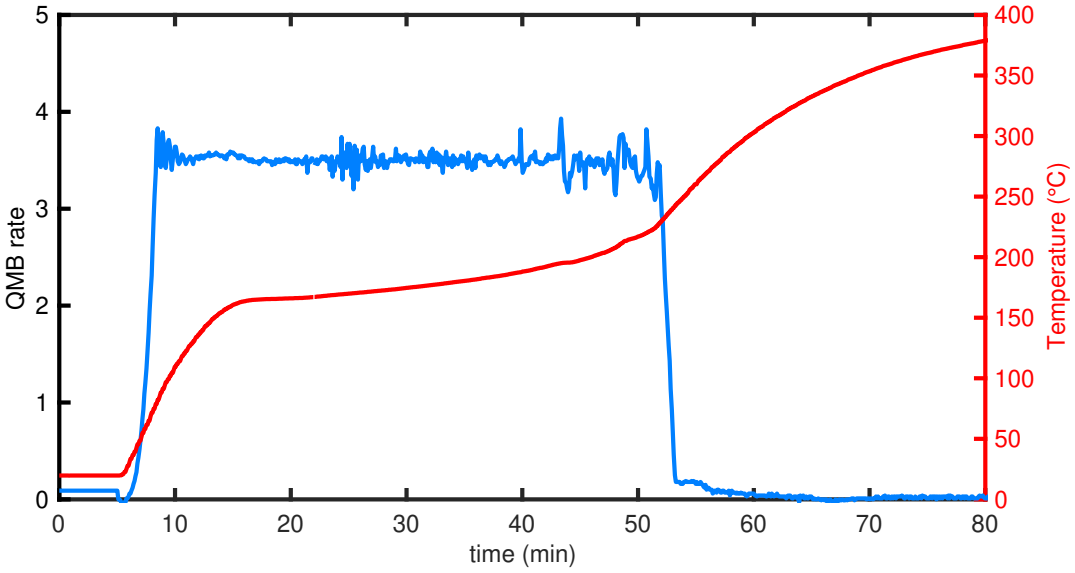


Figure 6.13: A standard rate-controlled evaporation run is set-up with the high-purity MAI as the organic precursor. The development of the temperature and the QMB reading are shown and demonstrate that the rate control is unsuccessful and the MAI runs out during the evaporation (used with permission from [152]).

6.3.4 Co-evaporation of $MAPbI_3$ thin-films

The deposition parameters for both the high-purity and the low-purity MAI batches were optimised separately so that efficient solar cells could be fabricated with either of the batches. It was not possible to use a QMB to monitor the high-purity MAI flux (as discussed in section 6.3.3), therefore optimisation involved repeated co-evaporations of MAI and PbI_2 first varying the temperature setpoints for the MAI source each time and subsequently varying the deposition time. A standard solar cell device architecture consisting of C_{60} and Spiro-OMeTAD as contact layers was used (see 6.2.1 for details). Stabilised efficiencies of 15.7 % for the low-purity batch and 15.3 % for the high-purity

MAI were achieved. The current–voltage (J-V) curves for each of the champion cells are shown in Figure 6.14a and b. For both champion cells the forward (red line) as well as the reverse scan (blue line) are shown and a small amount of hysteresis is found probably related to an imperfect n-contact [100]. While the different purity batches of MAI had different optimal source temperatures and depositions times, it was possible to achieve nearly equal efficiencies using MAI precursors of different purity. This result for vapour deposited devices is in stark contrast to the effect of the impurities MAH_2PO_3 and MAH_2PO_2 on solution processed solar cells. Levchuk et al. [149] reported that during solution processing, these impurities in the MAI can influence $MAPbI_3$ crystallisation, grain size and solar cell performance. They found that solar cells solution processed from less pure MAI actually performed better than those made using highly purified MAI. This contrast highlights the different mechanisms of perovskite crystal formation between vapour and solution based deposition methods and their sensitivity to impurities.

While optimised solar cell performance was similar between vapour deposited devices from different purity MAI, drastic differences were seen between deposition rates of MAI as observed by the QMBs. To gain a better understanding of how the impurities MAH_2PO_3 and MAH_2PO_2 influenced the observed MAI deposition rates, a systematic study was performed in which three QMBs were monitored and the residual gas in the deposition chamber was sampled continuously during an evaporation. The three QMBs were positioned in the chamber so that one was 5 cm above each source (MAI and PbI_2) and one at the same height as the substrate. The temperature of each source was monitored via K-type thermocouples in contact with the bases of crucibles containing the MAI and PbI_2 precursors. Mass spectroscopy was performed continuously via a sampling RGA system connected directly to the deposition chamber at a height intermediate between the deposition sources and sample substrate.

For these depositions the temperature of the source containing MAI was set to a constant target temperature. The proportional-integral-derivative controller (PID) of the MAI source was intentionally detuned so that the measured temperature oscillated around the target value. These oscillations were used to identify the MAI rather than PbI_2 as the source of the iodine signal in the RGA measurements. To achieve this, PID control of the PbI_2 source temperature (based on QMB feedback) was well tuned, with the source temperature remaining constant for the duration of the deposition (as shown in Figure 6.12). Therefore, we could use the temperature oscillations of the MAI source to unambiguously assign the changes seen in the RGA and QMB measurements to the MAI flux.

Firstly, a deposition of a $MAPbI_3$ film was performed using the low-purity MAI batch. Figure 6.14c shows the MAI source temperature (red line) as a function of deposition time with the rate signal from the QMB closest to the MAI source overlaid (blue line). As expected, it can be seen that the small temperature oscillations associated with the detuned PID parameters lead to a large fluctuation of the deposition rate observed on the QMB. The QMB signal could, in this case, have easily been used as a feedback to control the source temperature for steady deposition rates. In contrast, Figure 6.14d shows a repeat deposition in which the low-purity MAI was replaced with high-purity MAI. While the source temperature also oscillates, the apparent rate measured by the QMB for the high-purity MAI was especially low and indistinguishable from the noise floor of the measurement. As such, QMBs clearly cannot be used as part of a control feedback loop when high-purity MAI is deposited. Thus, the QMB behaved quite differently during these two depositions and showed completely different apparent rates for the two different depositions. These results could mean that either there is actually less MAI evaporated when high-purity MAI is used or they could point to a discrepancy between the apparent rate on the QMB and the actual rate of MAI

evaporation. The fact that both of the depositions produced $MAPbI_3$ perovskite films points to a problem with the apparent rate measured by the QMB when purified MAI is being evaporated. This explanation is confirmed by in situ RGA data and analysis of the material deposited on the QMBs, as detailed below.

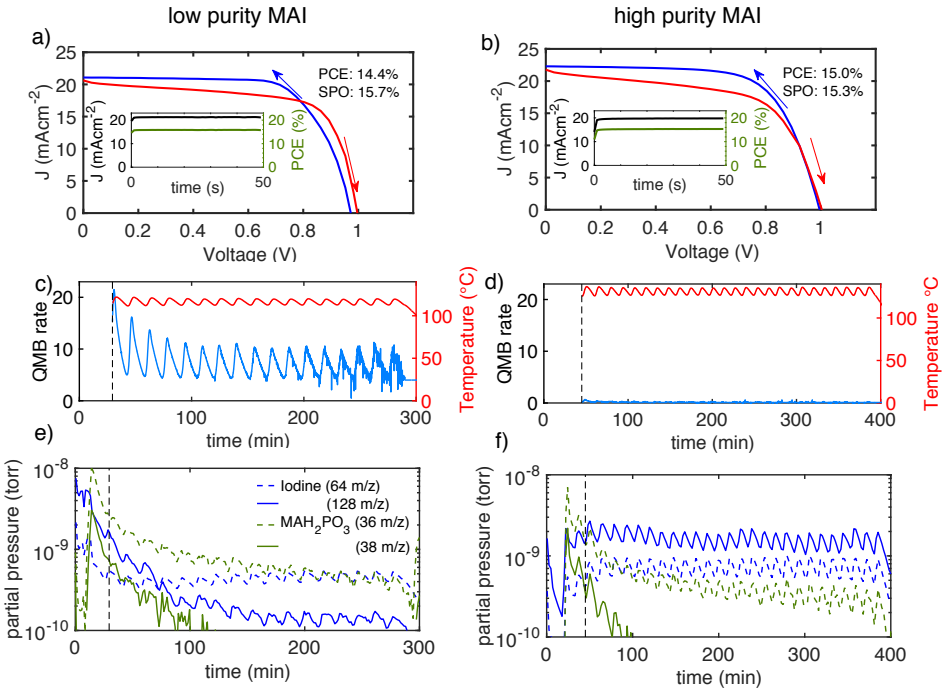


Figure 6.14: J-V-curves of champion $MAPbI_3$ solar cells made using the low-purity MAI (a) or the high-purity MAI (b). For the low-purity MAI, a champion power conversion efficiency (PCE) of 14.4 % and a stabilised power output (SPO) of 15.7 % were measured. For the high-purity MAI the champion PCE was 15.0 % and the SPO was 15.3 %. During the evaporation runs the quartz micro-balance (QMB) rate and MAI source temperature (c,d) were measured. Additionally, a residual gas analysis (RGA) system was used to track selected mass spectroscopy peaks (e,f) over the course of the respective evaporation run (used with permission from [152]).

During the depositions shown in Figures 6.14 c,d the composition of the residual gas in the evaporation chamber was measured using the RGA. The evolution of selected mass spectroscopy peaks over the course of the evaporations is displayed in Figures 6.14 e,f, and selected peaks are identified as originating from iodine (blue) and the impurity MAH_2PO_3 (green) (the assignment of these peaks is discussed in Section 6.3.1.2). For the case of high-purity MAI it is immediately clear from comparison of Figure 6.14 d and f that MAI is indeed being evaporated. The oscillation of the iodine RGA peak,

which correlates with the source temperature, shows that the gaseous iodine originates from the high-purity MAI in the source. Therefore, in support of the argument above, even when the QMB is reading zero, MAI is still being evaporated, hence the problem lies with the QMB not reading correctly when MAI is particularly pure, not the actual MAI flux emitted from the furnace.

X-ray diffraction (XRD) measurements were performed with a Panalytical X'pert powder diffractometer. A standard $\theta - 2\theta$ scan was performed on one $MAPbI_3$ thin-film sample for each MAI batch. A sample from the batch that contained the champion solar cell was used for the XRD for both the low-purity MAI and the high-purity MAI. The two XRDs are very similar. Both show a very small peak around 12.6°, indicating a small amount of PbI_2 in the film. Otherwise, the expected peaks for $MAPbI_3$ are clearly visible in both samples, for example at 14° and 28°.

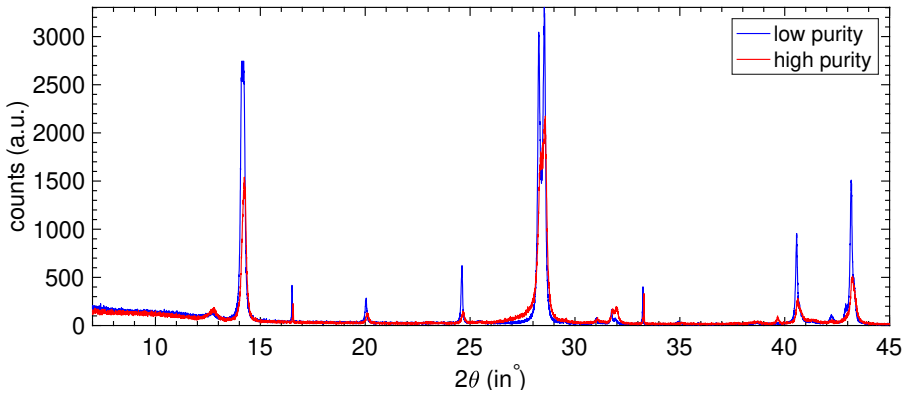


Figure 6.15: XRD spectra measured with a Panalytical X'pert powder diffractometer for samples from $MAPbI_3$ deposition runs performed with low-purity MAI (blue) or high-purity MAI (red) (used with permission from [152]).

Cross-sectional scanning electron microscopy (SEM) images were taken using a FEI Quanta 600 FEG. $MAPbI_3$ thin-films were deposited onto glass which was coated with fluoride-doped tin oxide (FTO). The substrates were then broken in half and mounted vertically to enable recording of SEM images of the cross-section. The perovskite films

from the deposition with the high-purity MAI and from the deposition using low-purity MAI have the same thickness and no noticeable difference in the SEM.

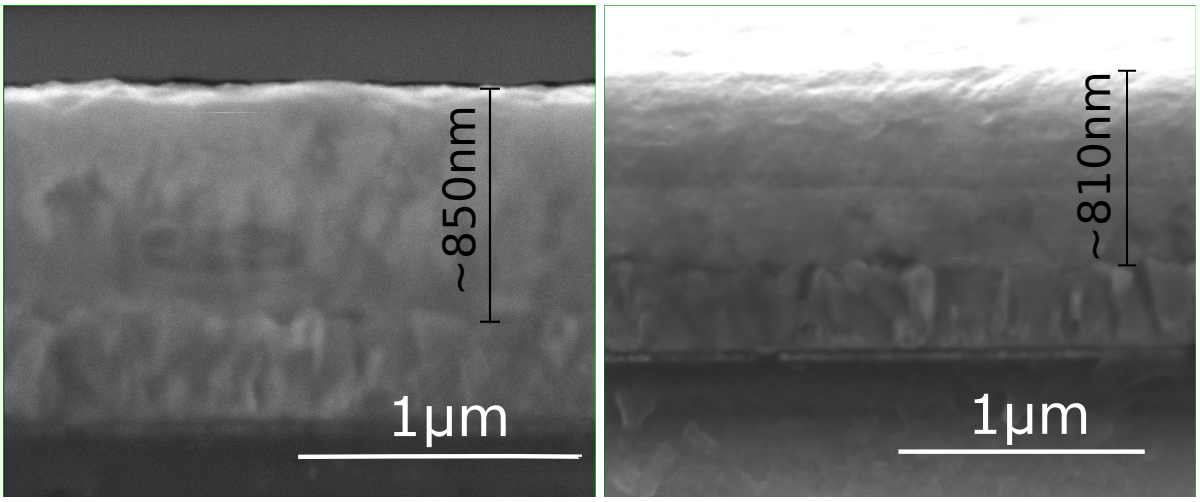


Figure 6.16: Scanning electron micrographs of a $MAPbI_3$ thin-film deposited in the same run as the champion solar cell. The perovskite film on the left (810 nm) was deposited with the low-purity MAI on the one on the right (850 nm) deposited with the high-purity MAI (used with permission from [152]).

6.3.5 Deposits on the quartz micro balances

The results discussed in previous sections do not explain, why the apparent rate of MAI deposition recorded by a QMB is particularly sensitive to small changes in the concentration of impurities in the MAI. During evaporation runs, it was observed that the reading of the quartz balance, which is mounted close to the MAI source, depends dramatically on the batch of MAI that is used (Figure 6.14 c,d). When the low-purity MAI is used, a rate is easily detected. In contrast, when the high-purity MAI is used, the rate is low from the beginning and drops off quickly. The apparent deposition rates recorded by the QMB are vastly different even for runs that result in perovskite films with nearly the same thickness (810 nm and 850 nm respectively, see Figure 6.16). To understand why the QMBs seem to fail in the case of MAI evaporation, the films deposited on the quartz crystals themselves were characterised. After a full co-evaporation run, the QMB crystals were removed from the chamber and scanning electron microscopy

(SEM) and attenuated total reflectance (ATR) infra-red absorption measurements were performed to study any deposits on the QMBs.

Cross-sectional scanning electron micrographs of QMB sensors that monitored MAI deposition rates from low-purity and high-purity MAI are displayed in Figure 6.17a and b respectively. The low-purity MAI has formed a thick MAI layer with grains closely packed (Figure 6.17a) in stark contrast to the high-purity MAI which produced a much thinner layer of platelets on the QMB crystal (Figure 6.17b). To confirm that the material deposited on the QMB in each case was indeed MAI, ATR infrared absorption measurements on each QMB were performed and the resulting spectra are presented in 6.17c.

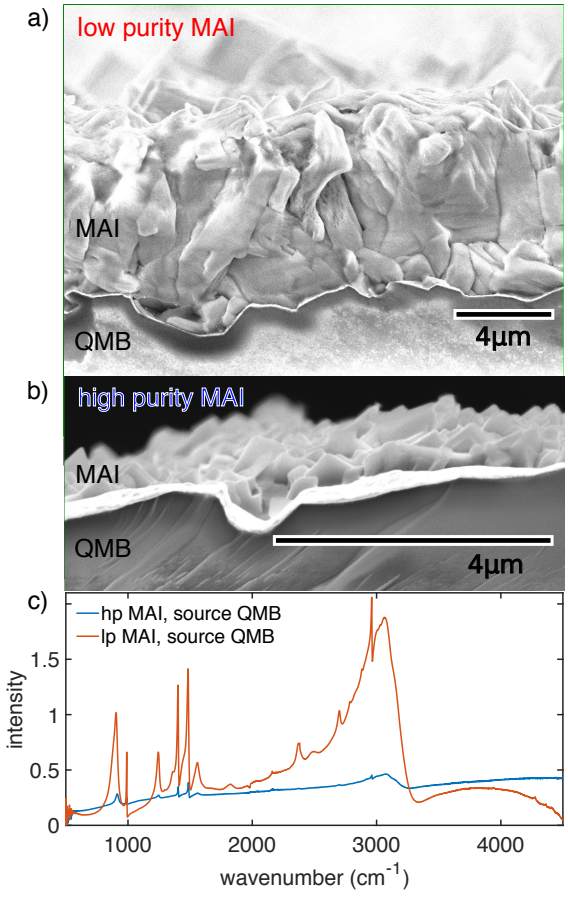


Figure 6.17: Cross-sectional scanning electron microscopy (SEM) images of a quartz balance used to monitor the MAI evaporation during a deposition run with a) low-purity MAI and b) high-purity MAI. c) Infra-red spectrum of those same quartz balances (used with permission from [152]).

The vibrations related to the NH_3^+-bend appear at 2701 cm^{-1}, 1559 cm^{-1} and 1414 cm^{-1} while the vibrations relating to the $NH_3CH_3^+$-rock occur at 1244 cm^{-1}, and 905 cm^{-1} [138]. The ATR signal from the QMB sensor used during the high-purity MAI deposition is much weaker than that from the low-purity MAI. However, both do show the expected peaks for MAI, indicating that a film of MAI is present in both cases, albeit of considerably different thickness. Thus, it appears that in both cases MAI is deposited onto the source monitor crystal, but much less material adheres to the crystal when high-purity MAI is used compared to when low-purity MAI is used, even when the same thickness of $MAPbI_3$ is grown on the substrate.

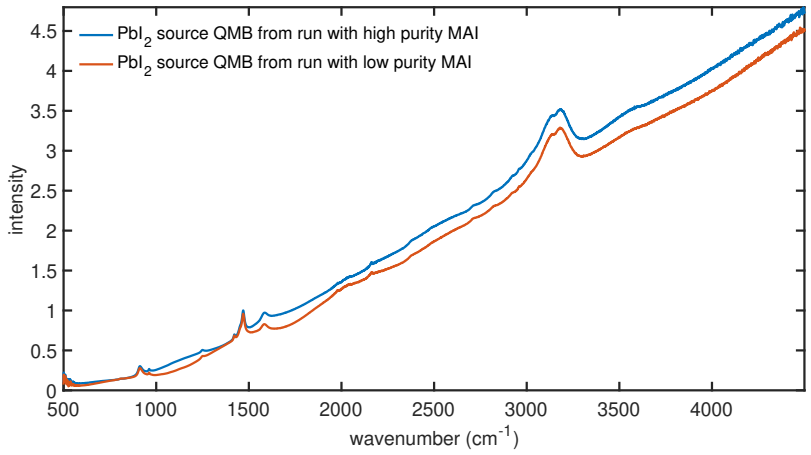


Figure 6.18: ATR infra-red absorption spectra of the QMB placed close to the PbI_2 source during co-evaporation with high-purity MAI (blue), and low-purity MAI (red) (used with permission from [152]).

The infra-red absorption spectra of the material deposited onto the QMBs which were mounted close to the PbI_2 source are nearly identical (Figure6.18). The small difference in intensity can be explained by small differences of how firmly the QMB is pressed against the ATR crystal. This strong similarity is expected, as the QMB monitors at the PbI_2 source are only meant to detect the PbI_2 and not the MAI. Therefore, a change in MAI batch should not influence the deposition on this QMB crystal.

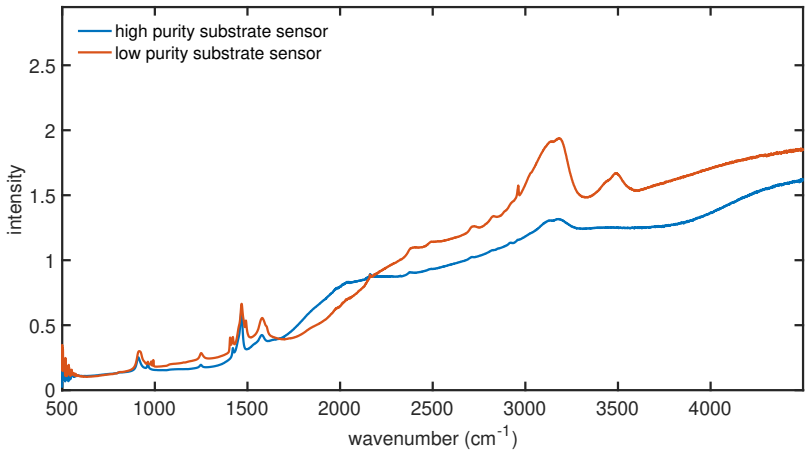


Figure 6.19: ATR infra-red absorption spectra of the QMB placed close to the substrate during co-evaporation with high-purity MAI (blue), and low-purity MAI (red) (used with permission from [152]).

Similar to the spectra of the QMBs next to the PbI_2, the infra-red spectra of the QMB monitors mounted next to the substrate, are not influenced by which batch of MAI is used (see Figure 6.19). The large differences between high and low-purity MAI seen in the SEM images and IR spectrum of the source QMB (Figure 6.17) are consistent with the difference in the detected MAI rate during the evaporation run displayed in Figure 6.14 c,d. In both evaporation runs, nearly the same thickness of $MAPbI_3$ was grown on the substrate (see Figure 6.16). Evidently, enough MAI was deposited to achieve the desired composition as only very small lead iodide peaks appear in the XRD of the grown $MAPbI_3$ films (see Figure 6.15). But from the apparent rate measured by the QMB at the MAI source, one could incorrectly conclude that much less MAI was present during the evaporation with the high-purity MAI than during the run using low-purity MAI. Together, these measurements indicate that the sticking coefficient of pure MAI to the gold surface of the QMB is vanishingly small, however in the presence of the impurities MAH_2PO_3 and MAH_2PO_2, MAI adheres significantly better to the gold surface. A possible mechanism for this could be that the impurities form small clusters on the

gold surface which then act as nucleation centres for MAI growth. A more detailed study would be required to test this hypothesis.

6.4 Conclusion and outlook

To study the processes occurring within the vacuum chamber during the co-evaporation of $MAPbI_3$ and the influence of impurities, MAI batches with two different purities were used. Thin-film depositions were performed with these MAI batches and the evaporations were monitored using quartz microbalances, a residual gas analysis system as well as pressure and temperature sensors. Subsequently, the resulting films and solar cells were synthesised. It was found that the sticking coefficient of MAI to the gold surface of a quartz microbalance is highly sensitive to the concentration of impurities in the MAI. Thus, for the same MAI flux, the thickness of the MAI film deposited onto the balance varies greatly depending on which batch is used. This explains why some groups report great difficulty with the QMB-based control of MAI deposition flux, while others are able to control the MAI rate with quartz balances.

The presence of MAH_2PO_3 and MAH_2PO_2 increases the sticking coefficient of MAI to the QMB and allows deposition rate feedback control. This suggests that controlled concentrations of these impurities in the MAI precursor could allow reproducible QMB controlled depositions. However it was found that the concentration of the MAH_2PO_3 impurity varies during an evaporation, as can be seen in Figure 6.14 e,f. This suggests that the impurities preferentially out-gas from the precursor at the beginning of the deposition which is likely to lead to changes of the sticking coefficient of MAI to the QMB during an evaporation run. Hence, it is expected that the apparent MAI deposition rate as measured by a QMB will vary from the true rate over the course of a co-deposition.

Therefore, QMBs on their own are not an especially reliable way to monitor the MAI evaporation. Thus, additional monitoring methods should be used, for example residual gas analysis or in situ XRD [110]. Residual gas analysis can additionally be useful to monitor deposition rates, detect possible water or halide contamination, and to check for vacuum leaks. The change in the concentration of impurities in the residual gas over the course of the deposition (see Figure 6.14 e,f) also complicates QMB based rate control even when sufficient MAI does stick to the QMB.

In spite of the difficulties in controlling MAI deposition rates it was possible to optimise $MAPbI_3$ co-deposition for a batch of high-purity and a batch of low-purity MAI. The resulting solar cell devices had a similar performance, indicating that the impurities MAH_2PO_3 and MAH_2PO_2 have little effect on the function of co-evaporated $MAPbI_3$. These results are very promising as they show that the full potential of vapour deposited solar cells has not been reached yet, owing to a lack of reliable process control. Once accurate rate control of all precursors is achieved, rapid growth optimisation will be achieved, which should lead to significant improvement in the performance and reproducibility of vapour deposited metal halide solar cells. Overall, the understanding gained in this study of the source of growth irreproducibility and developing better deposition control methods will enable vapour co-deposition to become the method of choice for up-scaling solar cell production to an industrial scale.

7

Patterned Perovskite Thin-films for Transparent Solar Cells and Lasing

7.1 Introduction and motivation

Excellent solar cell materials that approach the Shockley–Queisser limit of power conversion efficiency also need to be good materials for light emission and vice-versa [158]. Therefore metal halide perovskite materials should not only be useful for solar cells, but also for light emitting devices (LEDs) and lasers. A large number of different perovskite based LEDs have been demonstrated with emission wavelengths from blue, green and red to infra-red [159] and first steps towards commercialisation of perovskite LEDs are being made [160]. The progress towards electrically driven perovskite lasers has not been as rapid, but several approaches for optically driven lasing have been implemented [45]. A variety of feedback architectures has been used to achieve lasing action in perovskites, namely random lasing facilitated by scattering on grain boundaries [161], Fabry-Pérot resonance between the boundaries of a perovskite thin-film [162], the end facets of a nanowire [163], a distributed feedback provided by a grating at the back of the perovskite film [164], or whispering gallery mode lasing [165]. But so far, all of these approaches have been optically driven, not electrically driven.

A particularly popular feedback architecture for perovskite lasers are whispering gallery mode lasers. Whispering-gallery wave modes (WGM) are modes that travel along the surface of a concave structure. They were first described in sound waves by Baron Rayleigh who observed them in the gallery at the base of the dome of St. Paul's Cathedral, London [166]. He described such wave modes as the sound clinging to the concave wall. His initial proposals of a theory to describe whispering gallery wave modes were refined by Chandrasekhara Venkata Raman who not only refined the theory and conducted experiments in St.Paul's, but also conducted lab experiments to show the same effect in light waves [167]. Both already speculated that such wave modes could also play a role in the propagation of seismic waves around the surface of the earth. More recently, such modes have been exploited in micro-disk semiconductor lasers and have now also been deployed to fabricate perovskite lasers [168–170]. To fabricate a perovskite WGM laser, a small disk or sphere of perovskite is necessary. Most WGM based perovskite lasers, reported in the literature, use nanoplatelets randomly grown in solution [171–173]. This approach limits the control over the used size and shape. Consequently, most of these do not use circular disks, but less advantageous square or hexagonal perovskite platelets. Being able to grow controlled perovskite disks would be an enormous advantage which would not only make it possible to use the best shapes for lasing, but would also make it easier to place them accurately and integrate them with contacts to fabricate electrically driven perovskite micro-disk lasers.

Another application of non-continuous perovskite films are semi-transparent solar cells. They are attractive for use in building-integrated solar panels, for example in glass façades or windows. Their use would open up previously unusable surfaces for solar energy generation. In their deployment, there is an obvious trade-off between absorbing light to generate electricity and transmission of light through the window to illuminate the space

behind it. Therefore the power conversion efficiency and the average visible transmittance (AVT) are important properties of a semi-transparent solar cell. Furthermore, it is usually desired to have a neutral coloured solar cell as to not distort the colours viewed through the window. With perovskites, this has been realised with two different approaches. Either very thin perovskite films [174] are used which still transmit a large fraction of the light or discontinuous perovskite films are employed [175] in which the light is transmitted in the areas not covered by perovskite. These discontinuous films have typically been fabricated by encouraging an island growth rather than continuous film growth in a solution deposition process. This leads to irregularly shaped perovskite islands and a hard to control deposition where properties such as overall coverage, island shape and height and position are hard to control. Only rarely have more precise patterning techniques been employed for perovskites. One attractive method would be photolithography but this is challenging to combine with a solution processed perovskite film. The solvents used to deposit the perovskite would attack the underlying photoresist, rendering standard photolithography approaches impossible. A few workarounds have been reported in the literature including a wettability-assisted photo-lithography (WAP) process which relies on patterning a polymer layer which the perovskite solution does not wet well and instead only wets the exposed substrate beneath [176]. This reliance on wettability limits which contact layers can be used. In contrast, a co-evaporation based approach eliminates any problems related to interaction of photoresist and perovskite solvent as no solvent is used.

The aim of this chapter is to demonstrate that it is possible to pattern co-evaporated perovskite films using both photolithography and ion-milling. Numerical modelling was used in collaboration with Dr Sudha Mokkapati of Monash University to determine suitable disk sizes. She numerically solved the three-dimensional Maxwell Equations for this system using the software package Lumerical to determine that disks and

rings with diameters below 10 μm would be able to support whispering gallery modes. Patterns suitable for whispering gallery lasing were fabricated and their absorption and luminescence properties were studied.

7.2 Methods

7.2.1 Photolithographic patterning

To fabricate photolithographically patterned perovskite disks, an image reversal photoresist was used with an inverted mask. Glass coated with fluoride doped tin oxide (FTO) was used as the substrate. The substrates were meticulously cleaned using a multi-step process. First, the substrates were ultra-sonicated in a succession of different baths. The first contained a soapy solution of the liquid detergent Decon 90, followed by a bath of deionised water, an isopropanol (IPA) bath and an acetone bath. Next, the substrates were cleaned for ten minutes with an oxygen plasma and finally ultra-sonicated for another 5 min in acetone and rinsed in IPA. The clean substrates were then placed in a spincoater and the image reversal photoresist AZ 5214E was spin-coated on-top of the substrate. To uniformly spread out the resist, a slow pre spin of 10 s at 500 rpm was used followed by a faster spin of 45 s at 5000 rpm. The resist was then dried on a hotplate at 110 °C for 50 s.

An EVG620 mask aligner was used to expose the resist to ultraviolet light. A 5 inch chrome on glass mask and a UV dose of 33 mJ/cm^2 was used. The sample was then baked at 120 °C for 120 s to reverse the image reversal resist. Then a flood exposure was used and the sample exposed to a UV dose of 250 mJ/cm^2. Finally, the resist was developed using the AZ726 MIF developer. To do this, the sample was placed on a bath of the developer for 60 s and then rinsed in deionised water. The developer dissolves the photoresist exposing the underlying FTO, except in those regions which were exposed during the initial UV exposure where the photoresist remains. The remaining photoresist

has an undercut which facilitates the later lift-off of the evaporated perovskite film. To achieve the desired features, all of these steps need to be optimised and executed with exactly the right settings and timings. If this is not the case, the pattern in the resist will be distorted or not be sufficiently deep to reach the FTO which is crucial for the following steps. Examples of such unsuccessful photolithographies are shown in Figure 7.1.

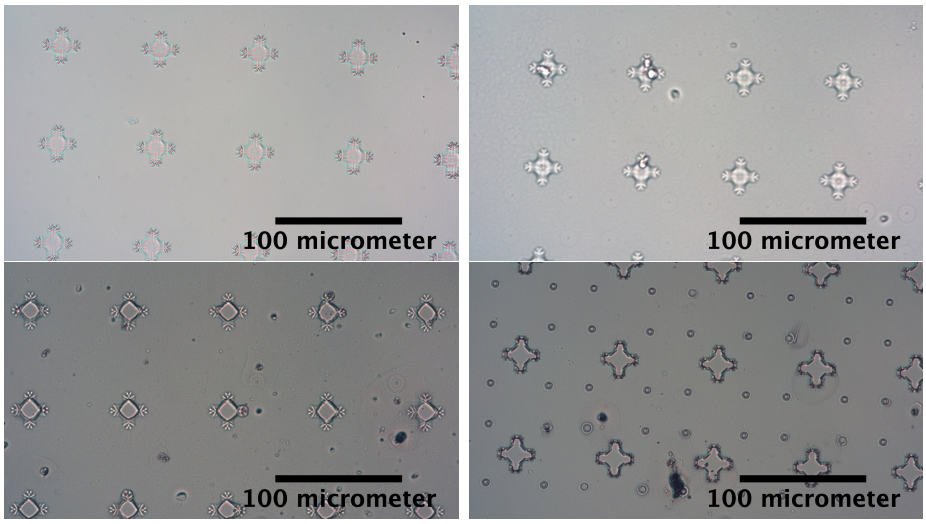


Figure 7.1: Examples of optical microscopy images of patterned photoresist from different photolithography runs. The shown reference marks should be crosses but are distorted due to different issues in the resist deposition, exposure and development.

Once a layer of photoresist with the desired pattern has been fabricated, the $FAPbI_3$ perovskite layer is evaporated on-top as described in Section 5.2.1. The perovskite fills in the holes where the photoresist has been removed but also covers the remaining photoresist. Those areas which have both photoresist and perovskite need to be removed. This lift-off is achieved by briefly (30-40 s) ultra-sonicating the sample in IPA which removes the photoresist and the perovskite on top of it, leaving only the perovskite disks behind.

7.2.2 Ion-milling of perovskite thin-films

Ion-milling was carried out in collaboration with Dr Li (Lily) Li at the ACT Node of the Australian National Fabrication Facility at the Australian National University (ANFF @ ANU). The features were milled with a FEI Helios 600 NanoLab focused ion beam set-up.

Ion-milling is a physical etching method which is frequently used to prepare thin lamella for cross-sectional transmission electron microscopy measurements. For this study, the technique was used to make small perovskite disks and rings. A $FAPbI_3$ thin-film was deposited on FTO coated glass in Oxford. The samples were then vacuum sealed and shipped to the Australian National University where Dr Li (Lily) Li partially milled away the perovskite to fabricate small disks and rings. The results are shown and discussed in Section 7.3.2. After the ion-milling, the samples were again vacuum packed and then shipped back to Oxford where they were characterised.

7.2.3 Photoluminescence microscopy

To study the photoluminescence (PL) of the fabricated features, it is necessary to be able to excite only the patterned feature and not the surrounding area. For this, a custom built photoluminescence microscope was used. The excitation laser was focused onto the sample with the same objective which is used to collect the photoluminescence from the sample. The whole microscope was mounted on a three-axis motorised stage to be able to move it with respect to the sample. The sample was mounted on a separate sample stage and illuminated with a back light. An armoured single mode optical fibre is pigtailed to the laser and transports the excitation light to the microscope where it is focused on the sample with a 50x objective with a large working distance. The photoluminescence is collected with the same objective and fed into a multimode optical fibre which carries it to the spectrometer where it is recorded. The spectrometer is a Horiba iH320 spectrometer combined with a nitrogen-cooled Si CCD detector. A camera is used to record the image from the microscope to allow for positioning and focusing of the sample prior to the photoluminescence measurement. It is protected with a filter during the photoluminescence measurement to avoid damage from the excitation laser. Similarly, a long pass filter is placed in-front of the entrance to the spectrometer to

avoid scattering of laser light into the spectrometer and 2nd order signals. During the PL measurement, the lamp used to back light the sample is also removed to avoid any influence from it.

To determine the spot size of the laser excitation spot in the photoluminescence microscope, a razor blade was attached to a power meter and the laser was moved across it. In order for this approach to yield an accurate result, the focus of the laser needs to be at the location of the razor blade. The focus of the laser and the focus of the PL microscope are well aligned to each other. Therefore, if the image of the razor blade is in focus, the focus of the laser is on the razor blade. After the razor blade was brought into focus, the motorised stages were used to move the laser stepwise across the edge of the razor and the laser power was measured at each step. The results of this measurement are shown in Figure 7.2. The full width at half maximum of the beam was determined to be 8.86 μm.

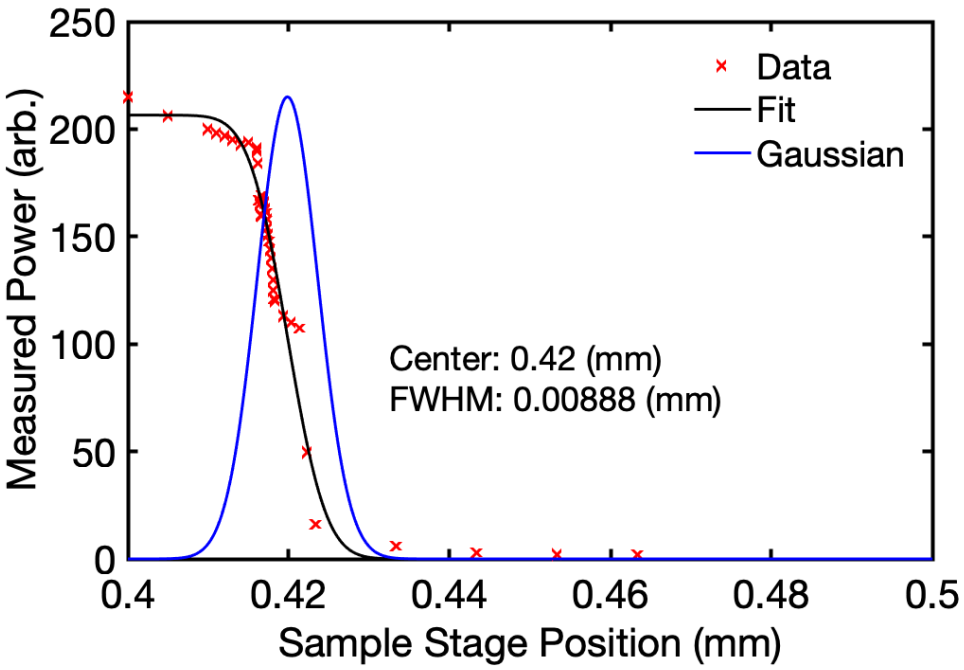


Figure 7.2: Beamwidth measurement to determine the size of the laser spot in the photoluminescence microscope. The measured data was fit with an Error function and the derivative of that is the shown Gauss function with a FWHM of 8.86 μm.

7.3 Results and discussion

Two different sets of patterned samples were fabricated. On the one hand, photolithographically patterned films, on the other hand ion-milled patterns. Using photolithography a whole area can be covered with the same pattern, whereas ion-milling gives individual features. Since these two sets of samples are quite different the results obtained from them are presented in separate sections.

7.3.1 Photolithographically patterned films

Films were patterned using image reversal photolithography as described in Section 7.2. Two different patterns were achieved, one with disks with a targeted size of 20 μm and one with disks with a targeted size of 10 μm. Once the photoresist was deposited, exposed and developed, a $FAPbI_3$ perovskite layers was deposited on top, as described in Section 5.2.1. This resulted in a sample with photoresist and perovskite on it, as shown in the image on the left in 7.3. Then the photoresist was lifted off to obtain a sample with only perovskite disks on it. This lift-off was performed by ultra-sonicating the sample in IPA for 30 s. IPA is known to dissolve the organic molecule used in the perovskite film [77, 177], there was therefore a concern that the IPA batch would dissolve some of the formamidinium in the film and damage the film. To avoid this, the lift-off was performed as quickly as possible with only a very brief IPA bath. Moreover, half of the samples were not lifted-off with neat IPA but with a solution of 10 mg/ml formamidinium iodide (FAI) in IPA to test if this would help avoid a degradation of the perovskite during lift-off.

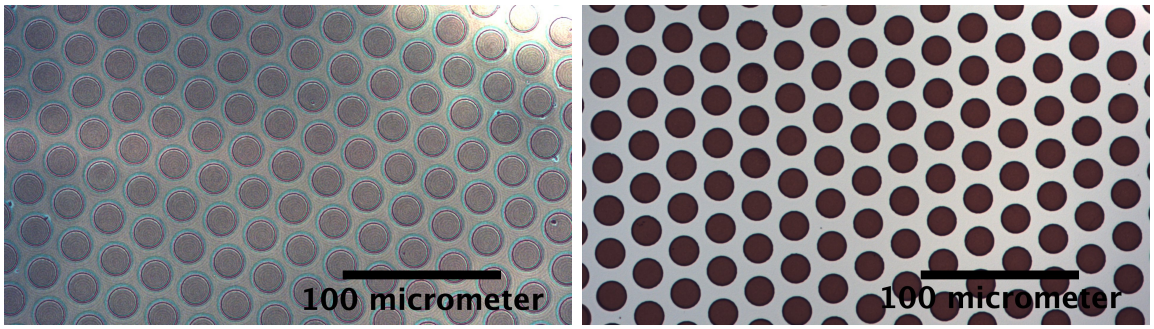


Figure 7.3: Optical microscopy images of photolithographically patterned $FAPbI_3$, on the left before lift-off together with the photoresist, and on the right, after lift-off with only the $FAPbI_3$ disks remaining.

Both the lift-off with neat IPA and the lift-off with IPA and added FAI were successful. The photoresist was removed and perovskite disks remained. When the lift-off was performed with a solution of FAI in IPA, the resultant samples had a less uniform appearance under the microscope with lighter spots on the perovskite disks (see Figures 7.4, 7.5). These may be excess FAI deposits, but further analysis would be necessary to confirm this. If they are FAI deposits, a reduction of the FAI concentration in the solution used for lift-off would be advisable.

The actual disk size was slightly smaller both for the pattern with targeted disk size of 20 μm and the pattern with a targeted size of 10 μm. The larger disks had a diameter of 18 μm (see Figure 7.4) and the smaller disks had a diameter of 9 μm (see Figure 7.5). Additional cross-sectional scanning electron microscopy (SEM) reveals that the edges of the disks are sloped (see Figure 7.11). This is consistent with the aforementioned undercut of the photoresist (compare Section 7.2).

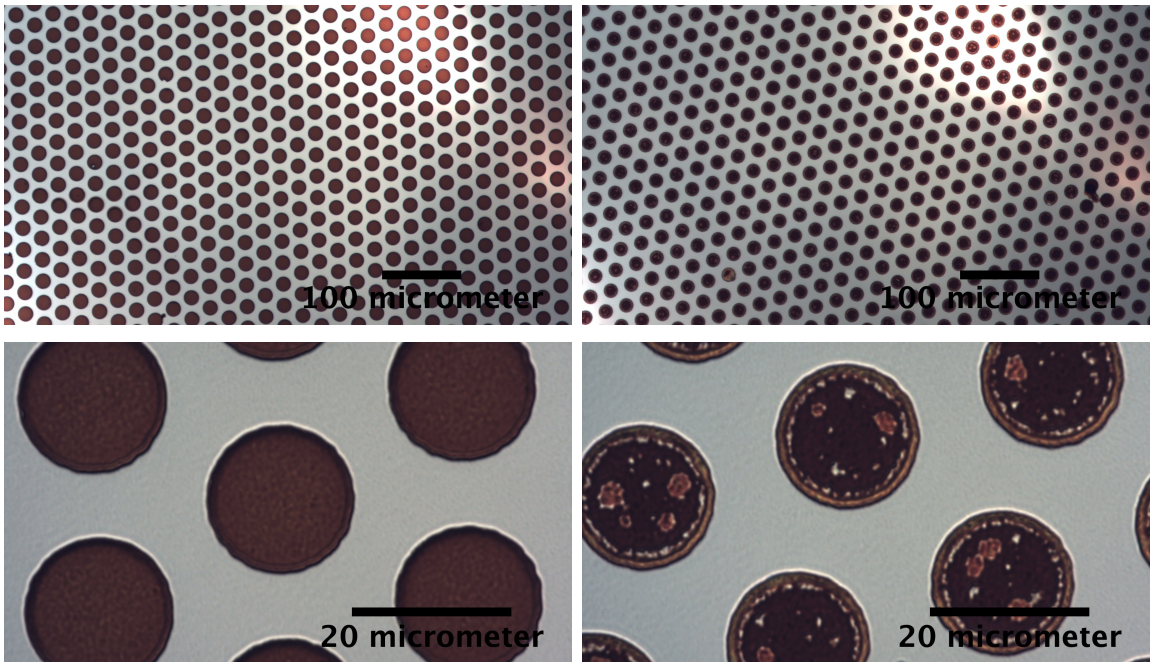


Figure 7.4: Photolithographically patterned $FAPbI_3$ disks with 18 μm diameter. On the left, samples for which lift-off was performed with neat IPA, on the right, samples where lift-off was performed with IPA with added FAI.

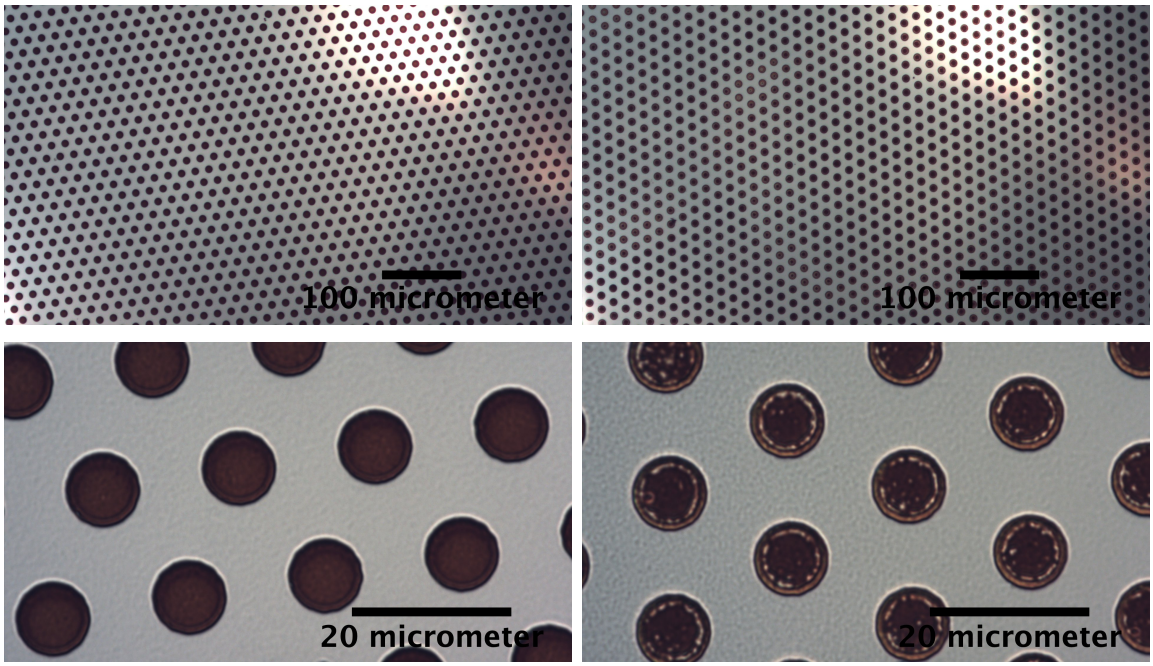


Figure 7.5: Photolithographically patterned $FAPbI_3$ disks with 9 μm diameter. On the left, samples for which lift-off was performed with neat IPA, on the right, samples where lift-off was performed with IPA with added FAI.

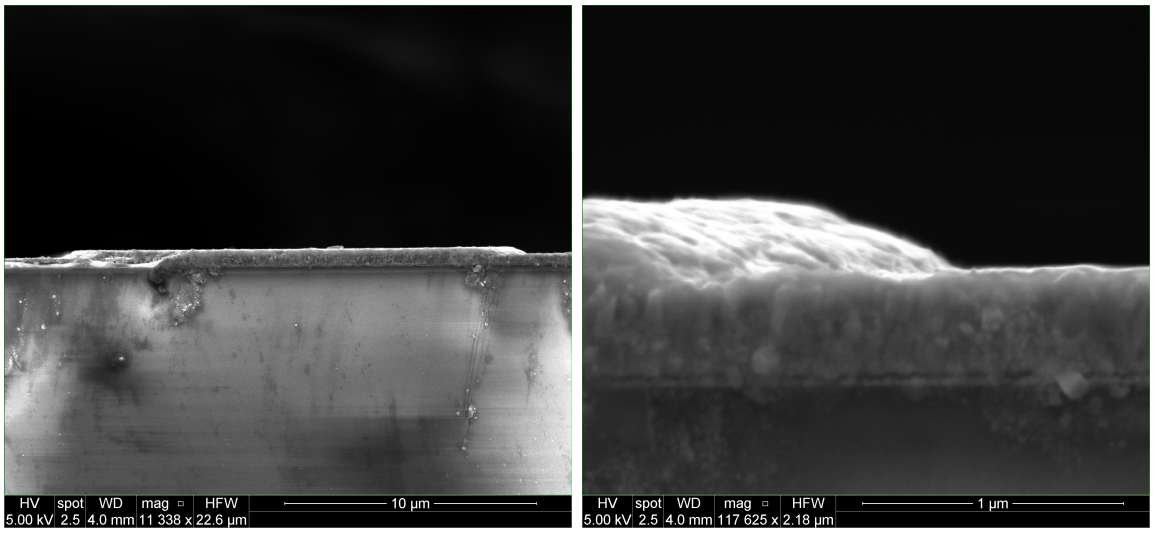


Figure 7.6: Cross-sectional scanning electron microscopy images of the 18 μm disks, recorded by Dr Mathias Uller Rothmann.

To assess the optical properties of these photolithographically patterned films, transmission and reflection were measured using a FTIR set up and the absorption calculated from these data (Figure 7.7). All of the films show an absorption onset around 1.6 eV in line with the expected onset for $FAPbI_3$. For energies above the bandgap, the 18 μm disks (samples B1 and B2) absorb more than the 9 μm disks (samples D1, D2). Both absorb significantly less in this region than the plain $FAPbI_3$ film. This shows that the patterned films are semi-transparent which could be utilised in the fabrication of semi-transparent solar cells. In the energy region below the bandgap, the absorption of the solid film drops off rapidly and it becomes nearly transparent which is in line with previous absorption spectra measured on $FAPbI_3$ films and presented in Figure 5.8. In contrast, the absorption of the patterned films appears to stay high even for energies below the bandgap. This is not due to actual absorption but is caused by scattering in this energy region. Scattered light is not captured by the detector and therefore neither measured in the transmission nor in the reflection measurement which falsely leads to the appearance of an elevated absorption in this region. This could be avoided by doing the measurements with an integrating sphere which would not only collect the directly

transmitted or reflected light, but also the scattered light.

In conclusion, the absorption spectra show that all of the films do have an absorption spectrum consistent with $FAPbI_3$ and the patterned films are semi-transparent for energies above the bandgap and scatter strongly below the bandgap.

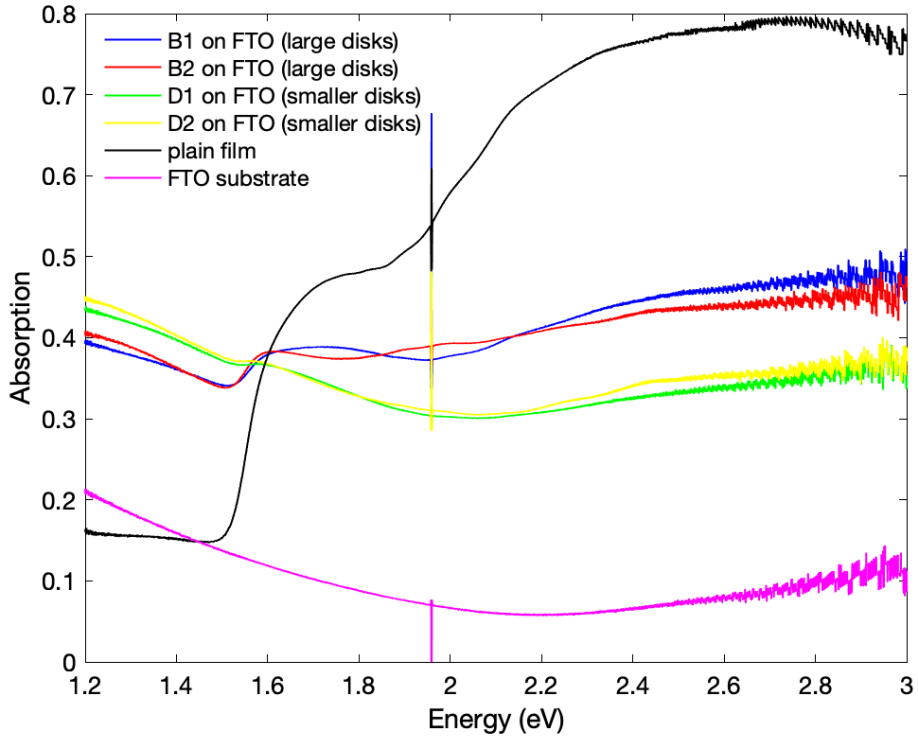


Figure 7.7: Absorption spectra of patterned $FAPbI_3$ films with two different patterns (larger and smaller disks) and a plain $FAPbI_3$ film (black line) as well as a bare FTO substrate for comparison.

After establishing that the absorption of the patterned films was as expected, the photoluminescent properties were studied to see if these patterns were emissive, a crucial first step towards amplified spontaneous emission (ASE) and lasing. The earlier described photoluminescence microscope (see section 7.2) was used to study the patterns further. Using the positioning camera and the sample stages, the sample was positioned so that the laser spot was either directly on the disk, or off the disk. In both positions, the photoluminescence (PL) spectrum was recorded. As shown in Figure 7.8, a clear

photoluminescence is measured when the laser is on the disk whereas no photoluminescence is measured when the laser is off the disk. This demonstrates that the perovskite was not degraded significantly during the fabrication and is still emissive. Furthermore, it shows that the disks are well separated and no perovskite remains between them. Additionally, it indicates that the laser is quite focused and indeed only excites a small area of the sample.

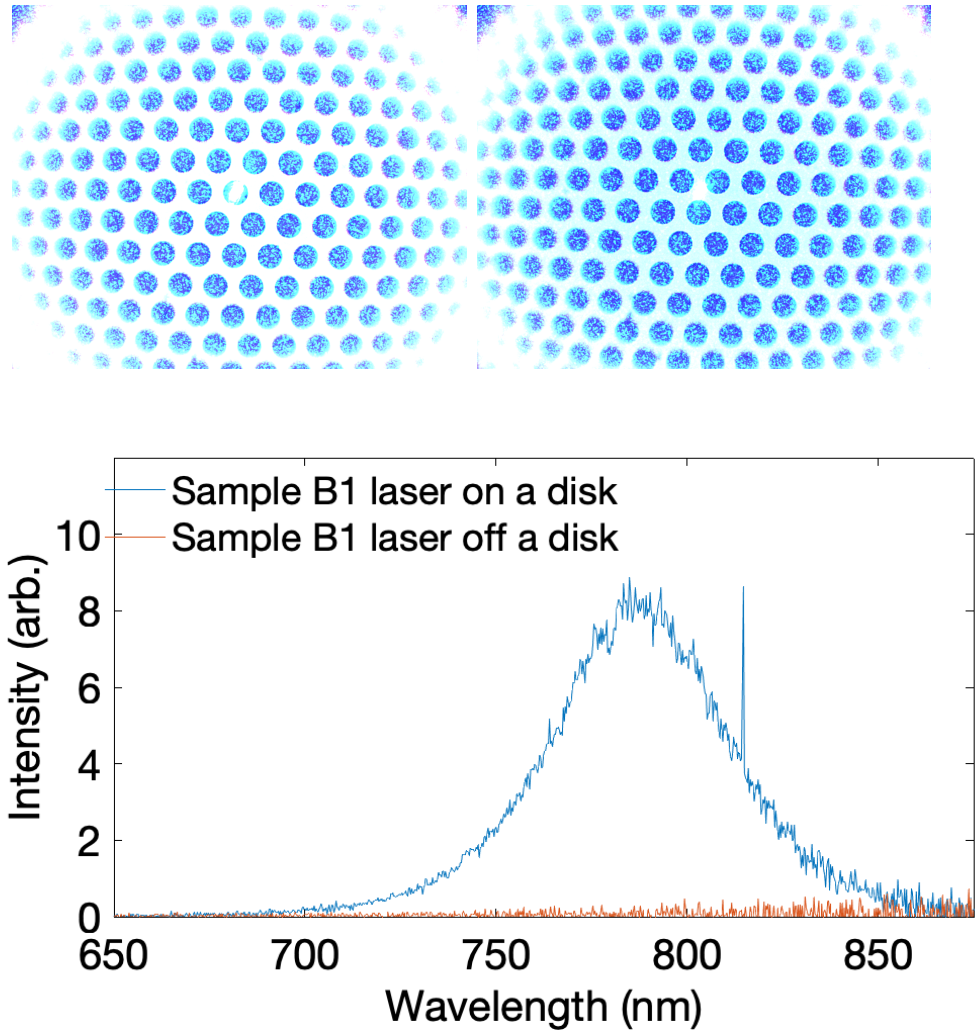


Figure 7.8: Top: View through the PL microscope. On the left with the laser aligned on one of the disks and on the right with the laser positioned off the disk. Bottom: Photoluminescence spectrum of Sample B1 (large disks, lift-off with IPA only) with the laser on a disk and off the disk.

The same PL experiment was repeated on the smaller 9 μm disks and the samples with the two different lift-off solutions and very similar results were achieved. The PL spectra for all these different photolithographically patterned films are shown in Figure

7.9. The shape and intensity of the spectra from the large 18 μm disks are very similar, irrespective of the lift-off method. In contrast for the smaller 9 μm disks, the PL intensity is higher for the sample that was lifted off using IPA with FAI as an additive. This effect was observed in multiple measurements but additional samples are necessary to confirm if it is a general effect. If so, it would indicate that at least for smaller disks the addition of FAI in the lift-off solution is beneficial.

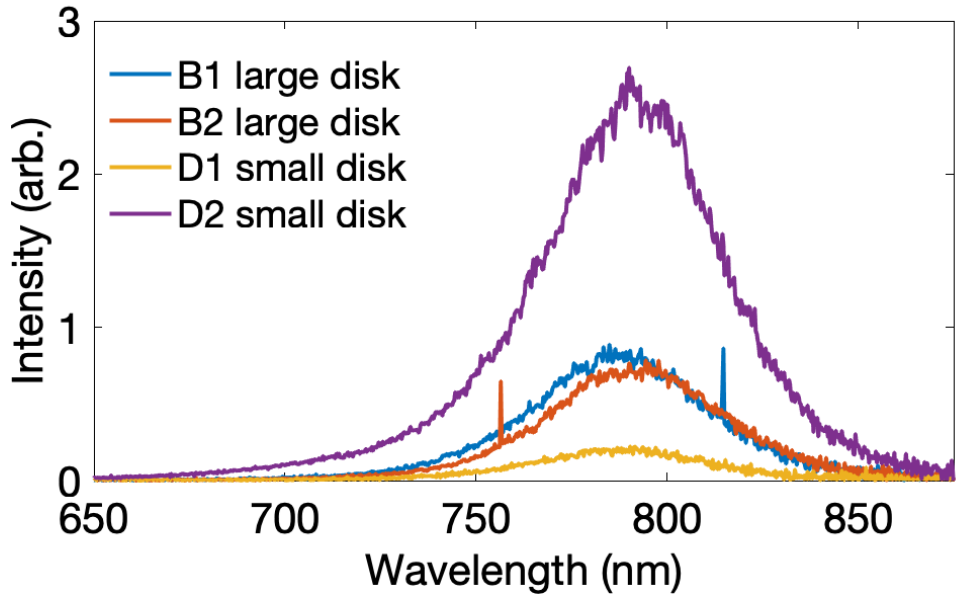


Figure 7.9: Photoluminescence spectrum of all photolithographically patterned samples. B1 and B2 are samples with large 18 μm disks, one lifted-off with IPA only (B1) and one with IPA with FAI (B2). D1 and D2 are samples with smaller 9 μm disks, one sample lifted-off with IPA only (D1) and one with IPA with FAI (D2).

Using image reversal photolithography, the fabrication of patterned perovskite films was achieved. Well separated disks with diameters of 18 μm or 9 μm were formed in a regular pattern over an area of several mm^2. These $FAPbI_3$ disks showed an absorption onset in the expected energy region and were semi-transparent above the bandgap. They were emissive under laser illumination and their PL spectra matched those previously measured for $FAPbI_3$. These properties make them very promising films for use in semi-transparent solar cells and lasing applications. To move further towards the goal of

amplified spontaneous emission, other substrates and smaller patterns should be studied.

7.3.2 Ion-milled patterns

To overcome the size limitations of photolithography, ion-milling was employed in collaboration with Dr Li (Lily) Li of the Department of Electronic Materials Engineering at the Australian National University (ANU). $FAPbI_3$ films were deposited on FTO substrates in Oxford and shipped to ANU for the ion-milling. Disks and rings with diameters ranging from 5 μm to 2 μm were milled into the perovskite film. An overview of such a sample is shown in Figure 7.10. Scanning electron microscopy was used at ANU to confirm the shape and dimensions of the milled features. All features had the specified dimensions.

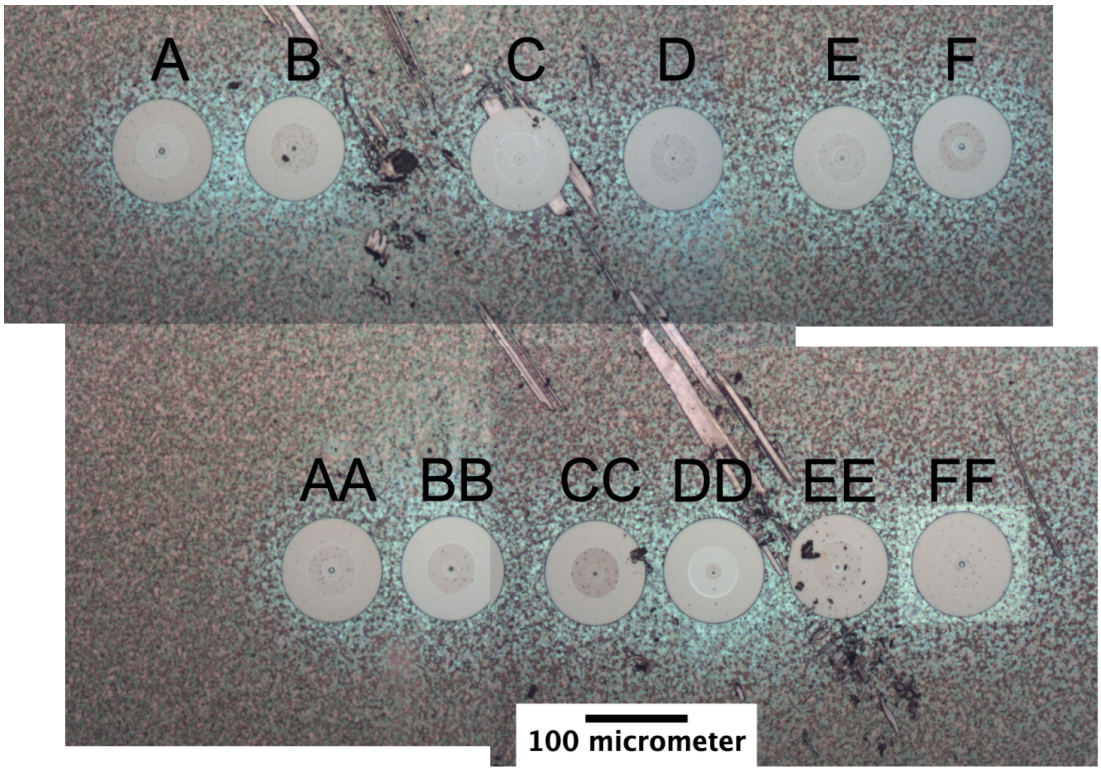


Figure 7.10: Composite of several optical microscopy images showing a range of features milled into a $FAPbI_3$ film.

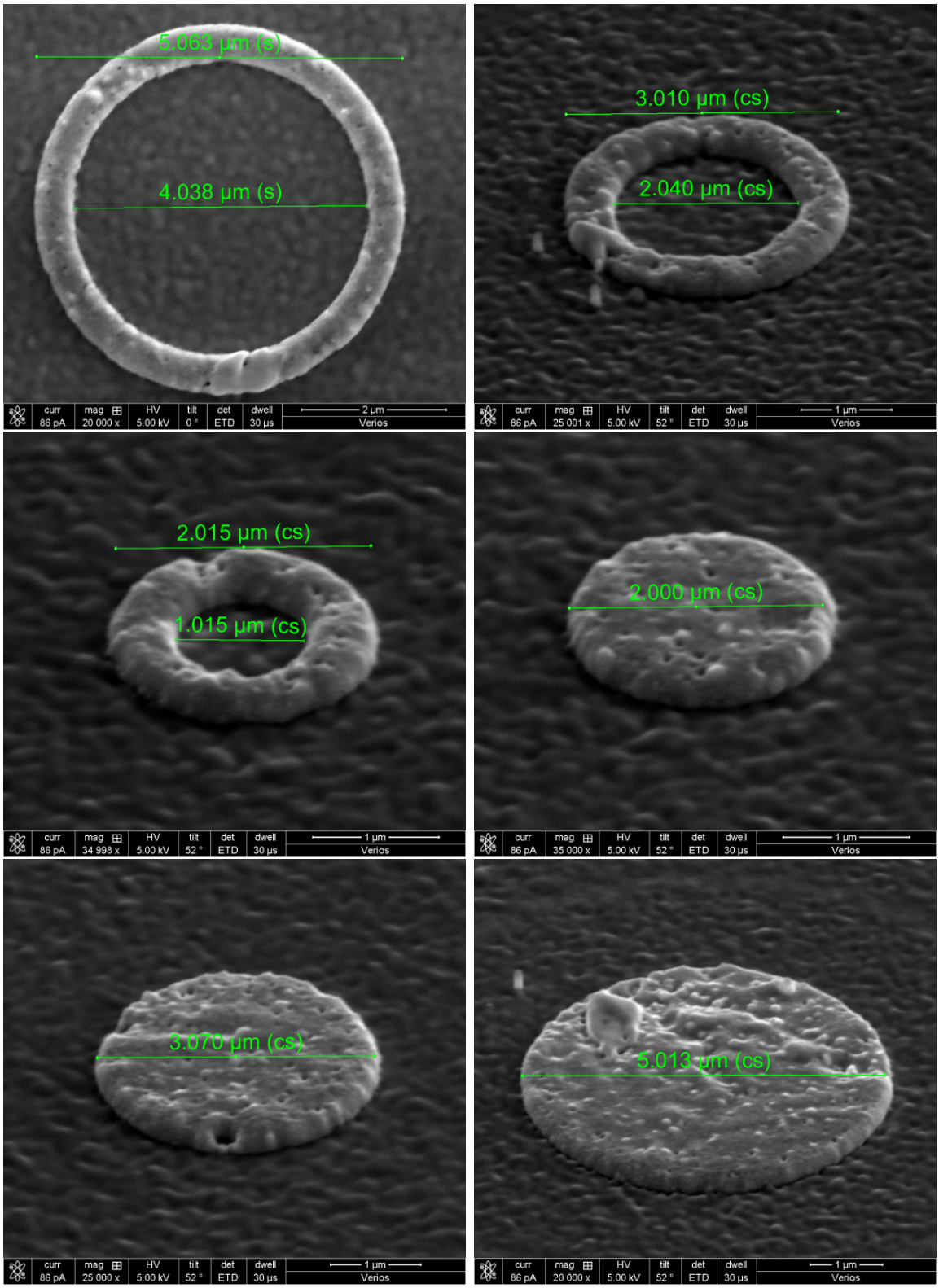


Figure 7.11: Scanning electron microscopy images taken by Dr Li Li of the ion-milled pattern milled by her.

After ion-milling and SEM measurements, the samples were sent back to Oxford for

measurements. Upon their arrival, it was noticed that most of the $FAPbI_3$ film across the samples had turned from the typical dark brown colour to yellow. This is typical for the phase transition from the perovskite $FAPbI_3$ phase to the yellow non-perovskite phase. Presumably the films were exposed to humidity during shipping or handling which triggered this phase transition. Nevertheless, in the PL microscope, they showed the expected PL spectra when the laser was positioned on the features (Figure 7.12). When the laser was moved off the feature, the PL decreased drastically. The position of the PL peak was consistent with the $FAPbI_3$ perovskite phase. This either indicates that the feature itself did not change phase with the rest of the sample, or that the energy from the laser was enough to anneal the feature back into the dark $FAPbI_3$ perovskite phase. Either way, this effect was very welcome, since it meant no annealing or other treatments were necessary to bring the samples back into the required perovskite $FAPbI_3$ phase.

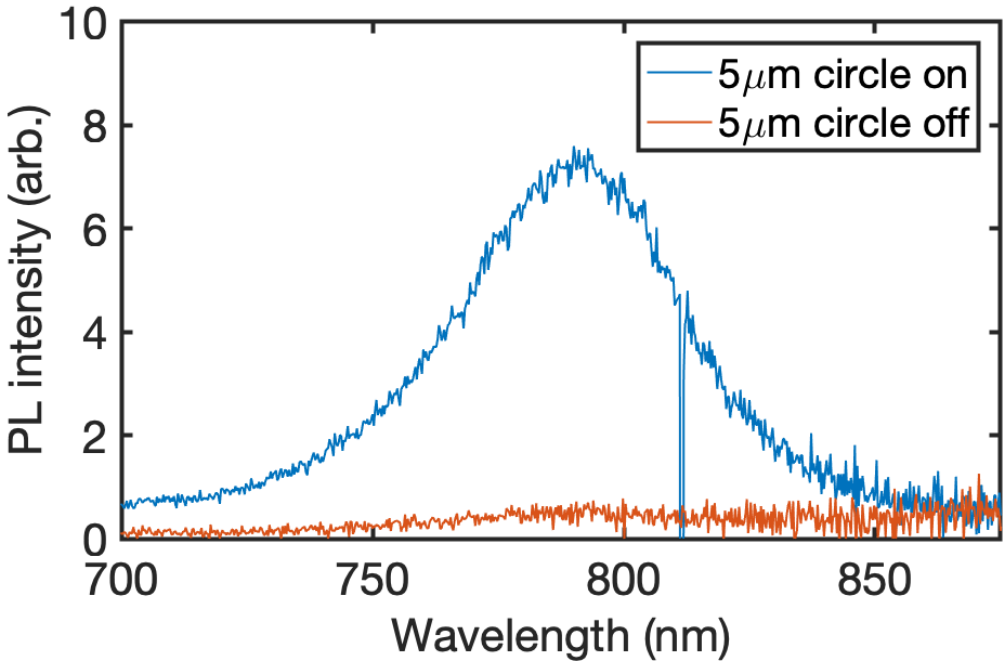


Figure 7.12: Photoluminescence spectra of the 5 μm with the laser positioned on a disk and off the disk.

When the PL spectra of all the different sized circles are compared, it is apparent that they are very similar (Figure 7.13). Only the PL spectrum of the largest circle which has

a diameter of 5 μm is a bit narrower and more intense than the other two.

In contrast, the PL spectra of the rings follow a trend. As the rings become smaller, the PL peak intensity rises. The PL spectrum of the ring with an outer diameter of 2 μm is significantly more intense than that of the 5 μm ring. To confirm this effect, this experiment would need to be repeated on more samples.

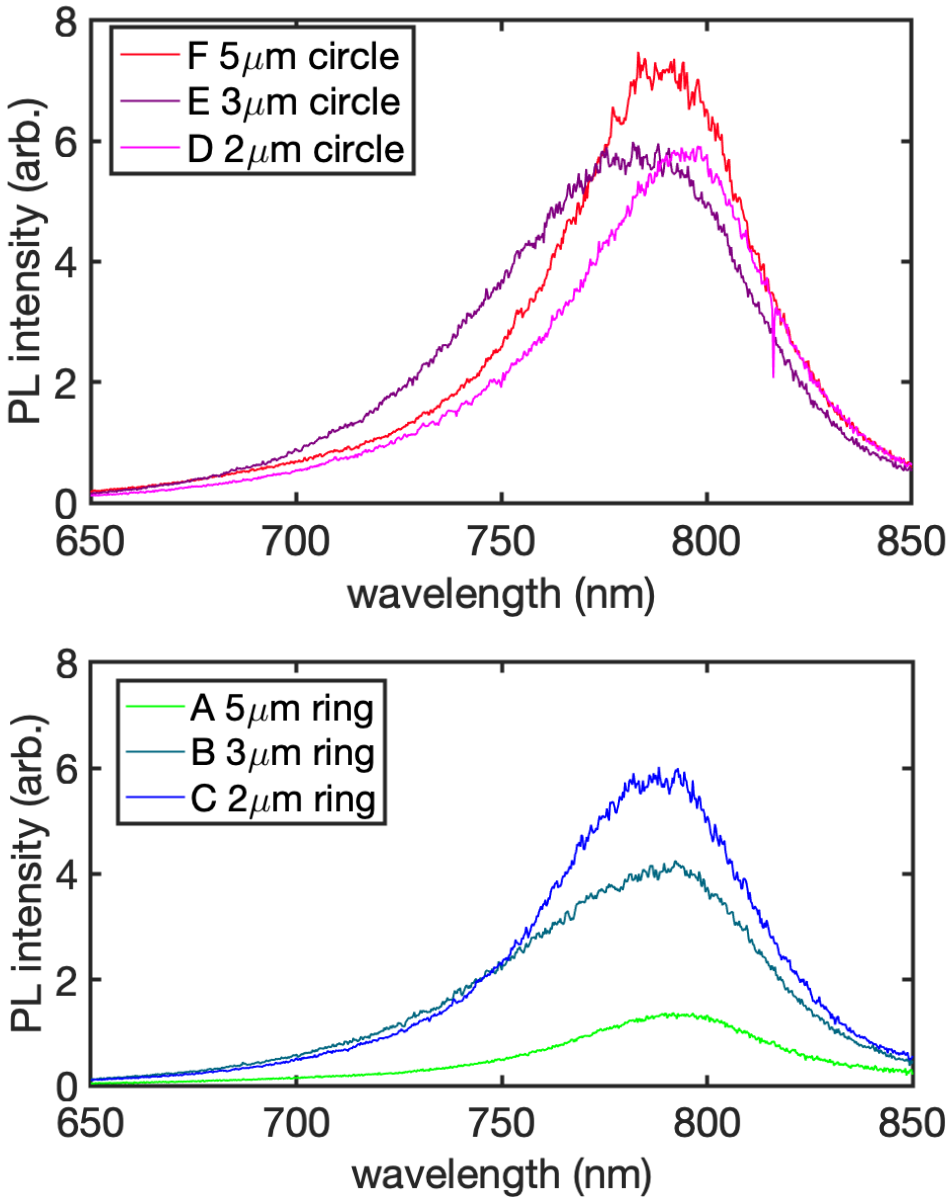


Figure 7.13: PL spectra of ion-milled $FAPbI_3$ circles (top) and rings (bottom) with outer diameters from 5 μm to 2 μm

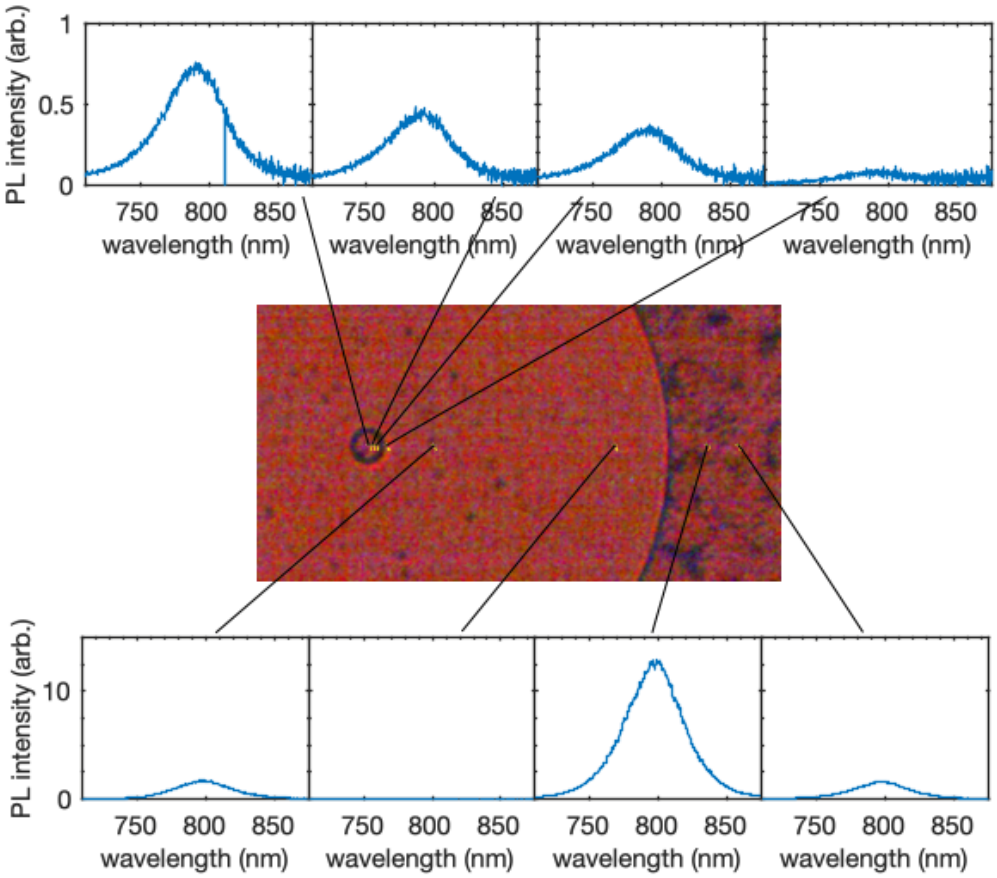


Figure 7.14: As the laser is moved from the feature onto the milled area and finally onto the continuous perovskite film, the PL spectra change accordingly. Initially, photoluminescence from the perovskite disk is measured and as the laser is moved way from it, the intensity of the photoluminescence drops. Once the laser is on the area in which the perovskite was milled away it should not give any signal. This is the case, expect in a few areas where the milling was incomplete and residual perovskite remains. Finally, when the laser is positioned on the continuous perovskite film, outside the milled area, a strong photoluminescence signal is again recorded.

To study the PL across the sample, the stages were moved step by step to change the position of the laser from being directly on the feature to far away from the feature, on the continuous $FAPbI_3$ film. The results from the 5 μm circle are shown in Figure 7.14. Initially, the laser is directly on the $FAPbI_3$ circle which leads to a strong PL signal. As the laser moves off the circle, the PL intensity decreases until it is nearly

gone. Then as the laser moves across the bare FTO substrates, the PL intensity is low, except for a few spots that have residual $FAPbI_3$ which gives a PL signal. Finally, the laser reaches the un-milled $FAPbI_3$ film and the PL intensity increases but varies from spot to spot, presumably depending on the local film quality. The laser fluence was varied to study the response of these ion-milled features under varying illumination levels. For all of these spectra, the value of the maximum PL intensity was determined and plotted in the overview in Figure 7.15.

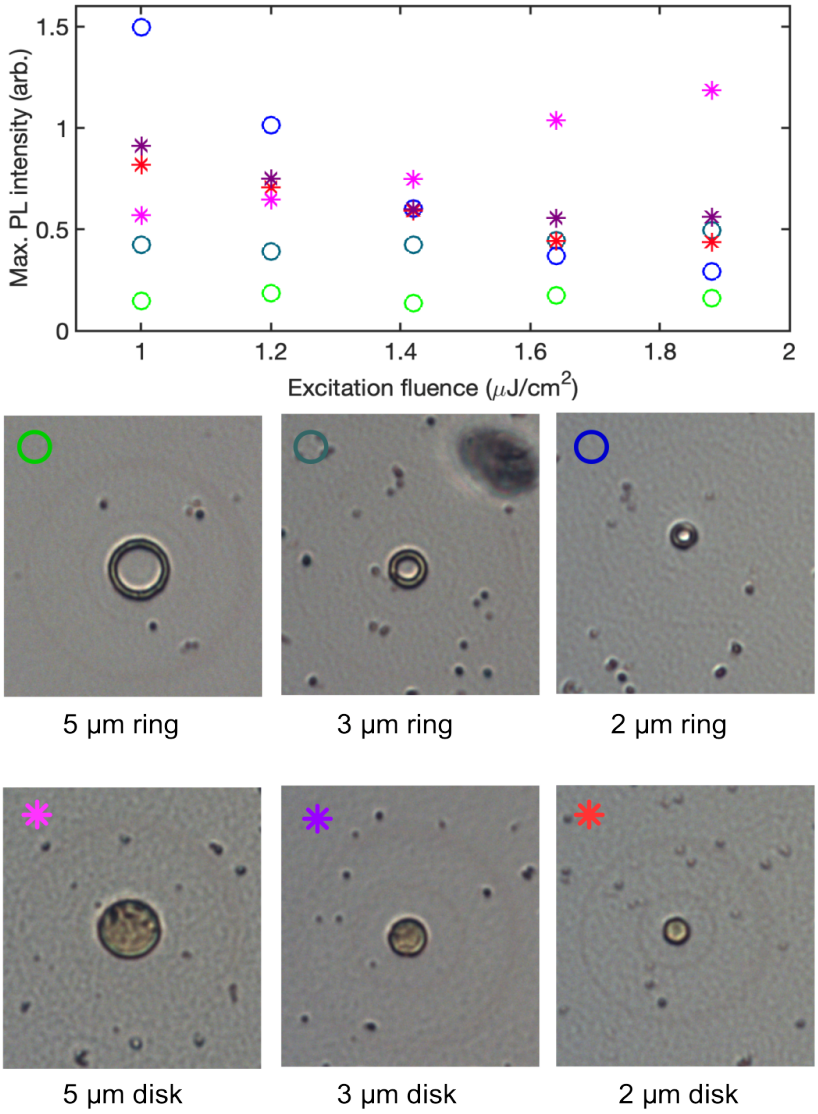


Figure 7.15: Overview of the maximal PL intensity under different excitation intensities for six different ion-milled features. Optical microscopy images of the features are shown below.

For the two largest rings with diameters 5 μm and 3 μm, the PL intensity rises as the laser power is increased (Figure 7.15). The same effect can also be observed for the largest disk (5 μm diameter).

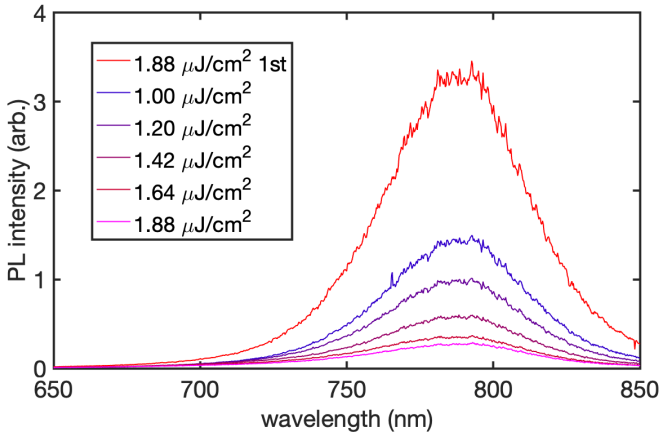


Figure 7.16: Photoluminescence spectra of a 2 μm ring (feature C) with increasing laser fluence. The spectra are plotted in the order they were measured in.

In contrast, the smallest ring (diameter 2 μm) shows the opposite behaviour. For this sample, the PL intensity falls as the laser fluence is increased. This matches the order in which the measurements were performed. This is particularly evident in the spectra from the smallest ring (Figure 7.16) since the highest laser fluence was used both in the first and the last measurement which makes a direct comparison possible. The first measurement was done with the highest laser fluence (red line). Then the fluence was decreased to the lowest used fluencer and then increased step by step back to the highest. When comparing the two measurements, which were both performed with the highest laser fluence, it is evident that the first measurement has a much higher PL intensity than the last measurements even though the same laser intensity was used. This clearly indicates that in this sample a degradation of the PL intensity over time dominates over any increase caused by an increase in the laser fluence.

This is also the case for the two smallest disks (3 and 2 μm diameter) for which the PL intensity also decreases with each measurement despite the laser power being increased.

It appears that some of the samples degrade quickly enough under laser illumination, that even a relatively short measurement series of only a few minutes is influenced. Yet others do not show such a drastic decay of the PL signal. The decrease of the PL intensity over time seems to occur especially on the smaller features, in particular the 3 and 2 μm disks and the 2 μm ring.

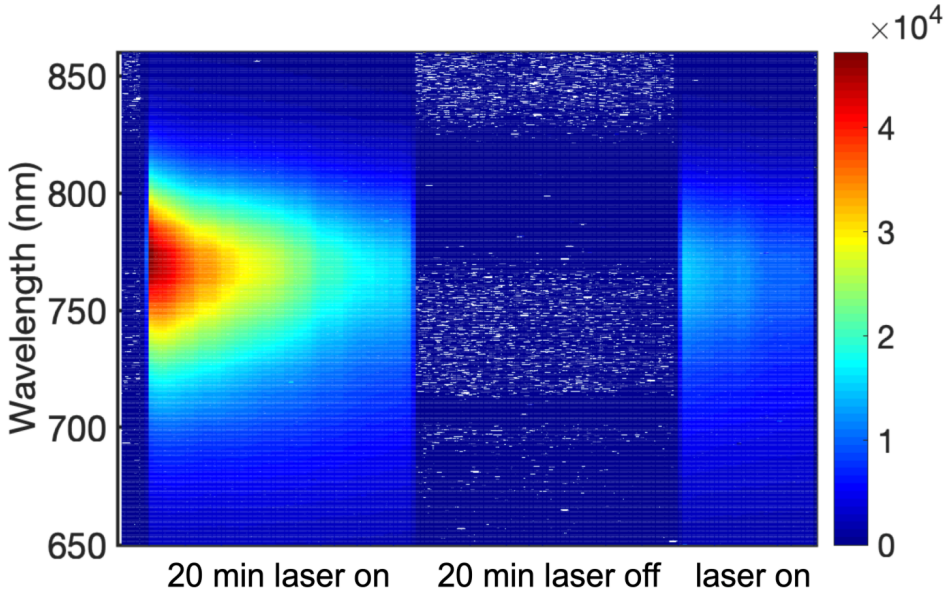


Figure 7.17: Colour map composed of photoluminescence spectra recorded from the 3 μm disk over 50 min. For the first 20 min, the laser was turned on, then it was turned off for 20 min to let the sample recover and then the laser was turned on and the sample measured again for another 10 min.

To understand the observed decrease in PL over time, additional experiments were performed. The laser, was positioned on a feature and the PL signal recorded every 10 s for 20 min. Then the laser was turned off for 20 min to allow the sample to recover. Finally, the laser was turned on again to measure the PL and check if the sample had recovered. This experiment was performed both on the largest (5 μm) and second largest (3 μm) disk. The results are shown as colour maps in Figures 7.17 and 7.18.

The photoluminescence of the 3 μm disk decreases significantly over the first 20 min of illumination Figure 7.17. This is consistent with the earlier described behaviour of this sample during repeated measurements. After 20 min in the dark, the PL signal does not significantly recover but stays low and falls further during the second illumination period. This non-recoverable decay of the PL intensity would make it impossible to measure the influence of other factors such as the laser fluence as any other effect would be overpowered by the PL decreasing from measurement to measurement.

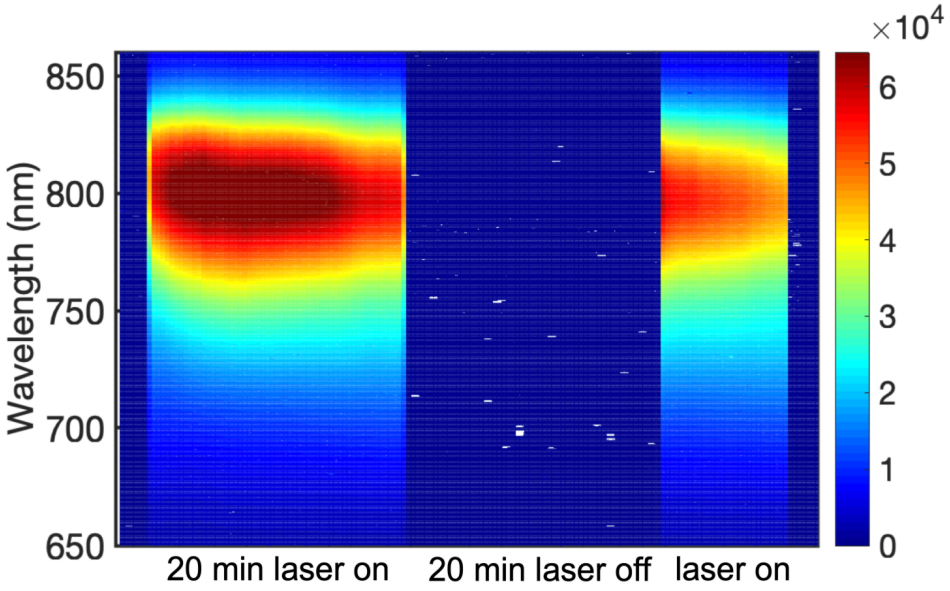


Figure 7.18: Colour map composed of photoluminescence spectra recorded from the 5 μm disk over 50 min. For the first 20 min, the laser was turned on, then it was turned off for 20 min to let the sample recover and then the laser was turned on and the sample measured again for another 10 min.

In contrast, the larger 5 μm disk does not show such an extensive decrease of the PL intensity (Figure 7.18). The intensity does decrease during laser exposure, but then appears to stabilise. After the laser has been off for 20 min, the PL continues to slowly decrease further. This comparatively stable PL emission from the 5 μm disk is consistent

with the fluence behaviour observed for this feature. For this larger disk, the PL intensity does not decay so quickly that it masks the rise of the PL with increased laser fluence.

7.4 Conclusion and outlook

For the first time, it was shown that patterning of co-evaporated $FAPbI_3$ films is possible. Micrometre-sized disks and rings were fabricated using photolithography and ion-milling. These are versatile approaches which enable a high degree of design flexibility. Various sizes from 18 μm diameter to 2 μm diameter were achieved. The minimal size for the photolithography is currently around 8 μm which could be further decreased through optimisation of the lift-off step of the photolithography. When ion-milling is used, features as small as a 2 μm diameter ring with a 500 nm linewidth were achieved.

Despite the rather harsh processing conditions, the patterned $FAPbI_3$ photoluminesces rather strongly which demonstrates that the processing did not overly damage the film. This is especially surprising for the ion-milled films since the overall sample had changed colour from brown to yellow indicating a phase transition to the undesired non-perovskite $FAPbI_3$ phase. Either the ion-milled features had not undergone this transition or the excitation laser for the photoluminescence measurement provided enough energy to anneal the feature back into the desired perovskite $FAPbI_3$ phase. Either way, photoluminescence was observed even from the smallest fabricated features. Unfortunately, the photoluminescence of some features was not very stable and decayed over time. Further studies with more samples are necessary to determine if this decay is size dependent and how it could be prevented. Especially the photoluminescence measurements on the ion-milled samples should be continued on more samples to confirm some of the observed trends.

To build on the important achievements presented in this chapter, the photoluminescence efficiency should be increased to move towards amplified spontaneous emission and

lasing. This could be achieved by using a different substrate or via after-treatments to tune the film properties. To apply the photo-lithographically patterned films in semi-transparent solar cells, they would need to be combined with shunt blocking and contact layers to form a full solar cell. Overall co-evaporation combined with photolithography or ion-milling were shown to be a promising approach towards the fabrication of a co-evaporated metal-halide perovskite disk laser.

8
Conclusion and Outlook

In this thesis, the co-evaporation of hybrid organic-inorganic metal-halide perovskites was developed further as a method and applied to a material and a field of application it had not been used for before. This work also provides insights into the mechanism that govern the co-evaporation of perovskite thin-films and has enabled studies into the optoelectronic properties of these materials.

In Chapter 5, it was demonstrated that very uniform $FAPbI_3$ thin-films can be deposited using co-evaporation. From these films, efficient $FAPbI_3$ solar cells were fabricated which are an important milestone towards the fabrication of highly efficient, co-evaporated perovskite solar cells with mixed compositions. The ability to deposit very planar and smooth $FAPbI_3$ thin-films has already enabled a further study into the properties of $FAPbI_3$ and two further studies into the optoelectronic and crystallographic properties of $FAPbI_3$ based on these films are ongoing. In Chapter 5.6, the influence of impurities on the co-evaporation of $MAPbI_3$ was studied in detail using mass-spectroscopy, nuclear magnetic resonance, X-ray diffraction, scanning electron microscopy, spectroscopy in the infra-red and visible, and solar cell J-V curves. It was shown that impurities

do not directly influence the efficiency of the fabricated solar cells but do drastically alter the readings of the quartz microbalance which is used to control the deposition process. Variations in impurity concentration between MAI batches complicate the process control and explain problems with the MAI rate control which have frequently been reported in the literature. These results resolve a long standing issue in the field and yield recommendations to make co-evaporation of perovskites even more reliable and reproducible in the future. The lessons learned in the two first chapters were then applied to move beyond solar cells and fabricate patterned perovskite films for micro-lasing applications. The additive nature of the co-evaporation was utilised to photolithographically pattern $FAPbI_3$ into small micro-disks. It was shown that patterning is also possible using ion-milling. In both cases, the processed films showed the expected photoluminescence which demonstrates that the optoelectronic properties were conserved even after the patterning steps. This demonstrates the potential of this approach for the fabrication of semi-transparent solar cells and micro-lasers. The used methods offer a high degree of control over the shape of the fabricated features. This is the first time that such patterned perovskite films have been realised with a vacuum based evaporation technique.

Three important themes will dominate the future of the field of hybrid organic-inorganic metal-halide perovskite solar cells, they are stability, up-scaling and tandem solar cells. The work presented in this thesis will inform future research in all three of these areas. The ability to evaporate $FAPbI_3$ will enable the vacuum fabrication of the more stable and tuneable mixed perovskites which are needed in tandem applications and to improve stability. For this the development and precise control of multi-source vacuum deposition processes will be necessary, which will benefit from the insights into the impact of impurities and the evaporation of formamidinium iodide, which were gained in this

thesis. The understanding gained about the influence of impurities will also further the up-scaling of perovskite thin-film deposition to an industrial scale. Finally being able to pattern evaporated perovskite thin-films opens up a range of new applications from semi-transparent solar cells to micro-lasing. In this thesis, it was demonstrated that patterning of evaporated perovskite films is possible. Next steps towards evaporated perovskite micro-lasers, would be the optimisation of the used substrates, patterning steps and optical pumping set up to demonstrate lasing from these patterned films. Subsequently, other patterns as well as architectures for electrically driven lasing should be explored which opens up a whole new field of applications for co-evaporated hybrid metal-halide perovskite thin-films.

References

[1] Arvizu, D.; Balaya Singapore, P.; Cabeza, L. F.; Terry Hollands, K.; Jäger-Waldau Italy, A.; Kondo, M.; Konseibo, C.; Meleshko, V.; Stein, W.; Tamaura, Y. *et al.* 'Direct Solar Energy'. *IPPC Special Report on Renewable Energy Sources and Climate Change Mitigation*. Cambridge University Press, 2011. Chap. Direct Solar Energy.

[2] Feron, S. 'Sustainability of Off-Grid Photovoltaic Systems for Rural Electrification in Developing Countries: A Review'. *Sustainability*, 2016, **8**, 1326.

[3] NASA. 'STS-117 Press Kit'. 2006.

[4] Crisp, D.; Pathare, A. and Ewell, R. C. 'The Performance of Gallium Arsenide/Germanium Solar Cells at the Martian Surface'. *Acta Astronautica*, 2004, **54**, 83–101.

[5] Landis, G. A. 'Exploring Mars with Solar-Powered Rovers'. *Conference Record of the Thirty-first IEEE Photovoltaic Specialists Conference, 2005.* 2005, 858–861.

[6] Stoumpos, C. C.; Malliakas, C. D. and Kanatzidis, M. G. 'Semiconducting Tin and Lead Iodide Perovskites with Organic Cations: Phase Transitions, High Mobilities, and Near-infrared Photoluminescent Properties'. *Inorganic Chemistry*, 2013, **52**, 9019–9038.

[7] Johnston, M. B. and Herz, L. M. 'Hybrid Perovskites for Photovoltaics: Charge-Carrier Recombination, Diffusion, and Radiative Efficiencies'. *Accounts of Chemical Research*, 2016, **49**, 146–154.

[8] Seo, J.; Noh, J. H. and Seok, S. I. 'Rational Strategies for Efficient Perovskite Solar Cells'. *Accounts of Chemical Research*, 2016, **49**, 562–572.

[9] Kojima, A.; Teshima, K.; Miyasaka, T. and Shirai, Y. 'Novel Photoelectrochemical Cell with Mesoscopic Electrodes Sensitized by Lead-halide Compounds'. *Meeting Abstracts 210 th ECS Meeting*, 2006, **210**, 2151–2043.

[10] Liu, M.; Johnston, M. B. and Snaith, H. J. 'Efficient Planar Heterojunction Perovskite Solar Cells by Vapour Deposition'. *Nature*, 2013, **501**, 395–398.

[11] Yang, W. S.; Noh, J. H.; Jeon, N. J.; Kim, Y. C.; Ryu, S.; Seo, J. and Seok, S. I. 'High-Performance Photovoltaic Perovskite Layers Fabricated through Intramolecular Exchange'. *Science*, 2015, **348**, 1234–1237.

[12] Jung, E. H.; Jeon, N. J.; Park, E. Y.; Moon, C. S.; Shin, T. J.; Yang, T.-Y.; Noh, J. H. and Seo, J. 'Efficient, Stable and Scalable Perovskite Solar Cells using Poly(3-hexylthiophene)'. *Nature*, 2019, **567**, 511–515.

[13] Cho, H.; Jeong, S. H.; Park, M. H.; Kim, Y. H.; Wolf, C.; Lee, C. L.; Heo, J. H.; Sadhanala, A.; Myoung, N. S.; Yoo, S. *et al.* 'Overcoming the Electroluminescence Efficiency Limitations of Perovskite Light-emitting Diodes'. *Science*, 2015, **350**, 1222–1225.

[14] Kim, Y. H.; Cho, H.; Heo, J. H.; Kim, T. S.; Myoung, N. S.; Lee, C. L.; Im, S. H. and Lee, T. W. 'Multicolored Organic/Inorganic Hybrid Perovskite Light-Emitting Diodes'. *Advanced Materials*, 2015, **27**, 1248–1254.

[15] Tan, Z. K.; Moghaddam, R. S.; Lai, M. L.; Docampo, P.; Higler, R.; Deschler, F.; Price, M.; Sadhanala, A.; Pazos, L. M.; Credgington, D. *et al.* 'Bright Light-emitting Diodes Based on Organometal Halide Perovskite'. *Nature Nanotechnology*, 2014, **9**, 687–692.

[16] Kagan, C.; Mitzi, D. B. and Dimitrakopoulos, C. D. 'Organic-Inorganic Hybrid Materials as Semiconducting Channels in Thin-Film Field-Effect Transistors'. *Science*, 1999, **286**, 945–947.

[17] Matsushima, T.; Hwang, S.; Sandanayaka, A. S.; Qin, C.; Terakawa, S.; Fujihara, T.; Yahiro, M. and Adachi, C. 'Solution-Processed Organic–Inorganic Perovskite Field-Effect Transistors with High Hole Mobilities'. *Advanced Materials*, 2016, **28**, 10275–10281.

[18] Spindler, J. P.; Hamer, J. W. and Kondakova, M. E. 'OLED Manufacturing Equipment and Methods'. *Handbook of Advanced Lighting Technology*. Ed. by Karlicek, R.; Sun, C.-C.; Zissis, G. and Ma, R. Cham: Springer International Publishing, 2017, 417–441.

[19] Tsujimura, T. *OLED Display Fundamentals and Applications 2nd*. Wiley Series in Display Technology. 2017.

[20] Nelson, J. *The Physics of Solar Cells*. Imperial College Press, 2003.

[21] Nick84. *Solar spectrum en - Licensed under CC BY-SA 3.0 via Commons*. https://commons.wikimedia.org/wiki/File:Solar_spectrum_en.svg/media/File:Solar_spectrum_en.svg.

[22] Würfel, P. *Physics of Solar Cells: From Basic Principles to Advanced Concepts*. WILEY-VCH, 2009.

[23] Shockley, W. and Queisser, H. J. 'Detailed Balance Limit of Efficiency of p-n Junction Solar Cells'. *Journal of Applied Physics*, 1961, **32**, 510.

[24] Green, M. A. 'Third Generation Photovoltaics: Solar Cells for 2020 and Beyond'. *Physica E: Low-Dimensional Systems and Nanostructures*. Vol. 14. 2002, 65–70.

[25] Rose, G. 'Ueber Einige neue Mineralien des Urals'. *Journal für Praktische Chemie*, 1840, **19**, 459–468.

[26] Snaith, H. J. 'Perovskites: The Emergence of a New Era for Low-Cost, High-Efficiency Solar Cells'. *The Journal of Physical Chemistry Letters*, 2013, **4**, 3623–3630.

[27] Mitzi, D. B.; Feild, C.; Schlesinger, Z and Laibowitz, R. B. 'Transport, Optical, and Magnetic Properties of the Conducting Halide Perovskite $CH_3NH_3SnI_3$'. *Journal of Solid State Chemistry*, 1995, **114**, 159–163.

[28] Mitzi, D. B.; Chondroudis, K. and Kagan, C. R. 'Organic-Inorganic Electronics'. *IBM Journal of Research and Development*, 2001, **45**, 29–45.

[29] Mitzi, D. B.; Wang, S; Feild, C. a.; Chess, C. a. and Guloy, a. M. 'Conducting Layered Organic-inorganic Halides Containing <110>-Oriented Perovskite Sheets'. *Science*, 1995, **267**, 1473–1476.

[30] Green, M. A.; Ho-Baillie, A. and Snaith, H. J. 'The Emergence of Perovskite Solar Cells'. *Nature Photon*, 2014, **8**, 506–514.

[31] Kojima, A.; Teshima, K.; Shirai, Y. and Miyasaka, T. 'Organometal Halide Perovskites as Visible-Light Sensitizers for Photovoltaic Cells.' *Journal of the American Chemical Society*, 2009, **131**, 6050–1.

[32] Lee, M. M.; Teuscher, J.; Miyasaka, T.; Murakami, T. N. and Snaith, H. J. 'Efficient Hybrid Solar Cells Based on Meso-Superstructured Organometal Halide Perovskites.' *Science (New York, N.Y.)* 2012, **338**, 643–7.

[33] Saliba, M.; Matsui, T.; Seo, J.-Y.; Domanski, K.; Correa-Baena, J.-P.; Nazeeruddin, M. K.; Zakeeruddin, S. M.; Tress, W.; Abate, A.; Hagfeldt, A. *et al.* 'Cesium-Containing Triple Cation Perovskite Solar Cells: Improved Stability, Reproducibility and High Efficiency'. *Energy Environ. Sci.* 6 2016, **9**, 1989–1997.

[34] Hao, F.; Stoumpos, C. C.; Cao, D. H.; Chang, R. P. H. and Kanatzidis, M. G. 'Lead-free Solid-state Organic-inorganic Halide Perovskite Solar Cells'. *Nature Photon*, 2014, **8**, 489–494.

[35] Hoye, R. L.; Brandt, R. E.; Osherov, A.; Stevanovic, V.; Stranks, S. D.; Wilson, M. W.; Kim, H.; Akey, A. J.; Perkins, J. D.; Kurchin, R. C. *et al.* 'Methylammonium Bismuth Iodide as a Lead-Free, Stable Hybrid Organic-Inorganic Solar Absorber'. *Chemistry - A European Journal*, 2016, **22**, 2605–2610.

[36] Yang, B.; Chen, J.; Yang, S.; Hong, F.; Sun, L.; Han, P.; Pullerits, T.; Deng, W. and Han, K. 'Lead-Free Silver-Bismuth Halide Double Perovskite Nanocrystals'. *Angewandte Chemie - International Edition*, 2018, **57**, 5359–5363.

[37] Zhao, D.; Yu, Y.; Wang, C.; Liao, W.; Shrestha, N.; Grice, C. R.; Cimaroli, A. J.; Guan, L.; Ellingson, R. J.; Zhu, K. *et al.* 'Low-Bandgap Mixed Tin-lead Iodide Perovskite Absorbers with Long Carrier Lifetimes for All-perovskite Tandem Solar Cells'. *Nature Energy*, 2017, **2**, 1–7.

[38] Heo, J. H. and Im, S. H. '$CH_3NH_3PbBr_3 - CH_3NH_3PbI_3$ Perovskite-Perovskite Tandem Solar Cells with Exceeding 2.2 V Open Circuit Voltage'. *Advanced Materials*, 2015, **28**, 5121–5125.

[39] Helmholtz Center Berlin. 2019. https://www.helmholtz-berlin.de/pubbin/news_seite?nid=20769;sprache=en;seitenid=74699.

[40] Oxford Photovoltaics. 2018. https://www.oxfordpv.com/news/oxford-pv-perovskite-solar-cell-achieves-28-efficiency.

[41] Cao, D. H.; Stoumpos, C. C.; Farha, O. K.; Hupp, J. T. and Kanatzidis, M. G. 'Two-dimensional Homologous Perovskites as Light Absorbing Materials for Solar Cell Applications'. *Journal of American Chemical Society*, 2015, **137**, 78437850.

[42] Hu, Y.; Schlipf, J.; Wussler, M.; Petrus, M. L.; Jaegermann, W.; Bein, T.; Muller-Buschbaum, P. and Docampo, P. 'Hybrid Perovskite/Perovskite Heterojunction Solar Cells'. *ACS Nano*, 2016, **10**, 59996007.

[43] Koh, T. M.; Shanmugam, V.; Schlipf, J.; Oesinghaus, L.; Müller-Buschbaum, P.; Ramakrishnan, N.; Swamy, V.; Mathews, N.; Boix, P. P. and Mhaisalkar, S. G. 'Nanostructuring Mixed-Dimensional Perovskites: A Route Toward Tunable, Efficient Photovoltaics'. *Advanced Materials*, 2016, **28**, 3653–3661.

[44] Tsai, H.; Nie, W.; Blancon, J.-C.; Stoumpos, C. C.; Asadpour, R.; Harutyunyan, B.; Neukirch, A. J.; Verduzco, R.; Crochet, J. J.; Tretiak, S. *et al.* 'High-efficiency Two-dimensional Ruddlesden–Popper perovskite solar cells'. *Nature*, 2016, **536**, 312–316.

[45] Stylianakis, M. M.; Maksudov, T.; Panagiotopoulos, A. and Kymakis, E. 'Inorganic and Hybrid Perovskite Based Laser Devices : A Review'. 2019, **12**, 859.

[46] He, Y. and Galli, G. 'Perovskites for Solar Thermoelectric Applications: a First Principle Study of $CH_3NH_3AI_3$ (A=Pb and Sn)'. *Chemistry of Materials*, 2014, **26**, 5394–5400.

[47] Aharon, S.; Cohen, B.-E. E. and Etgar, L. 'Hybrid Lead Halide Iodide and Lead Halide Bromide in Efficient Hole Conductor Free Perovskite Solar Cell'. *The Journal of Physical Chemistry C*, 2014, **118**, 17160–17165.

[48] Kranz, L.; Abate, A.; Feurer, T.; Fu, F.; Avancini, E.; Lö, J.; Reinhard, P.; Zakeeruddin, S. M.; Grätzel, M.; Buecheler, S. *et al.* 'High-Efficiency Polycrystalline Thin Film Tandem Solar Cells'. *J. Phys. Chem. Lett*, 2015, **6**, 13.

[49] Bailie, C. D.; Christoforo, M. G.; Mailoa, J. P.; Bowring, A. R.; Unger, E. L.; Nguyen, W. H.; Burschka, J.; Pellet, N.; Lee, J. Z.; Grätzel, M. *et al.* 'Semi-transparent Perovskite Solar Cells for Tandems with Silicon and CIGS'. *Energy Environ. Sci.* 2014, **8**, 956–963.

[50] Mailoa, J. P.; Bailie, C. D.; Johlin, E. C.; Hoke, E. T.; Akey, A. J.; Nguyen, W. H.; Mcgehee, M. D. and Buonassisi, T. 'A 2-terminal Perovskite/Silicon Multijunction Solar Cell Enabled by a Silicon Tunnel Junction'. *Applied Physics Letters*, 2015, **106**, 121105.

[51] Lang, F.; Gluba, M. A.; Albrecht, S.; Rg Rappich, J.; Korte, L.; Rech, B. and Nickel, N. H. 'Perovskite Solar Cells with Large-Area CVD-Graphene for Tandem Solar Cells'. *J. Phys. Chem. Lett*, 2015, **6**, 55.

[52] Albrecht, S.; Saliba, M.; Correa Baena, J. P.; Lang, F.; Kegelmann, L.; Mews, M.; Steier, L.; Abate, A.; Rappich, J.; Korte, L. *et al.* 'Monolithic Perovskite/Silicon-Heterojunction Tandem Solar Cells Processed at Low Temperature'. *Energy Environ. Sci.* 2015, **9**, 81–88. eprint: 1408.1149.

[53] Zhao, D.; Wang, C.; Song, Z.; Yu, Y.; Chen, C.; Zhao, X.; Zhu, K. and Yan, Y. 'Four-Terminal All-Perovskite Tandem Solar Cells Achieving Power Conversion Efficiencies Exceeding 23%'. *ACS Energy Letters*, 2018, **3**, 305–306.

[54] Zhao, D.; Chen, C.; Wang, C.; Junda, M. M.; Song, Z.; Grice, C. R.; Yu, Y.; Li, C.; Subedi, B.; Podraza, N. J. *et al.* 'Efficient Two-terminal All-perovskite Tandem Solar Cells Enabled by High-quality Low-bandgap Absorber Layers'. *Nature Energy*, 2018, **3**, 1093–1100.

[55] Konstantakou, M. and Stergiopoulos, T. 'A Critical Review on Tin Halide Perovskite Solar Cells'. *J. Mater. Chem. A,* 2017, **5**, 11518.

[56] Giustino, F. and Snaith, H. J. 'Toward Lead-Free Perovskite Solar Cells'. *ACS Energy Lett.* 2016, **1**, 12331240.

[57] Brittman, S.; Adhyaksa, G. W. P. and Garnett, E. C. 'The Expanding World of Hybrid Perovskites: Materials Properties and Emerging Applications'. *MRS Communications*, 2015, 1–20.

[58] Ito, S.; Tanaka, S.; Manabe, K. and Nishino, H. 'Effects of Surface Blocking Layer of $Sb_2S_3 on Nanocrystalline TiO_2 for CH_3NH_3PbI_3 Perovskite Solar Cells$'. *The Journal of Physical Chemistry C*, 2014, **118**, 16995–17000. eprint: http://dx.doi.org/10.1021/jp500449z.

[59] Abrusci, A.; Stranks, S. D.; Docampo, P.; Yip, H.-L.; Jen, A. K.-Y. and Snaith, H. J. 'High-Performance Perovskite-Polymer Hybrid Solar Cells via Electronic Coupling with Fullerene Monolayers'. *Nano Letters*, 2013, **13**, 3124–3128.

[60] You, J.; Hong, Z.; Yang, Y. M.; Chen, Q.; Cai, M.; Song, T.-b.; Chen, C.-c.; Lu, S.; Liu, Y.; Zhou, H. *et al.* 'Low-temperature Solution-processed Perovskite Solar Cells with High Efficiency and Flexibility.' *ACS Nano*, 2014, **8**, 1674–80.

[61] Zhu, Z.; Bai, Y.; Zhang, T.; Liu, Z.; Long, X.; Wei, Z.; Wang, Z.; Zhang, L.; Wang, J.; Yan, F. *et al.* 'High-Performance Hole-Extraction Layer of Sol-Gel-Processed NiO Nanocrystals for Inverted Planar Perovskite Solar Cells'. *Angewandte Chemie*, 2014, **126**, 1 –6.

[62] Qin, P.; Tanaka, S.; Ito, S.; Tetreault, N.; Manabe, K.; Nishino, H.; Nazeeruddin, M. K. and Tzel, M. G. A. 'Inorganic Hole Conductor-based Lead Halide Perovskite Solar Cells with 12.4% Conversion Efficiency'. *Nature Communications*, 2014, **5**, 3384.

[63] Zhao, Y.; Nardes, A. M. and Zhu, K. 'Effective hole extraction using $MoO_x - Alcontactinperovskite CH_3NH_3PbI_3 solarcells$'. *Applied Physics Letters*, 2014, **104**, 213906.

[64] Kim, H.-S.; Lee, C.-R.; Im, J.-H.; Lee, K.-B.; Moehl, T.; Marchioro, A.; Moon, S.-J.; Humphry-Baker, R.; Yum, J.-H.; Moser, J. E. *et al.* 'Lead Iodide Perovskite Sensitized All-solid-state Submicron Thin Film Mesoscopic Solar Cell with Efficiency Exceeding 9%'. *Scientific reports*, 2012, **2**, 591.

[65] Herz, L. M. 'Charge-Carrier Mobilities in Metal Halide Perovskites: Fundamental Mechanisms and Limits'. *ACS Energy Lett.* 2017, **2**.

[66] Wehrenfennig, C.; Liu, M.; Snaith, H. J.; Johnston, M. B. and Herz, L. M. 'Charge-carrier Dynamics in Vapour-deposited Films of the Organolead Halide Perovskite $CH_3NH_3PbI_{3x}Cl_x$'. *Energy & Environmental Science*, 2014, **7**, 2269.

[67] Rehman, W.; Milot, R. L.; Eperon, G. E.; Wehrenfennig, C.; Boland, J. L.; Snaith, H. J.; Johnston, M. B. and Herz, L. M. 'Charge-Carrier Dynamics and Mobilities in Formamidinium Lead Mixed-Halide Perovskites'. *Advanced Materials*, 2015, **27**, 7938–7944.

[68] Herz, L. M. 'Charge Carrier Dynamics in Organic-inorganic Metal Halide Perovskites'. *Annu. Rev. Phys. Chem.* 2016, **67**, 65–89.

[69] Eperon, G. E.; Burlakov, V. M.; Goriely, A. and Snaith, H. J. 'Neutral Color Semitransparent Microstructured Perovskite Solar Cells.' *ACS nano*, 2014, **8**, 591–8.

[70] Davies, C. L.; Borchert, J.; Xia, C. Q.; Milot, R. L.; Kraus, H.; Johnston, M. B. and Herz, L. M. 'Impact of the Organic Cation on the Optoelectronic Properties of Formamidinium Lead Triiodide'. *The Journal of Physical Chemistry Letters*, 2018, 4502–4511.

[71] Hao, F.; Stoumpos, C. C.; Chang, R. P. H. and Kanatzidis, M. G. 'Anomalous Band Gap Behavior in Mixed Sn and Pb Perovskites Enables Broadening of Absorption Spectrum in Solar Cells.' *Journal of the American Chemical Society*, 2014, **136**, 8094–8099.

[72] Im, J.-H.; Lee, C.-R.; Lee, J.-W.; Park, S.-W. and Park, N.-G. '6.5% Efficient Perovskite Quantum-Dot-Sensitized Solar Cell.' *Nanoscale*, 2011, **3**, 4088–93.

[73] Joong Jeon, N.; Hong Noh, J.; Chan Kim, Y.; Seok Yang, W.; Ryu, S. and Il Seok, S. 'Solvent Engineering for High-performance Inorganic-organic Hybrid Perovskite Solar Cells'. *NATURE MATERIALS*, 2014, **13**, 897–903.

[74] Noel, N. K.; Habisreutinger, S. N.; Wenger, B.; Klug, M. T.; Hörantner, M. T.; Johnston, M. B.; Nicholas, R. J.; Moore, D. T. and Snaith, H. J. 'A Low Viscosity, Low Boiling Point, Clean Solvent System for the Rapid Crystallisation of Highly Specular Perovskite Films'. *Energy Environmental Science*, 2017, **10**, 145–152.

[75] Xiao, M.; Huang, F.; Huang, W.; Dkhissi, Y.; Zhu, Y.; Etheridge, J.; Gray-Weale, A.; Bach, U.; Cheng, Y. B. and Spiccia, L. 'A Fast Deposition-crystallization Procedure for Highly Efficient Lead Iodide Perovskite Thin-film Solar Cells'. *Angewandte Chemie - International Edition*, 2014, **53**, 9898–9903.

[76] Huang, F.; Dkhissi, Y.; Huang, W.; Xiao, M.; Benesperi, I.; Rubanov, S.; Zhu, Y.; Lin, X.; Jiang, L.; Zhou, Y. *et al.* 'Gas-assisted Preparation of Lead Iodide Perovskite Films Consisting of a Monolayer of Single Crystalline Grains for High Efficiency Planar Solar Cells'. *Nano Energy*, 2014, **10**, 10–18.

[77] Burschka, J.; Pellet, N.; Moon, S.-J.; Humphry-Baker, R.; Gao, P.; Nazeeruddin, M. K. and Grätzel, M. 'Sequential Deposition as a Route to High-performance Perovskite-sensitized Solar Cells'. *Nature*, 2013, **499**, 316–319.

[78] Chen, Q.; Zhou, H.; Hong, Z.; Luo, S.; Duan, H.-S.; Wang, H.-H.; Liu, Y.; Li, G. and Yang, Y. 'Planar Heterojunction Perovskite Solar Cells via Vapor Assisted Solution Process'. *Journal of the American Chemical Society*, 2014, **136**, 622–625.

[79] Roldán-Carmona, C.; Malinkiewicz, O.; Soriano, A.; Mínguez Espallargas, G.; Garcia, A.; Reinecke, P.; Kroyer, T.; Dar, M. I.; Nazeeruddin, M. K. and Bolink, H. J. 'Flexible High Efficiency Perovskite Solar Cells'. *Energy & Environmental Science*, 2014, **7**, 994.

[80] Sessolo, M.; Momblona, C.; Gil-Escrig, L. and Bolink, H. J. 'Photovoltaic Devices Employing Vacuum-deposited Perovskite Layers'. English. *MRS Bulletin*, 2015, **40**, 660–666.

[81] Ono, L. K.; Leyden, M. R.; Wang, S. and Qi, Y. 'Organometal Halide Perovskite Thin Films and Solar Cells by Vapor Deposition'. *J. Mater. Chem. A*, 2015, **00**, 1–21.

[82] Chen, C.-W.; Kang, H.-W.; Hsiao, S.-Y.; Yang, P.-F.; Chiang, K.-M. and Lin, H.-W. 'Efficient and Uniform Planar-Type Perovskite Solar Cells by Simple Sequential Vacuum Deposition'. *Advanced Materials*, 2014, 1–6.

[83] Ng, A.; Ren, Z.; Shen, Q.; Cheung, S. H.; Gokkaya, H. C.; Bai, G.; Wang, J.; Yang, L.; So, S. K.; Djurišić, A. B. *et al.* 'Efficiency Enhancement by Defect Engineering in Perovskite Photovoltaic Cells Prepared Using Evaporated $PbI_2/CH_3NH_3IMultilayers$'. *J. Mater. Chem. A*, 2015, **3**, 9223–9231.

[84] Mitzi, D. B.; Prikas, M. T. and Chondroudis, K. 'Thin Film Deposition of Organic-inorganic Hybrid Materials Using a Single Source Thermal Ablation Technique'. *Chemistry of Materials*, 1999, **11**, 542–544.

[85] Longo, G.; Gil-Escrig, L.; Degen, M. J.; Sessolo, M. and Bolink, H. J. 'Perovskite Solar Cells Prepared by Flash Evaporation'. *Chem. Commun. Chem. Commun*, 2015, **7376**, 7376–7378.

[86] Hanlon, J. F.; Kelsey, R. J. and Forcinio, H. E. *Handbook of Package Engineering*. eng. CRC Press, 2015.

[87] Tang, C. W. and S. A. VanSlyke. 'Organic Electroluminescent Diodes'. *Appl. Phys. Lett.* 1987, **51**, 913.

[88] Neugebauer, C. A. 'Handbook of Thin Film Technology'. McGraw-Hill Book Company, 1970. Chap. 8.

[89] Merwe, J. H. van der. 'Misfitting Monolayers and Oriented Overgrowth'. *Discuss. Faraday Soc.* 1949, **5**, 201–214.

[90] Volmer, A and Weber, A. 'Keimbildung in Übersättigten Gebilden'. *Zeitschrift für Physikalische Chemie*, 1926, **119U**, 277–301.

[91] Stranski, I. N. and Krastanow, L. 'Zur Theorie der Orientierten Ausscheidung von Ionenkristallen Aufeinander'. *Monatshefte für Chemie und verwandte Teile anderer Wissenschaften*, 1937, **71**, 351–364.

[92] *Growth Modes*. https://en.wikipedia.org/wiki/Stranski%E2%80%93Krastanov_growth#/media/File:GrowthModes.png.

[93] Johannsmann, D. *The Quartz Crystal Microbalance in Soft Matter Research*. Springer, 2015.

[94] Sauerbrey, G. 'Verwendung von Schwingquarzen zur Wägung dünner Schichten und zur Mikrowägung'. *Zeitschrift für Physik*, 1959, **155**, 206–222.

[95] Wittich, C.; Mankel, E.; Clemens, O.; Lakus-Wollny, K.; Mayer, T.; Jaegermann, W. and Kleebe, H.-J. 'Structural and Compositional Characteristics of Vacuum Deposited Methylammonium Lead Halide Perovskite Layers in Dependence on Background Pressure and Substrate Temperature'. *Thin Solid Films*, 2018, **650**, 51–57.

[96] Leyden, M. R.; Jiang, Y. and Qi, Y. 'Chemical Vapor Deposition Grown Formamidinium Perovskite Solar Modules with High Steady State Power and Thermal Stability'. *Journal of Materials Chemistry A*, 2016, 13125.

[97] Borchert, J.; Milot, R. L.; Patel, J. B.; Davies, C. L.; Wright, A. D.; Martínez Maestro, L.; Snaith, H. J.; Herz, L. M. and Johnston, M. B. 'Large-Area, Highly Uniform Evaporated Formamidinium Lead Triiodide Thin Films for Solar Cells'. *ACS Energy Letters*, 2017, **2**, 2799–2804.

[98] Longo, G.; Momblona, C.; La-Placa, M.-G.; Gil-Escrig, L.; Sessolo, M. and Bolink, H. J. 'Fully Vacuum-Processed Wide Band Gap Mixed-Halide Perovskite Solar Cells'. *ACS Energy Letters*, 2018, **3**, 214–219.

[99] Erdenebileg, E.; Scholz, L. E.; Hofacker, A.; Koerner, C. and Leo, K. 'Very Small Inverted Hysteresis in Vacuum-Deposited Mixed Organic-Inorganic Hybrid Perovskite Solar Cells'. *Energy Technology*, 2017, **5**, 1606–1611.

[100] Patel, J. B.; Wong-Leung, J.; Van Reenen, S.; Sakai, N.; Wang, J. T. W.; Parrott, E. S.; Liu, M.; Snaith, H. J.; Herz, L. M. and Johnston, M. B. 'Influence of Interface Morphology on Hysteresis in Vapor-Deposited Perovskite Solar Cells'. *Advanced Electronic Materials*, 2016, 1600470.

[101] Patel, J. B.; Milot, R. L.; Wright, A. D.; Herz, L. M. and Johnston, M. B. 'Formation Dynamics of $CH_3NH_3PbI_3$ Perovskite Following Two-Step Layer Deposition'. *The Journal of Physical Chemistry Letters*, 2016, **7**, 96–102.

[102] Back, H.; Kim, J.; Kim, G.; Kyun Kim, T.; Kang, H.; Kong, J.; Ho Lee, S. and Lee, K. 'Interfacial Modification of Hole Transport Layers for Efficient Large-area Perovskite Solar Cells Achieved via Blade-coating'. *Solar Energy Materials and Solar Cells*, 2016, **144**, 309–315.

[103] Deng, Y.; Peng, E.; Shao, Y.; Xiao, Z.; Dong, Q. and Huang, J. 'Scalable Fabrication of Efficient Organolead Trihalide Perovskite Solar Cells with Doctor-bladed Active Layers'. *Energy & Environmental Science*, 2015, **8**, 1544–1550.

[104] Jiang, F.; Liu, T.; Luo, B.; Tong, J.; Qin, F.; Xiong, S.; Li, Z. and Zhou, Y. 'A Two-terminal Perovskite/Perovskite Tandem Solar Cell'. *Journal of Materials Chemistry A*, 2016, **4**, 1208–1213.

[105] Malinkiewicz, O.; Yella, A.; Lee, Y. H.; Espallargas, G. M.; Graetzel, M.; Nazeeruddin, M. K. and Bolink, H. J. 'Perovskite Solar Cells Employing Organic Charge-transport Layers'. *Nature Photonics*, 2013, **8**, 128–132.

[106] Polander, L. E.; Pahner, P.; Schwarze, M.; Saalfrank, M.; Koerner, C. and Leo, K. 'Hole-transport Material Variation in Fully Vacuum Deposited Perovskite Solar Cells'. *APL Materials*, 2014, **2**, 081503.

[107] Pistor, P.; Borchert, J.; Fränzel, W.; Csuk, R. and Scheer, R. 'Monitoring the Phase Formation of Coevaporated Lead Halide Perovskite Thin Films by in Situ X-ray Diffraction'. *The Journal of Physical Chemistry Letters*, 2014, **5**, 3308–3312.

[108] Ávila, J.; Momblona, C.; Boix, P. P.; Sessolo, M. and Bolink, H. J. 'Vapor-Deposited Perovskites: The Route to High-Performance Solar Cell Production?' *Joule*, 2017, **1**, 431–442.

[109] Momblona, C.; Gil-Escrig, L. N.; Bandiello, E.; Hutter, E. M.; Sessolo, M.; Lederer, K.; Blochwitz-Nimoth, J. and Bolink, H. J. 'Efficient Vacuum Deposited p-i-n and n-i-p Perovskite Solar Cells Employing Doped Charge Transport Layers'. *Energy Environ. Sci.* 2016, **3456**, 3456–3463.

[110] Borchert, J.; Boht, H.; Fränzel, W.; Csuk, R.; Scheer, R. and Pistor, P. 'Structural Investigation of Co-evaporated Methyl Ammonium Lead Halide Perovskite Films During Growth and Thermal Decomposition Using Different PbX_2 (X = I, Cl) Precursors'. en. *J. Mater. Chem. A*, 2015, **3**, 19842–19849.

[111] Arivazhagan, V.; Xie, J.; Yang, Z.; Hang, P.; Parvathi, M. M.; Xiao, K.; Cui, C.; Yang, D. and Yu, X. 'Vacuum Co-deposited $CH_3NH_3PbI_3FilmsbyControllingVaporPressureforEfficientPlanarPerovskiteSolarCells$'. *Solar Energy*, 2019, **181**, 339–344.

[112] Cojocaru, L.; Wienands, K.; Kim, T. W.; Uchida, S.; Bett, A. J.; Rafizadeh, S.; Goldschmidt, J. C. and Glunz, S. W. 'Detailed Investigation of Evaporated Perovskite Absorbers with High Crystal Quality on Different Substrates'. *ACS Applied Materials & Interfaces*, 2018, **10**, 26293–26302.

[113] Gil-Escrig, L.; Momblona, C.; La-Placa, M. G.; Boix, P. P.; Sessolo, M. and Bolink, H. J. 'Vacuum Deposited Triple-Cation Mixed-Halide Perovskite Solar Cells'. *Advanced Energy Materials*, 2018, **8**, 1–6.

[114] Park, C.-G.; Choi, W.-G.; Na, S. and Moon, T. 'All-Inorganic Perovskite $CsPbI_2BrThroughCo-evaporationforPlanarHeterojunctionSolarCells$'. *Electronic Materials Letters*, 2018, 1–5.

[115] Becker, P.; Márquez, J. A.; Just, J.; Al-Ashouri, A.; Hages, C.; Hempel, H.; Jošt, M.; Albrecht, S.; Frahm, R. and Unold, T. 'Low Temperature Synthesis of Stable γ-$CsPbI_3PerovskiteLayersforSolarCellsObtainedbyHighThroughputExperimentation$'. 2019, **9**, 1900555.

[116] Pistor, P.; Burwig, T.; Brzuska, C.; Weber, B. and Fränzel, W. 'Thermal Stability and Miscibility of Co-evaporated Methylammonium Lead Halide $(MAPbX_3, X = I, Br, Cl) Thin Films Analysed by In Situ X - ray Diffraction$'. *Journal of Materials Chemistry A*, 2018, **5**, 33083312.

[117] Burwig, T.; Fränzel, W. and Pistor, P. 'Crystal Phases and Thermal Stability of Co-evaporated $CsPbX_3 (X = I, Br) Thin Films$'. *The Journal of Physical Chemistry Letters*, 2018, **9**, 4808–4813.

[118] Olthof, S. and Meerholz, K. 'Substrate-dependent Electronic Structure and Film Formation of $MAPbI_3 Perovskites$'. *Nature Publishing Group*, 2016, 1–10.

[119] Zhao, D.; Ke, W.; Grice, C. R.; Cimaroli, A. J.; Tan, X.; Yang, M.; Collins, R. W.; Zhang, H.; Zhu, K. and Yan, Y. 'Annealing-free Efficient Vacuum-deposited Planar Perovskite Solar Cells with Evaporated Fullerenes as Electron-selective Layers'. *Nano Energy*, 2016, **19**, 88–97.

[120] PV Lighthouse. *The Solar Cell's Output Parameters*. https://www.pvlighthouse.com.au/resources/courses/altermatt/The%20PV%20Principle/The%20solar%20cells%20output%20parameters.aspx.

[121] Xiao, Z.; Dong, Q.; Bi, C.; Shao, Y.; Yuan, Y. and Huang, J. 'Solvent Annealing of Perovskite-Induced Crystal Growth for Photovoltaic-Device Efficiency Enhancement'. *Advanced Materials*, 2014, **26**, 6503–6509.

[122] Frost, J. M.; Butler, K. T. and Walsh, A. 'Molecular Ferroelectric Contributions to Anomalous Hysteresis in Hybrid Perovskite Solar Cells'. *APL Materials*, 2014, **2**, 081506.

[123] Weber, S. A.; Hermes, I. M.; Turren-Cruz, S. H.; Gort, C.; Bergmann, V. W.; Gilson, L.; Hagfeldt, A.; Graetzel, M.; Tress, W. and Berger, R. 'How the Formation of Interfacial Charge Causes Hysteresis in Perovskite Solar Cells'. *Energy and Environmental Science*, 2018, **11**, 2404–2413.

[124] Snaith, H. J.; Abate, A.; Ball, J. M.; Eperon, G. E.; Leijtens, T.; Noel, N. K.; Stranks, S. D.; Wang, J. T.-W.; Wojciechowski, K. and Zhang, W. 'Anomalous Hysteresis in Perovskite Solar Cells'. *The Journal of Physical Chemistry Letters*, 2014, **5**, 1511–1515.

[125] Unger, E. L.; Hoke, E. T.; Bailie, C. D.; Nguyen, W. H.; Bowring, A. R.; Heumuller, T.; Christoforo, M. G. and McGehee, M. D. 'Hysteresis and Transient Behavior in Current-Voltage Measurements of Hybrid-Perovskite Absorber Solar Cells'. *Energy & Environmental Science*, 2014, **7**, 3690–3698.

[126] Zimmermann, E.; Ehrenreich, P.; Pfadler, T.; Dorman, J. a.; Weickert, J. and Schmidt-Mende, L. 'Erroneous Efficiency Reports Harm Organic Solar Cell Research'. *Nature Photonics*, 2014, **8**, 669–672.

[127] Vanecek, M. and Poruba, A. 'Fourier-transform Photocurrent Spectroscopy of Microcrystalline Silicon for Solar Cells'. *Applied Physics Letters*, 2002, **80**, 719–721.

[128] Vandewal, K.; Goris, L.; Haeldermans, I.; Nesládek, M.; Haenen, K.; Wagner, P. and Manca, J. 'Fourier-Transform Photocurrent Spectroscopy for a fast and highly sensitive spectral characterization of organic and hybrid solar cells'. *Thin Solid Films*, 2008, **516**, 7135–7138.

[129] Poruba, A.; Hodakova, L.; Purkrt, A.; Holovsky, J.; Vanecek, M.; Purkrt, L. H. A.; Holovsky, J. and Vanecek, M. 'Fast Quantum Efficiency Measurement and Characterization of Different Thin Film Solar Cells by Fourier Transform Photocurrent Spectroscopy'. *2006 IEEE 4th World Conference on Photovoltaic Energy Conference*. Vol. 2. IEEE, 2006, 1525–1528.

[130] Koh, T. M.; Fu, K.; Fang, Y.; Chen, S.; Sum, T. C.; Mathews, N.; Mhaisalkar, S. G.; Boix, P. P. and Baikie, T. 'Formamidinium-Containing Metal-Halide: An Alternative Material for Near-IR Absorption Perovskite Solar Cells'. *The Journal of Physical Chemistry C*, 2014, **118**, 16458–16462.

[131] Eperon, G. E.; Stranks, S. D.; Menelaou, C.; Johnston, M. B.; Herz, L. M. and Snaith, H. J. 'Formamidinium lead trihalide: a broadly tunable perovskite for efficient planar heterojunction solar cells'. *Energy Environ. Sci.* 3 2014, **7**, 982–988.

[132] Habisreutinger, S. N.; Mcmeekin, D. P.; Snaith, H. J. and Nicholas, R. J. 'Research Update: Strategies for Improving the Stability of Perovskite Solar Cells'. *APL Materials*, 2016, **4**, 091503.

[133] McMeekin, D. P.; Sadoughi, G.; Rehman, W.; Eperon, G. E.; Saliba, M.; Hörantner, M. T.; Haghighirad, A.; Sakai, N.; Korte, L.; Rech, B. *et al.* 'A Mixed-cation Lead Mixed-halide Perovskite Absorber for Tandem Solar Cells'. *Science*, 2016, **351**, 151–155.

[134] Wang, Z.; McMeekin, D. P.; Sakai, N.; Reenen, S. van; Wojciechowski, K.; Patel, J. B.; Johnston, M. B. and Snaith, H. J. 'Efficient and Air-Stable Mixed-Cation Lead Mixed-Halide Perovskite Solar Cells with n-Doped Organic Electron Extraction Layers'. *Advanced Materials*, 2017, **29**. 1604186, 1604186.

[135] Lv, S.; Pang, S.; Zhou, Y.; Padture, N. P.; Hu, H.; Wang, L.; Zhou, X.; Zhu, H.; Zhang, L.; Huang, C. *et al.* 'One-step Solution-processed Formamidinium Lead Trihalide ($FAPbI_{(3-x)}Cl_x$) for Mesoscopic Perovskite-polymer Solar Cells'. *Physical Chemistry Chemical Physics*, 2014, **16**, 19206.

[136] Eperon, G. E.; Leijtens, T.; Bush, K. A.; Prasanna, R.; Green, T.; Wang, J. T.-W.; McMeekin, D. P.; Volonakis, G.; Milot, R. L.; May, R. *et al.* 'Perovskite-Perovskite Tandem Photovoltaics with Optimized Band Gaps.' *Science (New York, N.Y.)* 2016, **354**, 861–865.

[137] Ulbricht, R.; Hendry, E.; Shan, J.; Heinz, T. F. and Bonn, M. 'Carrier Dynamics in Semiconductors Studied with Time-resolved Terahertz Spectroscopy'. *Reviews of Modern Physics*, 2011, **83**, 543–586.

[138] Cabana, A and Sandordy, C. 'The Infrared Spectra of Solid Methylammonium Halides'. *Spectrochimica Acta*, 1962, **18**, 843–861.

[139] Yu, Y.; Wang, C.; Grice, C. R.; Shrestha, N.; Chen, J.; Zhao, D.; Liao, W.; Cimaroli, A. J.; Roland, P. J.; Ellingson, R. J. *et al.* 'Improving the Performance of Formamidinium and Cesium Lead Triiodide Perovskite Solar Cells using Lead Thiocyanate Additives'. *ChemSusChem*, 2016, **9**, 3288–3297.

[140] Xie, Z.; Sun, S.; Yan, Y.; Zhang, L.; Hou, R.; Tian, F. and Qin, G. G. 'Refractive Index and Extinction Coefficient of $NH_2CH = NH_2PbI_3$ Perovskite Photovoltaic Material'. *Journal of Physics: Condensed Matter*, 2017, **29**, 245702.

[141] Zhou, Z.; Pang, S.; Ji, F.; Zhang, B. and Cui, G. 'The Fabrication of Formamidinium Lead Iodide Perovskite Thin Films via Organic Cation Exchange'. *Chem. Commun.* 2016, **3828**, 3828–3831.

[142] Dimesso, L.; Quintilla, A.; Kim, Y.-M.; Lemmer, U. and Jaegermann, W. 'Investigation of Formamidinium and Guanidinium Lead Tri-iodide Powders as Precursors for Solar Cells'. *Materials Science and Engineering: B*, 2016, **204**, 27 –33.

[143] Binek, A.; Hanusch, F. C.; Docampo, P. and Bein, T. 'Stabilization of the Trigonal High-Temperature Phase of Formamidinium Lead Iodide'. *The Journal of Physical Chemistry Letters*, 2015, **6**, 1249–1253.

[144] Crothers, T. W.; Milot, R. L.; Patel, J. B.; Parrott, E. S.; Schlipf, J.; Mu, P.; Johnston, M. B. and Herz, L. M. 'Photon Reabsorption Masks Intrinsic Bimolecular Charge-Carrier Recombination in $CH_3NH_3PbI_3$ Perovskite'. *Nano Letters*, 2017, **17**, 57825789.

[145] Wright, A. D.; Verdi, C.; Milot, R. L.; Eperon, G. E.; Pérez-Osorio, M. A.; Snaith, H. J.; Giustino, F.; Johnston, M. B. and Herz, L. M. 'Electron–Phonon Coupling in Hybrid Lead Halide Perovskites'. *Nature Communications*, 2016, **7**, 11755.

[146] Quilettes, D. W. de; Vorpahl, S. M.; Stranks, S. D.; Nagaoka, H.; Eperon, G. E.; Ziffer, M. E.; Snaith, H. J. and Ginger, D. S. 'Impact of Microstructure on Local Carrier Lifetime in Perovskite Solar Cells'. *Science*, 2015, **348**, 683–686.

[147] Pellet, N.; Gao, P.; Gregori, G.; Yang, T.-Y.; Nazeeruddin, M. K.; Maier, J. and Grätzel, M. 'Mixed-organic-cation Perovskite Photovoltaics for Enhanced Solar-light Harvesting.' *Angewandte Chemie (International ed. in English)*, 2014, **53**, 3151–7.

[148] Wright, A. 'Intrinsic quantum oscillations in bulk halide perovskites'. In preparation.

[149] Levchuk, I.; Hou, Y.; Gruber, M.; Brandl, M.; Herre, P.; Tang, X.; Hoegl, F.; Batentschuk, M.; Osvet, A.; Hock, R. *et al.* 'Deciphering the Role of Impurities in Methylammonium Iodide and Their Impact on the Performance of Perovskite Solar Cells'. *Advanced Materials Interfaces*, 2016, 1600593.

[150] Gil-Escrig, L. L.; Miquel Sempere, A.; Sessolo, M.; Bolink, H. J.; Miquel-Sempere, A.; Sessolo, M. and Bolink, H. J. 'Mixed Iodide–Bromide Methylammonium Lead Perovskite-based Diodes for Light Emission and Photovoltaics'. *The Journal of Physical Chemistry Letters*, 2015, **6**, 3743–3748.

[151] Teuscher, J.; Ulianov, A.; Müntener, O.; Grätzel, M. and Tétreault, N. 'Control and Study of the Stoichiometry in Evaporated Perovskite Solar Cells'. *ChemSusChem*, 2015, **8**, 3847–3852.

[152] Borchert, J.; Levchuk, I.; Snoek, L. C.; Rothmann, M. U.; Haver, R.; Snaith, H. J.; Brabec, C. J.; Herz, L. M. and Johnston, M. B. 'Impurity Tracking Enables Enhanced Control and Reproducibility of Hybrid Perovskite Vapor Deposition'. *ACS Appl. Mater. Interfaces*, 2019, **11**, 2885128857.

[153] Nenon, D. P.; Christians, J. A.; Wheeler, L. M.; Blackburn, J. L.; Sanehira, E. M.; Dou, B.; Olsen, M. L.; Zhu, K.; Berry, J. J. and Luther, J. M. 'Structural and Chemical Evolution of Methylammonium Lead Halide Perovskites During Thermal Processing from Solution'. *Energy Environ. Sci.* 2016, **9**, 2072.

[154] Juarez-Perez, E. J.; Hawash, Z.; Raga, S. R.; Ono, L. K. and Qi, Y. 'Thermal Degradation of $CH_3NH_3PbI_3$ Perovskite into NH_3 and CH_3I Gases Observed by Coupled Thermogravimetry–Mass Spectrometry Analysis'. *Energy Environ. Sci.* 2016, **9**, 3406–3410.

[155] Baekbo, M. J.; Hansen, O.; Chorkendorff, I. and Vesborg, P. C. K. 'Deposition of Methylammonium Iodide via Evaporation-combined Kinetic and Mass Spectrometric Study'. *RSC Advances*, 2018, **8**, 29899.

[156] Zhang, W.; Pathak, S.; Sakai, N.; Stergiopoulos, T.; Nayak, P. K.; Noel, N. K.; Haghighirad, A. A.; Burlakov, V. M.; DeQuilettes, D. W.; Sadhanala, A. *et al.* 'Enhanced Optoelectronic Quality of Perovskite Thin Films with Hypophosphorous Acid for Planar Heterojunction Solar Cells'. *Nature Communications*, 2015, **6**, 10030.

[157] Yan, K.; Long, M.; Zhang, T.; Wei, Z.; Chen, H.; Yang, S. and Xu, J. 'Hybrid Halide Perovskite Solar Cell Precursors: Colloidal Chemistry and Coordination Engineering behind Device Processing for High Efficiency'. *Journal of the American Chemical Society*, 2015, **137**, 4460–4468.

[158] Miller, O. D.; Yablonovitch, E. and Kurtz, S. R. 'Strong Internal and External Luminescence as Solar Cells Approach the Shockley-Queisser Limit'. *IEEE Journal of Photovoltaics*, 2012, **2**, 303–311. eprint: 1106.1603.

[159] Sutherland, B. R. and Sargent, E. H. 'Perovskite Photonic Sources'. *Nature Photonics*, 2016, **10**, 295–302.

[160] Helio Display Materials. 2019. https://www.heliodisplaymaterials.com.

[161] Shi, Z. F.; Sun, X. G.; Wu, D.; Xu, T. T.; Tian, Y. T.; Zhang, Y. T.; Li, X. J. and Du, G. T. 'Near-infrared Random Lasing Realized in a Perovskite $CH_3NH_3PbI_3$ thin film'. *Journal of Materials Chemistry C*, 2016, **4**, 8373–8379.

[162] Deschler, F.; Price, M.; Pathak, S.; Klintberg, L. E.; Jarausch, D.-D.; Higler, R.; Hüttner, S.; Leijtens, T.; Stranks, S. D.; Snaith, H. J. *et al.* 'High Photoluminescence Efficiency and Optically Pumped Lasing in Solution-Processed Mixed Halide Perovskite Semiconductors'. *The Journal of Physical Chemistry Letters*, 2014, **5**, 1421–1426.

[163] Zhu, H.; Fu, Y.; Meng, F.; Wu, X.; Gong, Z.; Ding, Q.; Gustafsson, M. V.; Trinh, M. T.; Jin, S. and Zhu, X.-Y. 'Lead Halide Perovskite Nanowire Lasers with Low Lasing Thresholds and High Quality Factors'. *Nature Materials*, 2015, **14**, 636–642.

[164] Brenner, P.; Stulz, M.; Kapp, D.; Abzieher, T.; Paetzold, U. W.; Quintilla, A.; Howard, I. A.; Kalt, H. and Lemmer, U. 'Highly Stable Solution Processed Metal-halide Perovskite Lasers on Nanoimprinted Distributed Feedback Structures'. *Applied Physics Letters*, 2016, **109**, 141106.

[165] Sutherland, B. R.; Hoogland, S.; Adachi, M. M.; Kanjanaboos, P.; Wong, C. T. O.; McDowell, J. J.; Xu, J.; Voznyy, O.; Ning, Z.; Houtepen, A. J. *et al.* 'Perovskite Thin Films via Atomic Layer Deposition'. *Advanced Materials*, 2015, **27**, 53–58.

[166] Rayleigh, J. W. S. B. 'The Theory of Sound'. Vol. 2. MacMillan and Co., 1878, 115–117.

[167] Raman, C. V.; Sutherland, G. A. and Porter, A. W. 'On the Whispering-Gallery phenomenon'. *Proceedings of the Royal Society of London. Series A, Containing Papers of a Mathematical and Physical Character*, 1922, **100**, 424–428.

[168] Sutherland, B. R.; Hoogland, S.; Adachi, M. M.; Wong, C. T. O. and Sargent, E. H. 'Conformal Organohalide Perovskites Enable Lasing on Spherical Resonators'. 2014, **8**, 10947–10952.

[169] Liu, X.; Niu, L.; Wu, C.; Cong, C.; Wang, H.; Zeng, Q.; He, H.; Fu, Q.; Fu, W.; Yu, T. *et al.* 'Periodic Organic-Inorganic Halide Perovskite Microplatelet Arrays on Silicon Substrates for Room-Temperature Lasing'. *Advanced Science*, 2016, **3**, 1600137.

[170] Huang, C.; Sun, W.; Fan, Y.; Wang, Y.; Gao, Y.; Zhang, N.; Wang, K.; Liu, S.; Wang, S.; Xiao, S. *et al.* 'Formation of Lead Halide Perovskite Based Plasmonic Nanolasers and Nanolaser Arrays by Tailoring the Substrate'. *ACS Nano*, 2018, **12**, 3865–3874.

[171] Gao, Y.; Wang, S.; Huang, C.; Yi, N.; Wang, K.; Xiao, S. and Song, Q. 'Room Temperature Three-photon Pumped $CH_3NH_3PbBr_3$ perovskite microlasers'. *Scientific Reports*, 2017, **7**, 45391.

[172] Liao, Q.; Hu, K.; Zhang, H.; Wang, X.; Yao, J. and Fu, H. 'Perovskite Microdisk Microlasers Self-Assembled from Solution'. *Advanced Materials*, 2015, **27**, 3405–3410.

[173] Zhang, N.; Wang, K.; Wei, H.; Gu, Z.; Sun, W.; Li, J.; Xiao, S. and Song, Q. 'Postsynthetic and Selective Control of Lead Halide Perovskite Microlasers'. *The Journal of Physical Chemistry Letters*, 2016, **7**, 3886–3891.

[174] Roldan, C.; Malinkiewicz, O.; Betancur, R.; Longo, G.; Momblona, C.; Jaramillo, F.; Camacho, L.; Bolink, H. J.; Roldan-Carmona, C.; Malinkiewicz, O. *et al.* 'High Efficiency Single-junction Semitransparent Perovskite Solar Cells'. *Energy & Environmental Science*, 2014, **7**, 2968.

[175] Eperon, G. E.; Bryant, D.; Troughton, J.; Stranks, S. D.; Johnston, M. B.; Watson, T.; Worsley, D. A. and Snaith, H. J. 'Efficient, Semitransparent Neutral-Colored Solar Cells Based on Microstructured Formamidinium Lead Trihalide Perovskite'. *Journal of Physical Chemistry Letters*, 2015, **6**, 129–138.

[176] Wu, J.; Chen, J.; Zhang, Y.; Xu, Z.; Zhao, L.; Liu, T.; Luo, D.; Yang, W.; Chen, K.; Hu, Q. *et al.* 'Pinhole-Free Hybrid Perovskite Film with Arbitrarily-Shaped Micro-Patterns for Functional Optoelectronic Devices'. *Nano Letters*, 2017, **17**, 3563–3569.

[177] Hasan, M.; Venkatesan, S.; Lyashenko, D.; Slinker, J. D. and Zakhidov, A. 'Solvent Toolkit for Electrochemical Characterization of Hybrid Perovskite Films'. *Analytical Chemistry*, 2017, **89**, 9649–9653.